INFORMATION TO USERS

This manuscript has been reproduced from the microfilm master. UMI films the text directly from the original or copy submitted. Thus, some thesis and dissertation copies are in typewriter face, while others may be from any type of computer printer.

The quality of this reproduction is dependent upon the quality of the copy submitted. Broken or indistinct print, colored or poor quality illustrations and photographs, print bleedthrough, substandard margins, and improper alignment can adversely affect reproduction.

In the unlikely event that the author did not send UMI a complete manuscript and there are missing pages, these will be noted. Also, if unauthorized copyright material had to be removed, a note will indicate the deletion.

Oversize materials (e.g., maps, drawings, charts) are reproduced by sectioning the original, beginning at the upper left-hand corner and continuing from left to right in equal sections with small overlaps.

ProQuest Information and Learning
300 North Zeeb Road, Ann Arbor, MI 48106-1346 USA
800-521-0600

INFRARED PROPERTIES OF THREE LOW-DIMENSIONAL MATERIALS

By

Jeff McGuire

M. Sc. (Physics) McMaster University

A THESIS SUBMITTED TO

THE FACULTY OF GRADUATE STUDIES

IN PARTIAL FULFILLMENT OF

THE REQUIREMENTS FOR THE DEGREE OF

DOCTOR OF PHILOSOPHY

MCMASTER UNIVERSITY

May 2001

INFRARED PROPERTIES OF THREE LOW-DIMENSIONAL MATERIALS

DOCTOR OF PHILOSOPHY (2001) McMaster University

(Physics) Hamilton, Ontario

TITLE: Infrared Properties of Three Low-Dimensional Materials

AUTHOR: Jeff McGuire, M.Sc. (McMaster University)

SUPERVISOR: Professor T. Timusk

NUMBER OF PAGES: xi, 129

Abstract

This thesis includes far-infrared measurements of three new and very different materials, the spin-Peierls compound $CuGeO_3$, the quasi-two-dimensional organic superconductor κ-$(ET)_2Cu[N(CN)_2]Br$, and the high-temperature superconductor $HgBa_2Ca_2Cu_3O_{8-\delta}$. All three have reduced dimensionality and exhibit properties which are both of great interest to solid state physicists and ideal for study using far-infrared techniques.

$CuGeO_3$ is the first inorganic spin-Peierls compound to be discovered. It has a simple structure, is easily doped with impurities, and can be grown in the form of very large single crystals. These properties make it far easier to study than its organic predecessors. Like other spin-Peierls compounds, $CuGeO_3$ consists of chains of large tightly bound blocks that can move as units, in this case GeO_4 tetrahedra, and the spin-Peierls distortion can be described in terms of a displacement of these units. This thesis discusses a newly discovered local libration of the GeO_4 tetrahedra near impurity atoms in doped $CuGeO_3$. This unusual mode is highly anharmonic and causes striking features in the far-infrared spectra.

The superconductor κ-$(ET)_2Cu[N(CN)_2]Br$ belongs to a family of organic superconductors that, like the much studied high-temperature superconductors, consist of metallic sheets that are relatively isolated from one another. Conduction within the sheets is coherent, but the nature of the transport between the sheets is poorly understood. In this thesis, the first ever interplane far-infrared spectra for this material are reported. No evidence of coherent transport is found down to the lowest frequencies suggesting that in this respect this family of organic superconductors is similar to the high-temperature superconductors. Many internal modes of the ET molecule are also identified in the

spectra.

$HgBa_2Ca_2Cu_3O_{8-\delta}$ has the highest superconducting transition temperature ever measured, but single crystals large enough for infrared and far-infrared studies have only recently become available. This thesis presents in-plane infrared measurements on this material that show the presence of a pseudogap much like that seen in other high temperature superconductors except that it is considerably larger in size. In fact, its pseudogap is larger than those of the other materials by the same factor by which its transition temperature is higher. This suggests a possible relationship between pseudogap size and transition temperature which is discussed in light of other results in the literature.

All three of these materials are either quasi-one-dimensional or quasi-two-dimensional in nature and demonstrate both the diversity of the phenomena found in solid state systems and the utility of far-infrared spectroscopy in their study.

Acknowledgements

I would like to take this opportunity to thank my supervisor, Tom Timusk, who has provided me with years of guidance, encouragement and patience. With his help my time at McMaster University has been both pleasant and rewarding.

Thanks also goes to the members of my supervisory committee, Profs. Bruce Gaulin and John Preston. Their time and advice were very helpful.

With gratitude I acknowledge the assistance on countless occasions of Gord Hewitson, Jim Garrett and Bruce Collier and the fine work of the machine shop staff, Clee, Michael. Yosh. Venice, and Paul.

I would like to thank my colleagues and friends, Andy Duncan, Andy Duft, Rob Hughes, John Nam, Tatiana Startseva, Anton Puchkov, Dimitri Basov, Toomas Rõõm, Marco Windt, and Artem Pronin. Their contributions to this thesis and their companionship are very much appreciated.

I am fortunate to have the love and support of my parents, Joe and Connie McGuire. and my sister and brothers, Jen, Jerry, James, Joe, Jon and Josh. I am who I am because of them, and they are with me wherever I go.

Much of the joy in my life over the last fourteen years has been due to my girlfriend and now fiancée, Denise Teskey. Her love and support, admiration and criticism, laughter and music, have empowered me, and I look forward to our future together.

Finally, I thank my Lord and Saviour for giving me all that I have and for loving all that I am and will be.

Table of Contents

List of Tables

List of Figures

Chapter 1

FAR-INFRARED AND THE SOLID STATE

Infrared and far-infrared spectroscopy is a powerful tool for probing the physics of solids. This thesis describes the results obtained from infrared studies of three quasi-one-dimensional or quasi-two-dimensional materials. The first is the spin-Peierls compound $CuGeO_3$. The discovery of a very unusual, highly anharmonic librational mode seen in far-infrared spectra of doped samples of this material is discussed. The second material is the quasi-two-dimensional organic superconductor κ-$(ET)_2Cu[N(CN)_2]Br$. Spectra with the light polarized in the least conducting direction are used to discuss incoherent transport in layered systems. The third material is the high-temperature superconductor $HgBa_2Ca_2Cu_3O_{8-\delta}$. In-plane spectra show a pseudogap feature which is significantly higher in energy than that seen in any other material. This appears to be related to its exceptionally high transition temperature. The common thread that will run through the discussion of these three results will be the use of infrared and far-infrared spectroscopy.

This introductory chapter is meant to give the reader some general background that will be useful in understanding the more detailed material found in later chapters. Section 1.1 lists and briefly describes many of the phenomena in solid state physics that are relevant to spin-Peierls, organic and high-temperature superconducting systems. Section 1.2 goes on to discuss how these phenomena manifest themselves in infrared and far-infrared spectra. Section 1.3 ends the introduction with an overview of what is contained in the remaining chapters of the thesis.

1.1 Aspects of solid state physics

The theoretical description of the solid state[1, 2] has been and continues to be a very difficult challenge to physicists. The difficulty arises from the incredible number of degrees of freedom in any given solid where one must consider some 10^{23} individual atoms per cubic centimeter and the interactions between them. Each atom can be described by the location of its nucleus and the configuration of its electrons, some of which will remain closely associated with the nucleus, while others stay nearby but interact with neighbouring atoms, and still others may roam freely throughout the solid. Both the electric charge and magnetic spin of the electrons affect the energy of the system which will naturally exist in the configuration of least Gibbs free energy. The challenge to physicists is to find approximate descriptions of these systems that are simple enough to be understood yet accurate enough to correctly predict the lowest energy states.

In equilibrium and at low temperature each atom is positioned so as to minimize the energy due to attraction to and repulsion from neighbouring atoms. The resulting fixed position is perhaps the most basic aspect of a solid since this differentiates it from a liquid or a gas. In almost all cases, the lowest-energy configuration is the repeating geometrical pattern of a crystal lattice. Since the lattice can be completely characterized by its fundamental building block, the unit cell, this greatly simplifies the theoretical description of the solid.

When a small amount of energy is added to the lattice by, for example, raising its temperature, the resulting motion of the atoms about their lattice positions can be described in terms of the fundamental vibrational modes of the crystal. The vibrations can be longitudinal like sound waves in air, or transverse like the vibrations of a guitar string. If there is only one atom per unit cell, then there are three vibrational modes, one longitudinal and two transverse. If there are n atoms per unit cell, then in addition to

these three acoustic modes, there are $3n - 3$ optical modes that often couple to light. In the acoustic modes all the atoms in a given unit cell move in unison, while in the optical modes various atoms within the unit cell move in opposite directions. The relationship between the energy of a phonon, the fundamental excitation associated with a mode, and its spacial period is determined by the masses of and the forces between the atoms. The total energy supplied to a mode determines the occupation number of the phonon.

In this thesis two special kinds of phonons will be discussed. The first kind is referred to as a local mode[3], and occurs when the regular crystal lattice is interrupted by an impurity atom. This modifies the set of phonons associated with a mode so that the nature of one of the phonons is greatly modified while the rest of the phonons are only slightly affected. The energy of the greatly modified phonon is moved away from the energies of the other phonons, and its amplitude is appreciable only at the impurity site so that it can no longer be considered a true phonon. Usually such local modes are found at energies above those of the other phonons, but they can also be found at very low energies in which case they are referred to as resonant modes. Such a mode in doped $CuGeO_3$ will be studied in Chapter 2.

The second special kind of phonon to be discussed occurs when a solid is formed from molecular units. An isolated molecule has a set of fundamental vibrational modes depending on the number, configuration, mass and bond strength of the constituent atoms. Often, when molecules are combined to form a solid, the forces within the molecules are stronger than the forces between the molecules so that many of the phonons in the solid simply correspond to the molecules vibrating with the same vibrational modes as in an isolated molecule. Such internal-mode phonons occur at nearly the same energy as in the isolated molecules. The optical response of κ-$(ET)_2Cu[N(CN)_2]Br$ that will be discussed in Chapter 3 contains several phonons which will be identified with the internal modes of the ET molecule.

Depending on the configuration of its electrons, each atom in the lattice may have a magnetic spin which provides an additional interaction between the atoms. If they are ferromagnetically coupled then the energy is lowest when the spins of adjacent atoms are aligned, while if they are antiferromagnetically coupled then the energy is lowest when adjacent spins point in opposite directions. At low temperatures the spins can be ordered, but as the crystal is heated the directions of the spins fluctuate producing spin-waves with magnons as the fundamental excitations. As the temperature is raised, the number of magnons increase until a phase transition occurs and the spins can no longer be thought of as ordered. This transition temperature is the Curie temperature for ferromagnets and the Néel temperature for antiferromagnets. Antiferromagnetic correlations are an important aspect of all three materials studied in this thesis, although the focus here will be on other properties.

While the energy states of the electrons in a solid are related to the states that would exist in a single isolated atom, the atoms are close enough together for the states furthest from the nuclei to overlap with the corresponding states of nearby atoms. These overlapping states form bands of extended states that are no longer associated with particular atoms. The valence band is the highest full or nearly full electronic band, and the conduction band is the lowest band that consists of mostly unoccupied states. In an insulator the conduction band is completely empty, the valence band is full, and they are separated by a large energy gap ΔE. A completely full band necessarily corresponds to zero net motion of the electrons so that in an insulator, even if an electric field is applied, the electrons cannot rearrange their quantum states to produce an electric current. In a semiconductor the gap ΔE is so small that fluctuations due to the temperature are enough to cause some of the valence electrons to jump into the conduction band. A semiconductor is an insulator at low temperatures but becomes a progressively better conductor as it is heated. In a metal the conduction band is partially occupied even at

zero temperature so that the electrons it contains can readily produce electric currents.

Depending on the crystallographic arrangement of the atoms, some materials are much better conductors in some directions than in others. Quasi-one-dimensional metals conduct primarily along one direction only. The one-dimensional organic conductors that are discussed in Chapter 3 are one example of such materials, while $CuGeO_3$, which is discussed in Chapter 2, is an insulator with quasi-one-dimensional magnetic properties. Quasi-two-dimensional metals conduct primarily in two directions and have a layered structure of relatively isolated conducting sheets. Examples of these materials are the two-dimensional organic superconductors discussed in Chapter 3 and the high-temperature superconductors discussed in Chapter 4. This low dimensionality is often accompanied by interesting physical phenomena.

One example of this is the Peierls effect in quasi-one-dimensional metals where a shift in the positions of the atoms in every other unit cell doubles the size of the unit cell and causes a gap to develop in the middle of an electronic band splitting it into two bands. The effect of the gap is a decrease in the energy of the states near the top of the lower band and an increase in the energy of the states near the bottom of the upper band. This results in a lowering of the total energy of the electrons since there are only enough electrons to fill the lower band leaving the upper band empty. Of course, the shifting of the atoms causes an increase in lattice energy, but this increase is less than the resulting decrease in electronic energy. The Peierls transition only occurs at low temperatures where the effect of the gap is not washed out by thermal excitations.

A similar effect called a spin-Peierls transition can occur in quasi-one-dimensional materials with $S = \frac{1}{2}$ magnetic spins. Here the distortion of the lattice causes a gap to develop not in an electronic band, but rather in the spectrum of magnetic excitations. Adjacent spins move toward each other to form spin-singlets that are separated by an energy gap from the excited spin triplet-state. The tradeoff between magnetic energy

and lattice energy leads to a spin-Peierls phase transition at low temperatures. Some of the organic conductors, discussed in Chapter 3, as well as $CuGeO_3$, which is the subject of Chapter 2, have a spin-Peierls transition.

One last phenomenon to be discussed is superconductivity. Like the ferromagnetic, antiferromagnetic, Peierls and spin-Peierls states that have already been mentioned, superconductivity is an ordered collective state that exists in some materials at low temperatures where thermal fluctuations are small. One of its characteristics is the ability of current to flow without the electrical resistance normally felt by moving electrons due to impurities, lattice defects and thermal fluctuations of the lattice. Another characteristic is its ability to exclude a magnetic field from penetrating the bulk of the material.

The BCS theory of superconductivity describes the essence of the phenomenon [4]. It turns out that any attractive force between the electrons will favour a state in which electrons of opposite spin and momentum will form Cooper pairs, and these pairs carry electric charge in a superconductor. The Cooper pairs are organized in such a way that the energy of the electrons is lower by an amount Δ than the energy of the electrons in the normal metallic state. As a result the material becomes superconducting at low temperatures where the thermal excitations are small compared to Δ. The reason an attractive force can exist between two electrons that would normally repel each other due to their common negative charge, is that the electrons are inside a solid where the local effect of one electron on the solid can be attractive to a second electron. In most superconductors it is a movement of atoms in the crystal lattice which is responsible. In other words, phonons are the coupling mechanism.

Over the years many different kinds of superconductors have been discovered. The first discovery of superconductivity was made in 1911, when it was observed by the group of Heike Kamerlingh Onnes in mercury with a transition temperature $T_c = 4$ K[5]. Materials with higher T_c were found later, but by 1974 the highest T_c was still only 24 K.

These early superconductors are well described by the BCS theory and are now referred to as conventional superconductors. In 1986 Bednorz and Müller discovered a member of a new class of superconductors now referred to as high-temperature superconductors[6]. These materials, as the name suggests, have the highest known transition temperatures. $HgBa_2Ca_2Cu_3O_{8-\delta}$ has the highest with $T_c = 135$ K and is the subject of Chapter 4 of this thesis. Other classes are also known such as heavy-fermion and organic superconductors. Chapter 3 of this thesis discusses an organic superconductor with a T_c of 12 K. All of these unconventional superconductors have properties such as low dimensionality, gap asymmetry or unusual pairing mechanisms that make them considerably less understood than conventional superconductors and one of the most active areas of research in condensed matter physics.

1.2 Optical response

Maxwell's equations (Eq. 1.1) describe the interaction of electromagnetic fields with matter.

$$\nabla \cdot \mathbf{E} = 4\pi\rho, \qquad \nabla \cdot \mathbf{H} = 0, \qquad \nabla \times \mathbf{E} = -\frac{\mu}{c}\frac{\delta \mathbf{H}}{\delta t}, \qquad \nabla \times \mathbf{H} = \frac{\epsilon}{c}\frac{\delta \mathbf{E}}{\delta t} + \frac{4\pi\sigma}{c}\mathbf{E} \tag{1.1}$$

E and **H** are the electric and magnetic fields, and the charge density ρ, magnetic permeability μ, dielectric function ϵ, and conductivity σ are properties of matter.

Light is a transverse electromagnetic wave consisting of electric and magnetic fields oriented perpendicular to each other and to the direction of propagation. The wave equation, which describes the electric field component of light. can easily be derived from Maxwell's equations:

$$\nabla^2 \mathbf{E} = -\frac{\omega^2}{c^2}\left[\epsilon + \frac{4\pi i}{\omega}\sigma\right]\mathbf{E} = -\frac{\omega^2}{c^2}N^2\mathbf{E} \tag{1.2}$$

This equation has solutions of the form:

$$\mathbf{E}(x,t) = \mathbf{E}_0 e^{i(\frac{\omega}{c}Nx - \omega t)} \tag{1.3}$$

where N is the complex index of refraction and ω is the angular frequency of the wave's oscillation. Just as ω gives the interval of time over which the wave goes through an oscillation, the corresponding interval of space or wavelength can be determined from the real part of N which gives the speed of propagation through the material. The imaginary part of N gives the degree to which the wave decays as its energy is absorbed by the material.

The separation of the contributions of ϵ and σ to N is somewhat ambiguous. The dielectric function ϵ describes the polarization due to the response of bound charges to an electric field while the conductivity σ describes the response of free conduction electrons to an electric field. The distinction between these concepts, however, becomes blurred at high frequencies, and the complex nature of ϵ and σ allows either of these functions to describe both phenomena. N is therefore often redefined as:

$$\left[\epsilon + \frac{4\pi i}{\omega}\sigma\right] = N^2 \qquad \longrightarrow \qquad \epsilon = 1 + \frac{4\pi i}{\omega}\sigma = N^2 \tag{1.4}$$

so that the real and imaginary parts of $N = n + i\kappa$, $\epsilon = \epsilon_1 + i\epsilon_2$ and $\sigma = \sigma_1 + i\sigma_2$ are related by:

$$\epsilon_1 = 1 - \frac{4\pi}{\omega}\sigma_2 = n^2 - \kappa^2, \qquad \epsilon_2 = \frac{4\pi}{\omega}\sigma_1 = 2n\kappa \tag{1.5}$$

The energy carried by a single photon is $\hbar\omega$, where ω is the frequency of the light and $\hbar = 1.055 \times 10^{-34}$ Js is Planck's constant. Because of this direct relationship between the frequency and energy of light, frequency units such as Hz and rad/s are often used as units for light energy. The inverse of the vacuum wavelength of the light is often used as another frequency unit, since in vacuum $1/\lambda = \omega/2\pi c$ where $c = 3.0 \times 10^{10}$ cm/s is the speed of light. This unit, cm^{-1}, is called a wavenumber and is often the unit of choice in

spectroscopy since it arises naturally from the Fourier transform techniques used to make measurements. Fig. 1.1 shows the electromagnetic spectrum on a logarithmic scale in a variety of energy units. On the extreme ends of the spectrum are radio waves and gamma rays which have little use in the study of solid state systems because their energies are too low or too high to be of interest. x-rays are primarily used to determine the structure of a material's crystal lattice. Of the rest of the spectrum, it is the infrared and far-infrared that are most appropriate for solid state spectroscopy. The signatures of many excitations of interest, such as phonons, magnons and excitations across energy gaps, can be found in the optical responses of solids (N, ϵ and σ) at infrared and far-infrared frequencies.

The mathematical form of the optical response of an electric charge can be calculated by considering the simple force equation $F = ma$ which, for an electric charge in an electric field, has the form:

$$-eE - kx - m\Gamma\frac{\partial x}{\partial t} = m\frac{\partial^2 x}{\partial t^2} \tag{1.6}$$

In Eq. 1.6 the three terms on the left are: (1) the force of the field on the charge, (2) any restoring force that might be present if the charge is bound, and (3) a damping term due to scattering. e is the electric charge, $k = m\omega_0^2$ is a spring constant, m is the mass associated with the charge, and Γ is a scattering rate. Assuming an oscillating field and position, $E(t) = Ee^{i\omega t}$ and $x(t) = xe^{i\omega t}$, we have:

$$x = \frac{-eE/m}{\omega_0^2 - \omega^2 - i\Gamma\omega} \tag{1.7}$$

This can be used to derive the dielectric function and the optical conductivity. The electric displacement field is $D = \epsilon E = E + 4\pi P$ with the polarization $P = -nex$ where n is the charge density. This, along with Eq. 1.7, gives for the dielectric function:

$$\epsilon = 1 + \frac{\omega_p^2}{\omega_0^2 - \omega^2 - i\Gamma\omega} \tag{1.8}$$

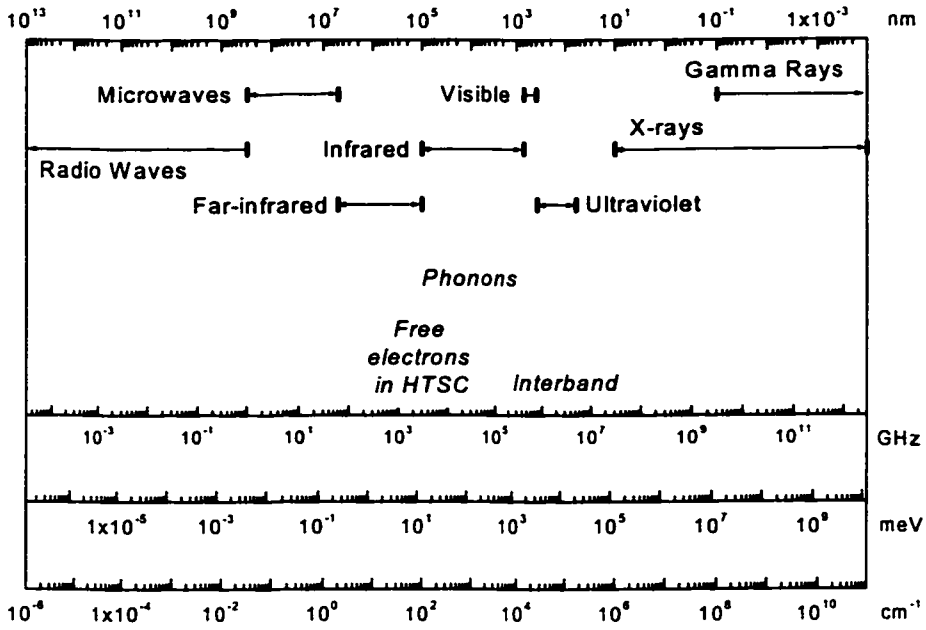

Figure 1.1: The electromagnetic spectrum.
Many of the processes in condensed matter physics occur on an energy scale that corresponds to infrared or far-infrared light making it a very useful experimental probe.

where $\omega_p^2 = 4\pi ne^2/m$ is the plasma frequency. The current density is $J = \sigma E = -nev = nei\omega x$ which, along with Eq. 1.7, gives for the optical conductivity:

$$\sigma = -\frac{i\omega}{4\pi}\frac{\omega_p^2}{\omega_0^2 - \omega^2 - i\Gamma\omega} \tag{1.9}$$

These expressions for ϵ and σ are consistent with Eqs. 1.4 and 1.5.

These equations can describe free electrons or a response due to phonons or magnons which occur at a frequency ω_0. Their form in ϵ_2 and σ_1, which are related to energy absorption, is a Lorentzian oscillator which is nonzero only near ω_0 with an intensity given by ω_p^2 and a width given by Γ. Free electrons are unbound and are therefore described by Eq. 1.6 without the spring constant term. This gives a Lorentzian oscillator with $\omega_0 = 0$ referred to as a Drude peak. Its value at $\omega = 0$ in σ_1 corresponds to the DC conductivity. For illustrative purposes, Fig. 1.2 shows ϵ and σ for a simple model material with a Drude term and two oscillators, a strong one centred at 700 cm^{-1} and a weaker one centred at 1200 cm^{-1}. Clearly ϵ and σ give the same information, and in this thesis it will usually be σ and in particular σ_1 that is discussed.

An energy gap in the available electronic states will show up as a suppression of σ_1 below the gap energy. This can be seen in the upper panel of Fig. 1.3 which shows σ_1 for an organic material with a semiconducting gap at 1120 cm^{-1}[7]. A similar suppression of σ_1 can be seen in the superconducting state of conventional BCS superconductors. The lower panel of Fig. 1.3 shows this for lead which superconducts below 7.2 K[8]. Here the suppression occurs below twice the gap energy since both members of a Cooper pair must be excited across the gap. There is a sum rule that states that the total area under the conductivity curve is the same at all temperatures. In the superconducting state, the suppressed spectral weight below 2Δ is actually transferred to a delta function at $\omega = 0$ related to the infinite DC conductivity. For some unconventional superconductors, like the high-temperature superconductors in which the gap is actually zero in some

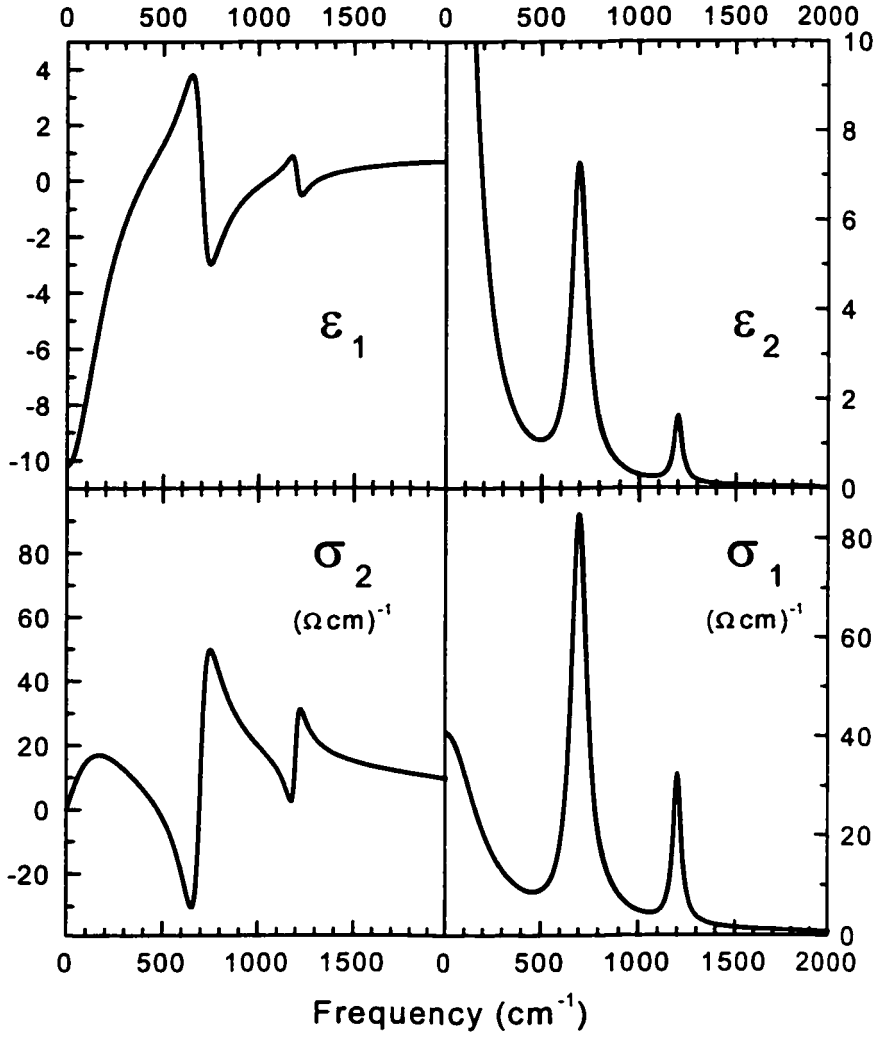

Figure 1.2: ϵ and σ for a simple model system.
The spectra are calculated for a Drude term along with two oscillators at 700 and 1200 cm^{-1}.

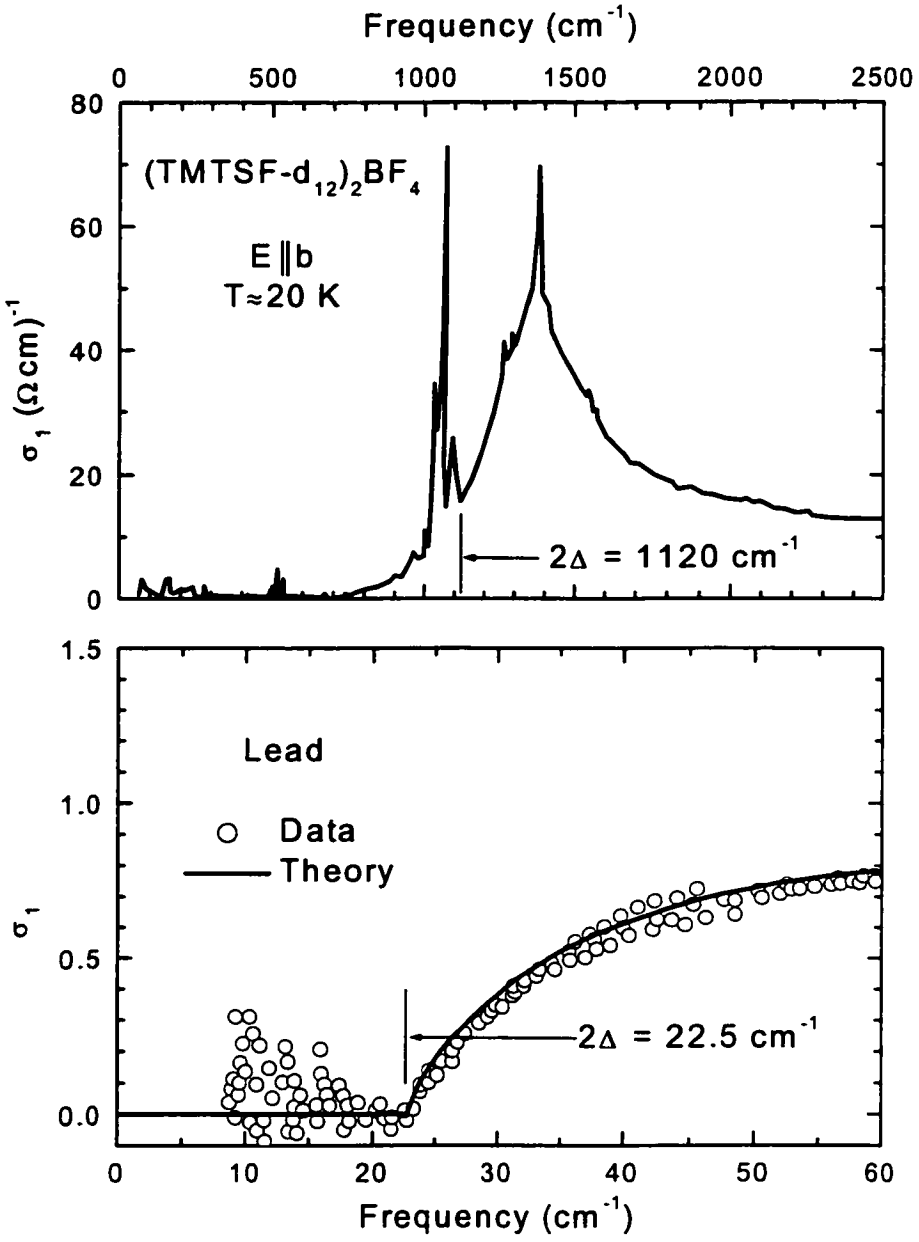

Figure 1.3: Gaps in the real part of the optical conductivity.
The upper panel shows a semiconducting gap in an organic material[7], and the lower panel shows the superconducting gap in lead, a conventional superconductor[8].

directions, the gap in the conductivity is replaced by a pseudogap. This phenomenon will be discussed in more detail in Chapter 4.

In practice, the optical response of a transparent material is determined in an experiment by passing light through the material and observing how much light is absorbed at each frequency. For opaque materials it is easier to reflect light off the sample's surface. The techniques used to measure these effects and then obtain an optical response function such as ϵ or σ will be described in Chapter 2 for transmission and in Chapter 3 for reflection.

1.3 Thesis overview

This thesis describes the results of far-infrared measurements of three distinct materials, the spin-Peierls compound $CuGeO_3$, the organic superconductor κ-$(ET)_2Cu[N(CN)_2]Br$, and the high-temperature superconductor $HgBa_2Ca_2Cu_3O_{8-\delta}$. Chapter 2 covers the work on $CuGeO_3$. It includes an overview of the apparatus used to make far-infrared tranmission measurements, a description of the spin-Peierls phenomenon in $CuGeO_3$, and a presentation and discussion of the measured spectra. Chapter 3 is devoted to κ-$(ET)_2Cu[N(CN)_2]Br$. It begins with a discussion of the experimental and theoretical techniques used to measure far-infrared reflectance and obtain optical conductivity. This is followed by a description of organic superconductors in general and κ-$(ET)_2Cu[N(CN)_2]Br$ in particular. Finally, data on the interplane conductivity of κ-$(ET)_2Cu[N(CN)_2]Br$ are presented. Chapter 4 turns to the high-temperature superconductor $HgBa_2Ca_2Cu_3O_{8-\delta}$. A discussion of high-temperature superconductivity is followed by an examination of the far-infrared in-plane optical spectra of this superconductor which has the highest known transition temperature. Chapter 5 summarizes the major findings of the previous chapters and makes suggestions for future research.

Chapter 2

$CuGeO_3$

In recent years $CuGeO_3$ has been the focus of much excitement. It was shown to undergo a spin-Peierls transition at $T_{SP} = 14$ K, making it the first inorganic spin-Peierls compound ever discovered. Because of its simple structure and the fact that it is easily doped with impurities, this material is ideal for studying the spin-Peierls phenomenon. Investigations have been performed using a wide variety of techniques including magnetic susceptibility, NMR, neutron scattering, and optical spectroscopy. Phase transitions have been shown to occur with changes in temperature, pressure, doping, and magnetic field. The results reported here were obtained from far-infrared transmittance measurements from 3 to 100 cm^{-1} on doped samples at temperatures from 1.2 to 100 K and in fields up to 18 T. Of particular interest is the discovery through this study of an unusual, highly anharmonic librational mode associated with the dopant ions[9].

Section 2.1 is a description of the apparatus and experimental techniques used to perform the measurements. Section 2.2 is an overview of the spin-Peierls phenomenon and a summary of the properties of $CuGeO_3$. Section 2.3 contains the far-infrared transmittance results including a discussion of the anharmonic librational mode.

2.1 Far-infrared transmittance measurements

Optical spectroscopy is the study of the interaction of matter with light as a function of the frequency or energy of the light. In Chapter 1, Fig. 1.1 showed a chart of the various regions of the light spectrum that have been used in the study of condensed matter

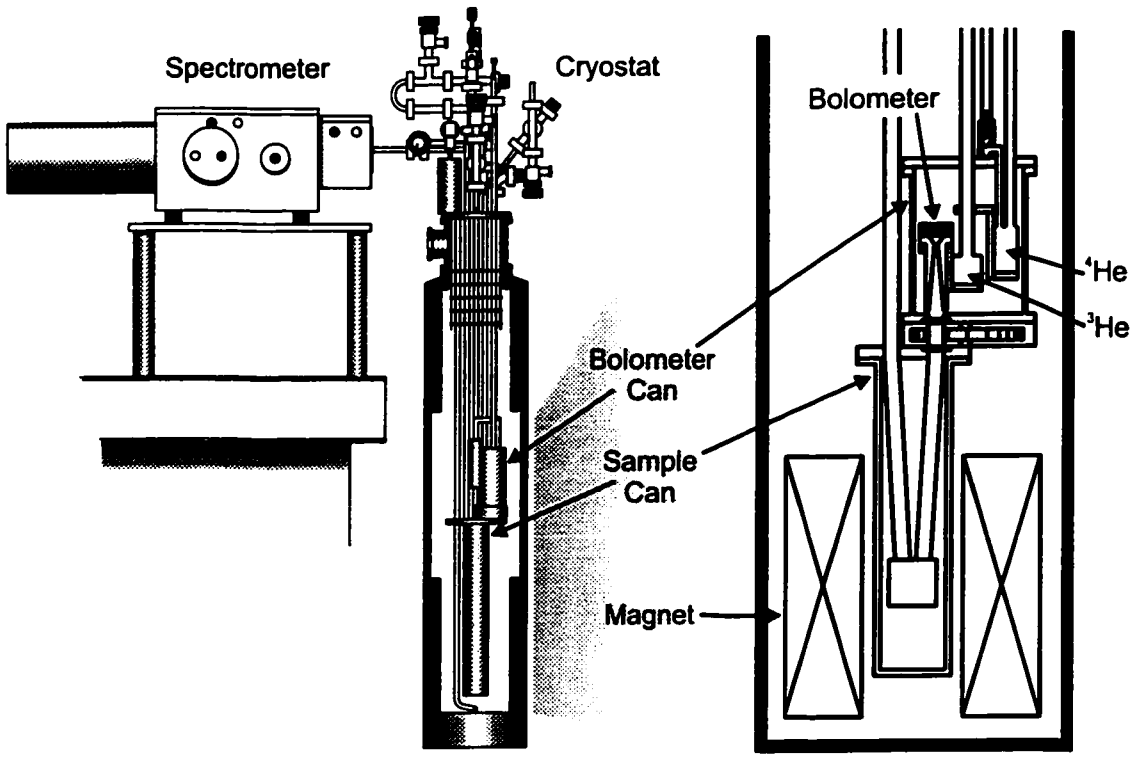

Figure 2.1: Apparatus for measuring far-infrared transmittance.
Light from a Martin-Puplett spectrometer is guided by a light-pipe to the sample and bolometer at the bottom of a liquid-helium-cooled cryostat. A superconducting magnet allows measurements in high magnetic fields.

along with some of the physical phenomena that have been observed. Some regions of the spectrum are more difficult than others to access experimentally, particularly the region between 1 and 10 cm^{-1} on the boundary between microwaves and the far-infrared. Microwave techniques require waveguides with physical dimensions that depend on the wavelength of the light. At higher energies the wavelengths become shorter and as a result require smaller waveguides. A practical limit is reached around 1 cm^{-1}. The limit on the far-infrared side is due mainly to the lack of high-intensity light sources in this part of the spectrum. Some potential solutions to this problem are the use synchrotron radiation, backward wave oscillators and terahertz spectroscopy, but these have not yet replaced the traditional Hg-arc lamp. While less intense, this light source is stable, provides light over a broad range of frequencies, and is relatively inexpensive. The light intensity decreases with decreasing frequency giving a practical limit around 10 cm^{-1}. This can be extended down to 2-3 cm^{-1} with the use of extremely sensitive bolometers that operate at 0.3 K.

The apparatus[10] uses a 0.3 K bolometer and is shown in Fig. 2.1. Both the bolometer and the sample are contained in a cryostat which is submerged in liquid helium. The far-infrared light is generated by a Hg-arc lamp in a Martin-Puplett spectrometer. It is coupled to the cryostat via a polished brass light pipe that extends about 1 m from the exit of the spectrometer to the sample chamber at the bottom of the cryostat. Here the light interacts with the sample before being directed back up into the bolometer chamber where it is detected.

The Martin-Puplett spectrometer[11], shown in Fig. 2.2, is a variation of the Michelson interferometer. In a Michelson interferometer, a light beam is split and sent along two separate paths, one of which is of variable length. When the beams recombine, the phase difference between them results in interference that depends on the difference in the lengths of the two light paths. The resulting light intensity as a function of path

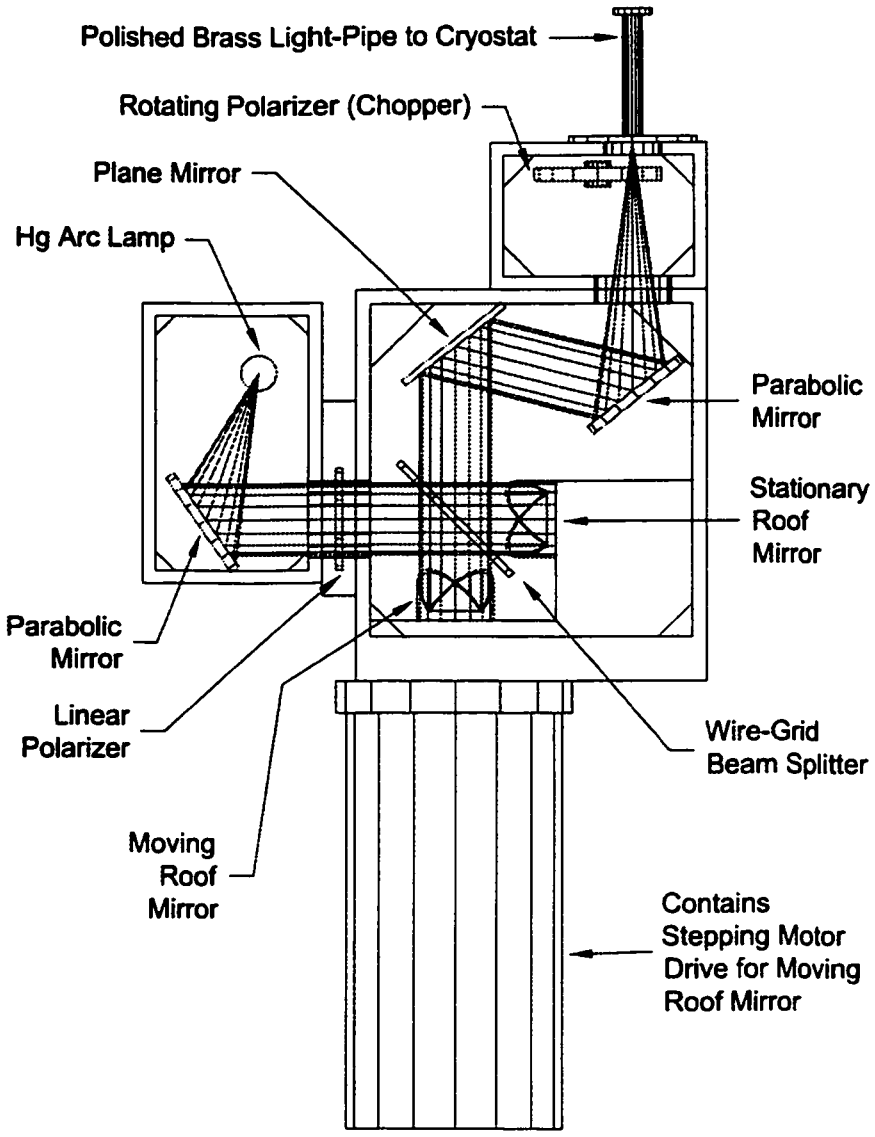

Figure 2.2: Martin-Puplett spectrometer.
The spectrometer is similar to a Michelson spectrometer except that it makes use of polarization. It is especially efficient at long wavelengths.

difference, called an interferogram, can then be Fourier transformed to give the intensity as a function of frequency[12]. In a Martin-Puplett spectrometer, the two light beams have orthogonal linear polarizations. When they are recombined the degree of circular polarization of the combined beam depends on the path difference. By passing the beam through a rotating linear polarizer, one obtains an intensity modulation with an amplitude that depends on the degree of circular polarization and hence on the path difference. This is analogous to the Michelson interferogram and can be Fourier transformed to give a spectrum. The Martin-Puplett spectrometer takes maximum advantage of the little light that is available at far-infrared frequencies since the wire-grid beamsplitter and polarizers approach 100% efficiency at long wavelengths, although they become less efficient at higher frequencies where the wavelength is no longer large compared to the separation of the wires in the grid.

The cryostat, shown in Fig. 2.1, is unique in that it is designed to allow optical measurements in a high magnetic field. It was designed specifically for use with the 18 T superconducting magnet at the University of Toronto. This 18 T limit sets the energy scale for processes that can be best studied with the apparatus. The operating temperature and spectral range were chosen to match this energy scale such that $\mu H \approx \hbar\omega \approx k_B T$. 18 T corresponds to 24 K which is easily achieved with liquid helium. 18 T also corresponds to 17 cm^{-1} demonstrating the appropriateness of using far-infrared frequencies. The specific requirements for far-infrared measurements along with the constraint of working within the 2 inch diameter core of the magnet are what determined the design of the cryostat.

A sketch of the contents of the bolometer chamber can be seen in Fig. 2.1. It consists of several components. The bolometer and JFET perform the actual detection of the light and impedance matching of the signal. The ^{3}He can holds the liquid ^{3}He which is pumped by the charcoal pump to cool the bolometer to its operating temperature

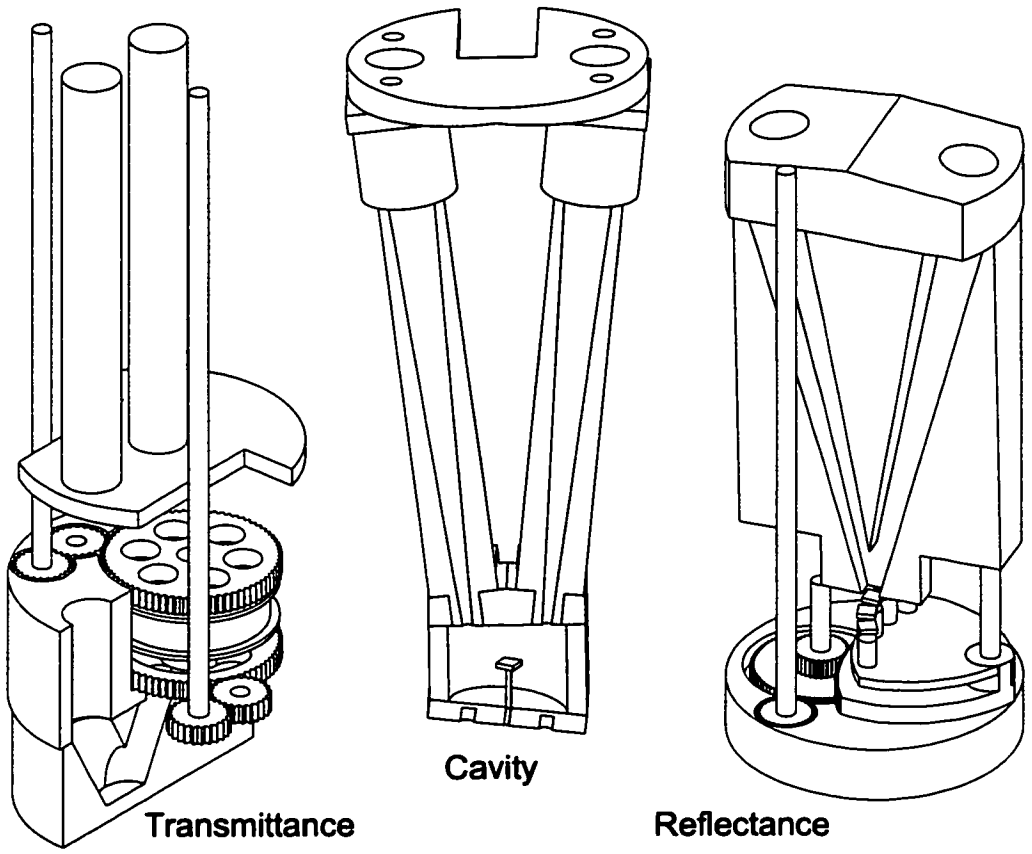

Figure 2.3: Three modes of far-infrared measurement.
Depending on the contents of the sample chamber, the light is either transmitted through the sample, reflected multiple times from the sample surface, or reflected once before being directed back up to the bolometer to be detected.

of 0.3 K. In order to condense the ^{3}He gas into the ^{3}He can, it is initially cooled by its thermal connection to the ^{4}He can that contains pumped liquid ^{4}He at 1.2 K. Finally, the filter wheel allows various optical filters to be placed in the light path to block out high-frequency light that would otherwise overload the bolometer. Since the spectrometer is not effective in modulating light above 100 cm^{-1}, this light can be blocked out without losing additional information. To measure the lowest frequencies, where the intensity is very low, it is often desirable to block out all other frequencies in order to decrease the noise and scan times. By using various filters, spectra can be measured from 3 to 100 cm^{-1}.

The contents of the sample chamber are often as complex as those of the bolometer chamber and yet must fit into a smaller space since the entire sample chamber must fit into the 2 inch core of the magnet. The three measurement modes that are available are reflectance, transmittance and cavity, and these are shown in Fig. 2.3. The reflectance mode measures the light after a single reflection off the sample. The cavity mode allows the light to reflect several times off the sample as it bounces around inside a polished cavity. The transmittance mode allows the light to pass through the sample and is the technique most appropriate for transparent samples like $CuGeO_3$. In the transmittance mode, the samples are mounted on a wheel which can be rotated to bring different samples into the light path including an open hole that acts as a reference to allow absolute measurements. The temperature of the sample wheel is controlled using a built-in heater and thermometer. A second wheel allows a polarizer to be brought into the light path and then rotated to control the light polarization for anisotropic samples.

The apparatus allows measurements with linearly polarized light from 3 to 100 cm^{-1} at temperature from 1.2 to 100 K and with magnetic fields up to 18 T parallel to the light propagation. All of the $CuGeO_3$ transmittance results reported in this thesis were obtained using this apparatus. For another example of measurements made using a very

similar apparatus, see the work by Rõõm *et al.* on the two-dimensional dimer spin system $SrCu_2(BO_3)_2$[13].

It is useful to relate the transmittance to the other optical constants discussed in Chapter 1. Eq. 1.3 gives for the spacial dependence of the electric field of a light wave traveling in a medium with index of refraction $N = n + i\kappa$:

$$\mathbf{E}(x) = \mathbf{E}_0 e^{i\frac{\omega}{c}Nx} = \mathbf{E}_0 e^{i\frac{\omega}{c}nx} e^{-\frac{\omega}{c}\kappa x} \tag{2.1}$$

For nonzero κ this gives an intensity $I(x)$ that decays as the light travels through the medium:

$$I(x) = |E(x)|^2 = E_0^2 e^{-2\frac{\omega}{c}\kappa x} = I_0(1-R)^2 e^{-\alpha x} \tag{2.2}$$

Here α is the absorption coefficient and the factor $(1-R)^2$ has been included to account for light lost to reflection from the two surfaces of the sample. The transmittance through a sample of thickness d is then given by:

$$T = \frac{I(d)}{I_0} = (1-R)^2 e^{-\alpha d} \qquad \Longrightarrow \qquad \alpha = -\frac{1}{d}\ln\left(\frac{T}{(1-R)^2}\right) \tag{2.3}$$

In order to calculate the absorption coefficient α it is necessary to estimate a value for the reflectance R. This can be done using:

$$R = \frac{(n-1)^2 + \kappa^2}{(n+1)^2 + \kappa^2} \approx \frac{(n-1)^2}{(n+1)^2} \tag{2.4}$$

where $n \gg \kappa$ is generally valid for the weakly absorbing materials on which transmittance measurements are usually performed. n can often be estimated by analyzing the interference fringes in the transmittance through a thin sample with parallel faces. Maxima will occur at frequencies where twice the sample thickness corresponds to an integer number of wavelengths.

As mentioned in Chapter 1, the real part of the total optical conductivity σ_1 is simply the sum of the conductivity spectra associated with different absorption channels

or carrier types, such as a Drude component for free electrons, Lorentzians for phonons, and broad peaks in the mid-infrared for interband transitions. The spectral weight of a feature is the area associated with that feature under the σ_1 curve. If the features are well separated in frequency with little overlap, then the spectral weight of one feature is simply the integral of σ_1 taken over the appropriate frequency range. If the features overlap, then the background due to nearby features must be subtracted out. The spectral weight is often expressed in terms of a squared plasma frequency:

$$\omega_p^2 = 8 \int \sigma_1 d\omega \tag{2.5}$$

since this is the result of the integral when σ_1 has the form of a Lorentzian oscillator (real part of Eq. 1.9). In Eq. 2.5 ω_p, σ_1 and ω are all expressed in the same units.

The spectral weight can also be expressed as an integral over the absorption coefficient α. Using Eqs. 2.5, 2.2 and 1.5, and assuming the real part of the index of refraction n is constant over the integral, this gives

$$\omega_p^2 = \frac{n}{\pi^2} \int \alpha d\omega \tag{2.6}$$

2.2 The first inorganic spin-Peierls compound

The quasi-one-dimensional antiferromagnet $CuGeO_3$ is the first inorganic compound to show a spin-Peierls (SP) transition[14]. This type of transition is well known in one-dimensional organic materials and is the magnetic analog of the Peierls transition[15]. In the Peierls transition a modulation of the lattice occurs at low temperatures that increases the size of the unit cell in one direction by a factor n. As shown at the top of Fig. 2.4 this creates a new Brillouin zone boundary that opens a gap in the dispersion curve at the Fermi energy, lowering the energy of the occupied electronic states. The states on the other side of the boundary are increased in energy, but this is of no consequence at

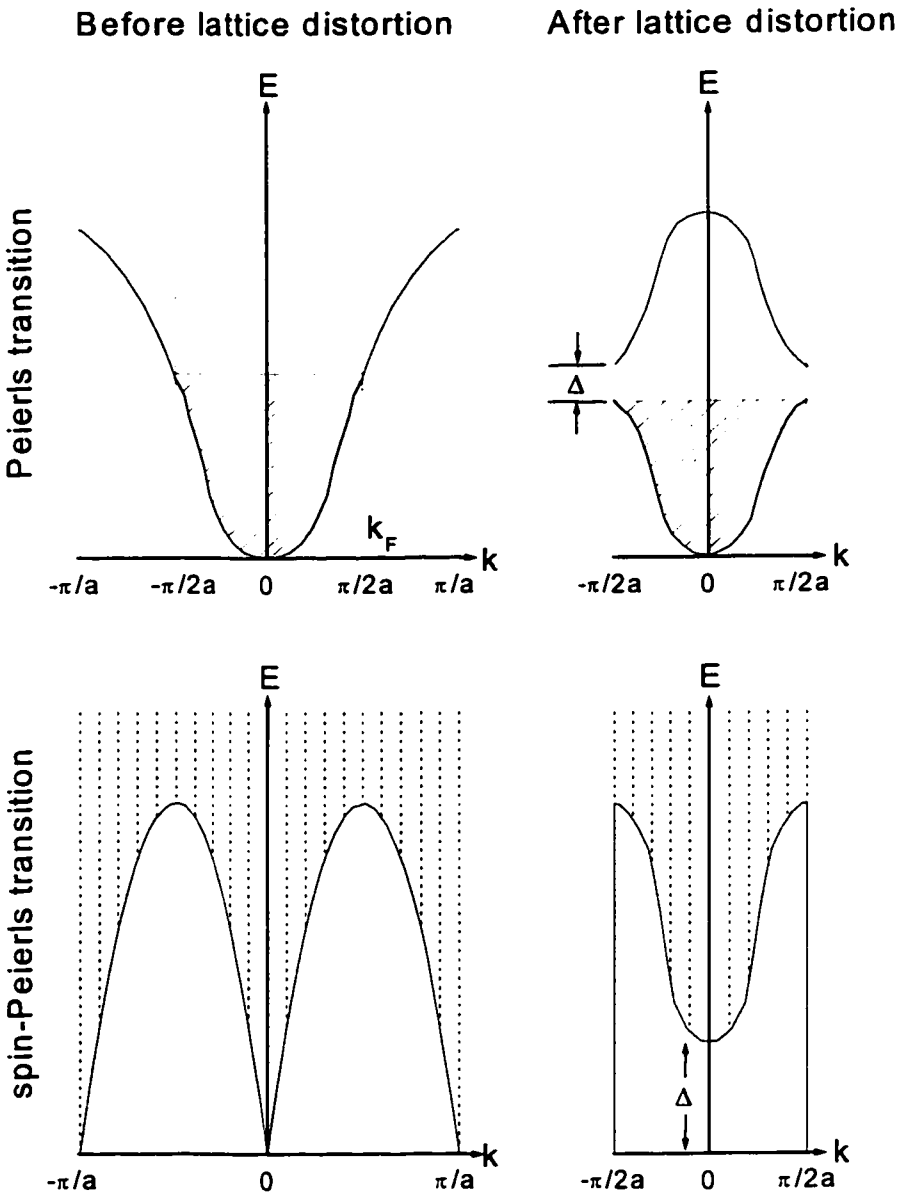

Figure 2.4: Peierls and spin-Peierls gaps.
(After Bray *et al.*[15]) In the Peierls transition, shown at the top, the lattice distortion causes a gap in the electronic energy, while in the spin-Peierls transition, shown at the bottom, it causes a gap in the spin-wave excitation spectrum.

low temperatures where these states are unoccupied. As the temperature is raised, these states do become occupied due to thermal excitation, and the energy savings becomes smaller. Eventually this becomes less than the increase in the elastic energy associated with the lattice distortion, and the crystal returns to its normal state. A SP transition involves a doubling of the unit cell in one dimension, but here the energy saving comes from a gap in the spin excitation spectrum. If the crystal contains quasi-one-dimensional chains of antiferromagtetically coupled spin-$\frac{1}{2}$ atoms, then the spin excitation spectrum is as shown at the bottom of Fig. 2.4. When the spins are equally spaced along the chains, the excitation spectrum is infinitely close to the ground state near $q = 0, \pm\pi/a$. This means that low-lying excited states will be occupied at all temperatures, even at $T = 0$ K where the excitations are due to quantum zero-point fluctuations. When the crystal dimerizes, adjacent spins form spin-singlets, and the spin excitation spectrum is modified so that the spin-singlet ground state is separated from the spin-triplet excited state by a finite energy gap. As long as the temperature is low enough that the spin-triplet states remain mostly unoccupied, then the dimerization results in a net savings in energy. The SP transition temperature occurs when the energy savings due to the gap in the spin excitation spectrum is equal to the energy increase due to the elastic strain caused by the dimerization. In $CuGeO_3$ this occurs at $T_{SP} = 14$ K.

Structures where large tightly bound blocks can move as units, such as the organic charge transfer complexes, exhibit the SP phenomenon. Similar structural units occur in oxides in the form of rigid AlO_4 or SiO_4 tetrahedra bonded weakly to each other to form easily distorted structures[16]. It has been found that in $CuGeO_3$ the SP transition involves both a dimerization of the copper ions along the c-axis and a rotation of the GeO_4 tetrahedra about the c-axis[17]. The lattice structure of $CuGeO_3$ is shown in Fig. 2.5. It consists of chains of relatively rigid GeO_4 tetrahedra along the c-axis. Cu^{2+} ions are positioned between these chains and form chains of CuO_6 octahedra which share the GeO_4

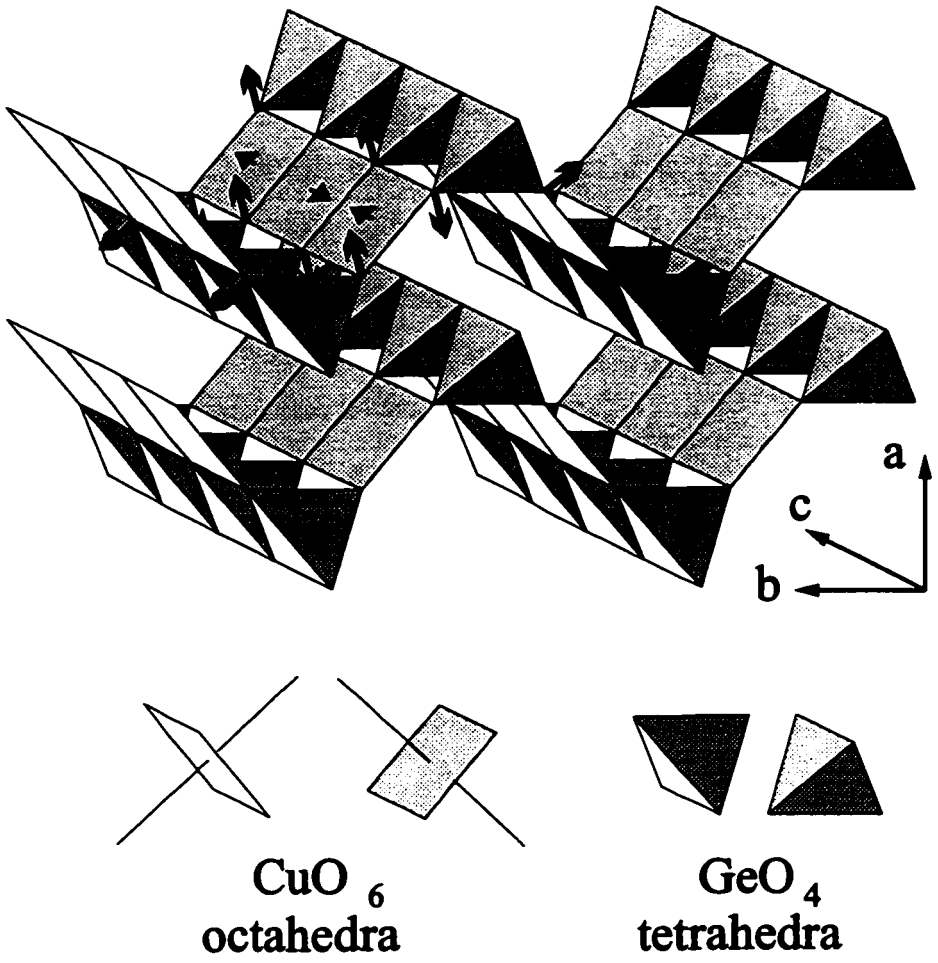

Figure 2.5: Lattice structure of $CuGeO_3$.
Arrows show the motion of the rigid GeO_4 tetrahedra associated with the SP transition.

oxygens. Adjacent octahedra share two oxygens which provide a superexchange path for the antiferromagnetic interaction between Cu^{2+} ions. The arrows show the distortion that occurs in the SP transition which can be thought of primarily in terms of a motion of the GeO_4 tetrahedra. Adjacent tetrahedra tip in opposite directions about the c-axis causing a distortion of the oxygen squares around the Cu^{2+} ions. This distortion moves adjacent Cu^{2+} ions toward each other promoting the formation of spin-singlet pairs. The unit cell becomes doubled in both the c and the a directions.

The magnetic field/temperature phase diagrams of all SP compounds, including $CuGeO_3$, are similar. The phase diagram[18] for $CuGeO_3$ is shown in Fig. 2.6 and consists of three phases. At temperatures above the SP transition temperature the material is in the uniform phase where the Cu^{2+} ions are equally spaced in the c direction. Below T_{SP}, the material is in the dimerized phase where the unit cell has doubled along the c direction and the Cu^{2+} ions have formed spin-singlet pairs. T_{SP} is 14 K at 0 T and decreases somewhat as the magnetic field is increased reaching 11 K at 12 T. Above 12 T the material enters the incommensurate phase[19, 20] where the modulation of the Cu^{2+} ions becomes incommensurate with the periodicity of the lattice. The phase transition between the dimerized phase and the incommensurate phase is first order in nature while transitions to the uniform phase are second order[21].

Using the apparatus described in section 2.1[10], the far-infrared absorption spectrum of undoped $CuGeO_3$ has been measured in all three phases. The results are consistent with those reported by others[22, 23].

In the uniform phase, the far-infrared absorption spectrum of pure $CuGeO_3$ consists of two components. The first is a weak background absorption that goes to zero at zero frequency. The second feature is a line at 48 cm^{-1} that has been identified as a weak B_{3u} phonon that corresponds to a displacement of the four planar oxygens in the direction of the apical oxygens in the CuO_6 octahedra[24]. Neither of these features is

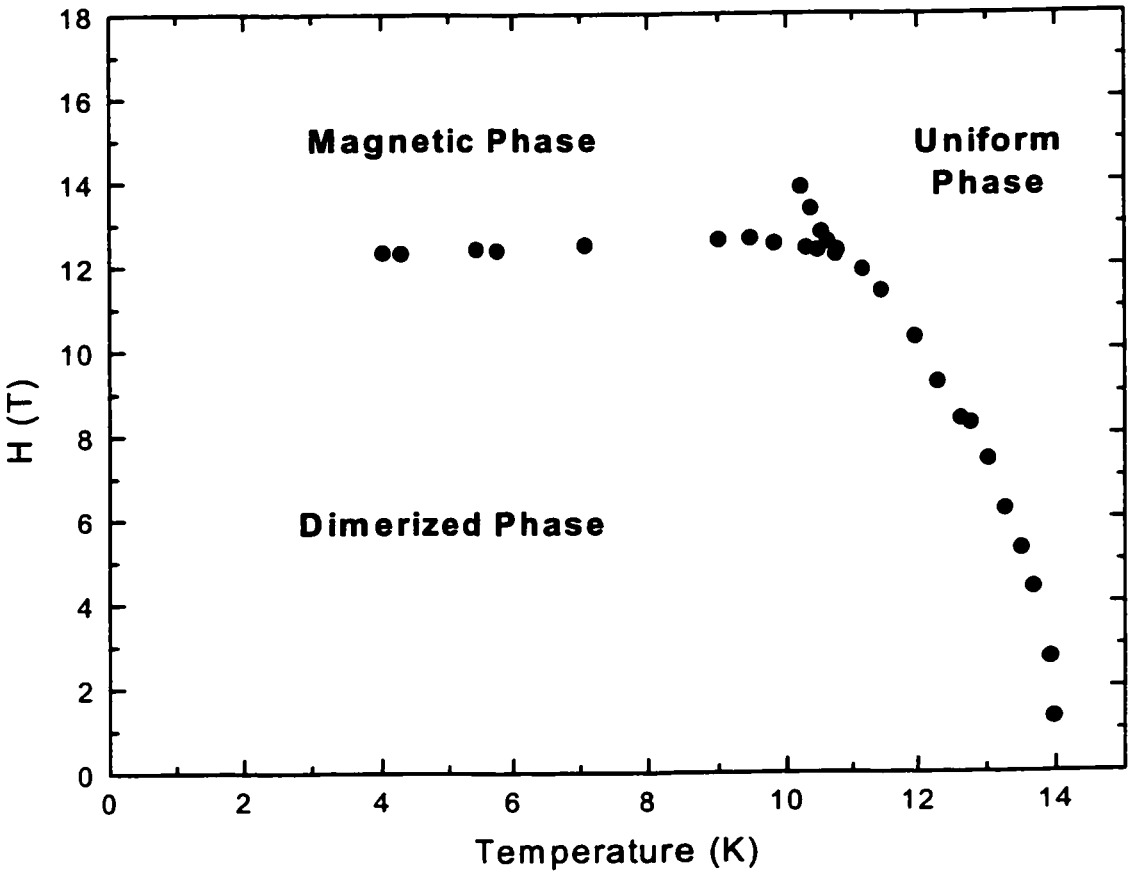

Figure 2.6: H/T phase diagram of $CuGeO_3$.
(After Musfeldt *et al.*[18]) In the uniform phase the copper atoms are evenly spaced along the c-direction. Below T_{SP} a dimerization takes place so that adjacent spin-$\frac{1}{2}$ copper atoms form spin-singlet pairs. At high fields the distortion becomes incommensurate with the lattice and the ground state becomes magnetic.

strongly temperature- or field-dependent although the phonon does broaden somewhat with temperature.

In the dimerized phase, the absorption spectrum has a weak absorption line[22] at 44 cm^{-1} that corresponds to the SP gap energy ($\approx$ 5.5 meV) at $\mathbf{Q} = [0, 0, 0]$ of the magnetic Brillouin zone as determined by electron spin resonance[25]. The temperature dependence of the 44 cm^{-1} line intensity with no applied magnetic field is shown in Fig. 2.7 where it is seen to rapidly disappear as T_{SP} is approached. The line splits in a magnetic field as expected for a transition from the ground singlet state to the excited triplet state as shown in Fig. 2.8. It is induced when $\mathbf{k}\|\mathbf{a}$ with b-polarization only. In the figure, the negative features are at 12 T in the dimerized phase, and the positive features are at 15 T in the incommensurate phase. The lines at 32 and 56 cm^{-1} are the transitions from the ground state to the $m = \pm 1$ components of the excited triplet state. Note the persistence of a weak line at 44 cm^{-1} corresponding to the forbidden transition to the $m = 0$ component.

In the incommensurate phase a magnetic dipole transition in the triplet ground state can be observed[22]. This transition (at 15 cm^{-1} in Fig. 2.8) is independent of polarization in the bc-plane (B_0 = 15 T along the a-axis) as expected for an $S = 1$, $\Delta M = \pm 1$ transition.

Two of the effects of doping $CuGeO_3$ have been studied extensively. The first is a suppression of the SP transition temperature T_{SP}, and the second is the introduction of a new antiferromagnetic phase below a Néel transition temperature T_N. Fig. 2.9 shows T_{SP} and T_N as a function of dopant concentration for various dopant atoms[26, 27, 28]. T_{SP}, which is at 14 K in undoped samples, decreases with doping to about 10 K at 2.5% doping where the dimerized phase is apparently destroyed. In undoped samples there is no antiferromagnetic phase, but with doping T_N increases from 0 K and seems to saturate at about 4 K near 4% dopant concentration. Much attention has been paid

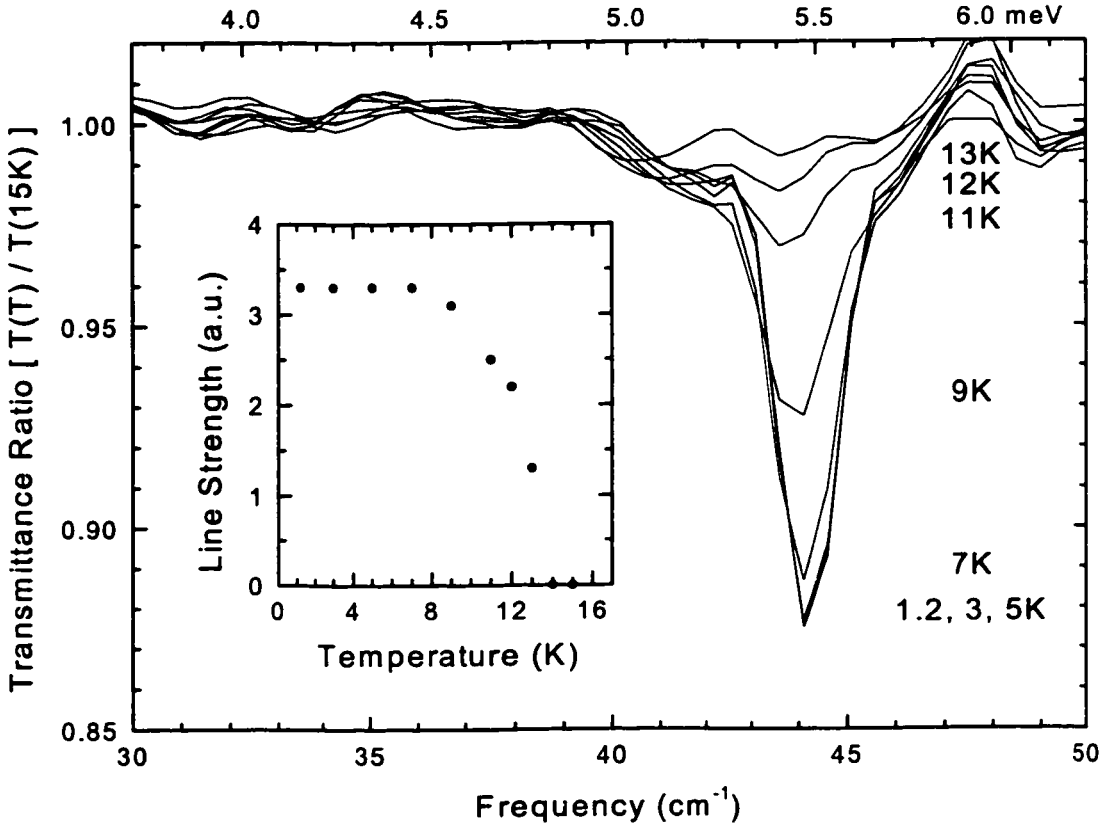

Figure 2.7: The temperature dependence of the 44 cm^{-1} line.
This line corresponds to the singlet-to-triplet transition in the dimerized phase. Its frequency corresponds to the gap energy which decreases as T_{SP} is approached. Its intensity, shown in the inset, also vanishes at T_{SP}.

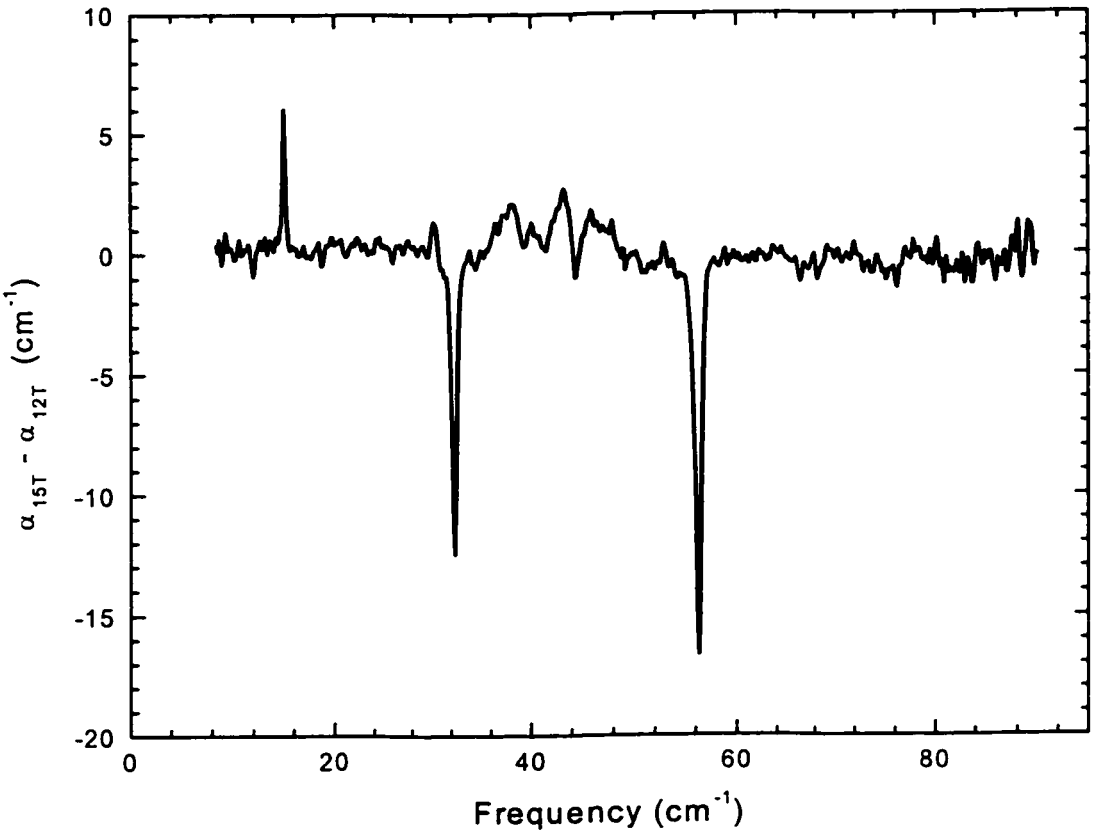

Figure 2.8: High-field spectra of $CuGeO_3$.
Absorption in the SP phase at 12 T (negative features) subtracted from absorption in the incommensurate phase at 15 T (positive features) for the undoped sample at 2.1 K and 0.2 cm^{-1} resolution with b-polarization and $\mathbf{k}\|\mathbf{a}$.

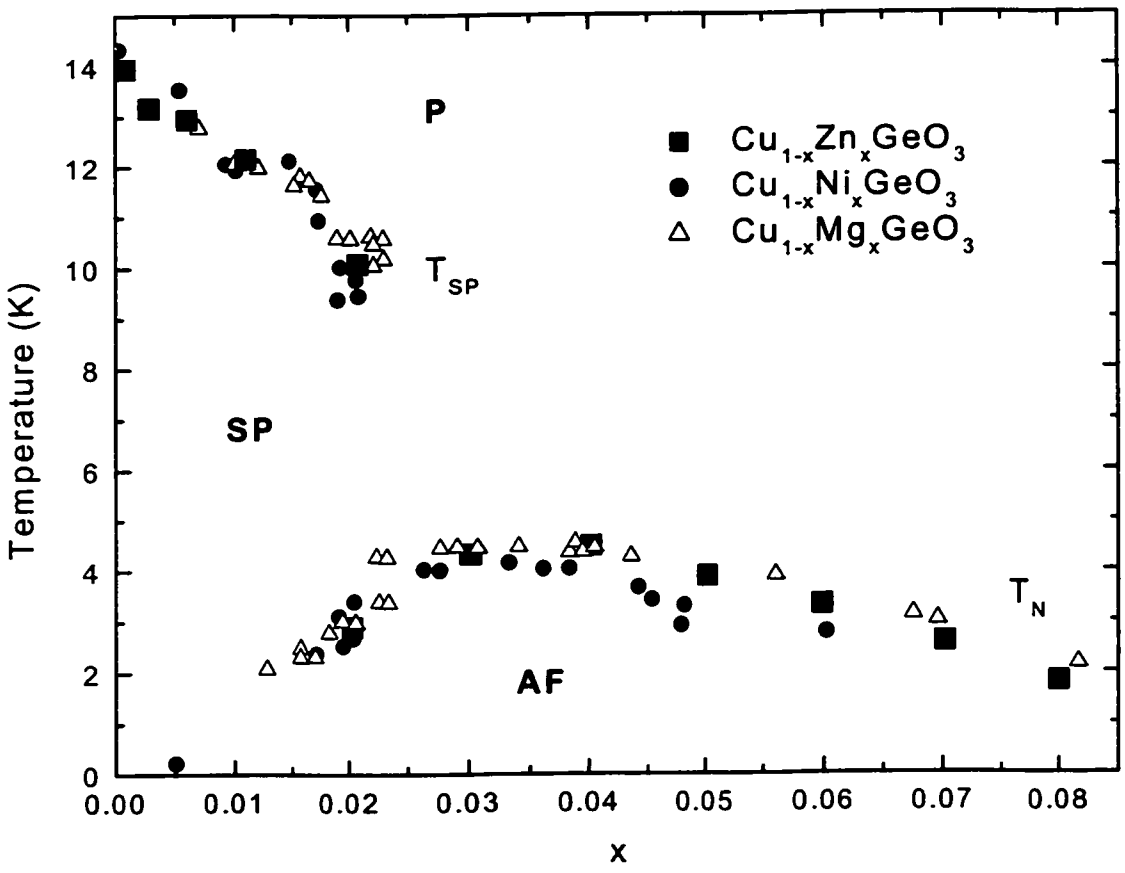

Figure 2.9: Doping/temperature phase diagram of $CuGeO_3$
The SP transition temperature T_{SP} and the Néel transition temperature T_N are shown for various concentrations of Zn[26], Ni[27] and Mg[28] dopants.

to the apparent coexistence of the antiferromagnetic phase and the SP dimerized phase that has been seen in neutron scattering studies[29, 26, 30, 31, 32, 33, 34, 35, 36, 27].

The most recent work comes from measurements on Mg-doped samples[28, 37, 38, 39, 40]. Mg-doping results in a more uniform distribution of dopant ions than when other dopants are used making it possible to control the doping level more precisely[38]. These studies have revealed a first order phase transition at $x_c \approx 0.24$ Mg where there is a jump in the Néel transition temperature. High resolution synchrotron x-ray-diffraction experiments have revealed that while the SP lattice dimerization persists above x_c, the SP state attains long-range order only below x_c[37]. A similar behaviour is seen in Zn-doped samples suggesting that this is universal behaviour for doped $CuGeO_3$[38]. It has been pointed out that many of the observed characteristics, such as randomness, slow dynamics and hysteresis, are reminiscent of what is seen in spin-glass systems[37, 39].

Fig. 2.10 shows the magnetization as a function of applied field for samples with various Zn concentrations. The decrease in magnetization near 14 K is due to the SP transition and can be seen to occur at lower temperatures with increased doping consistent with Fig. 2.9. The suppression near 4 K, which is seen only in the two most highly doped samples, is a signature of the transition to the antiferromagnetic phase. Note that the signature of the SP transition has completely disappeared in the most highly doped sample.

Another effect of doping is the introduction of localized vibrational modes of the dopant atoms which give rise to unusual low frequency lines in the transmittance spectra. This has not been observed previously since very few far-infrared studies have been made on doped $CuGeO_3$ [41, 42], none of which extend below 20 cm^{-1}. This is the subject of Section 2.3.

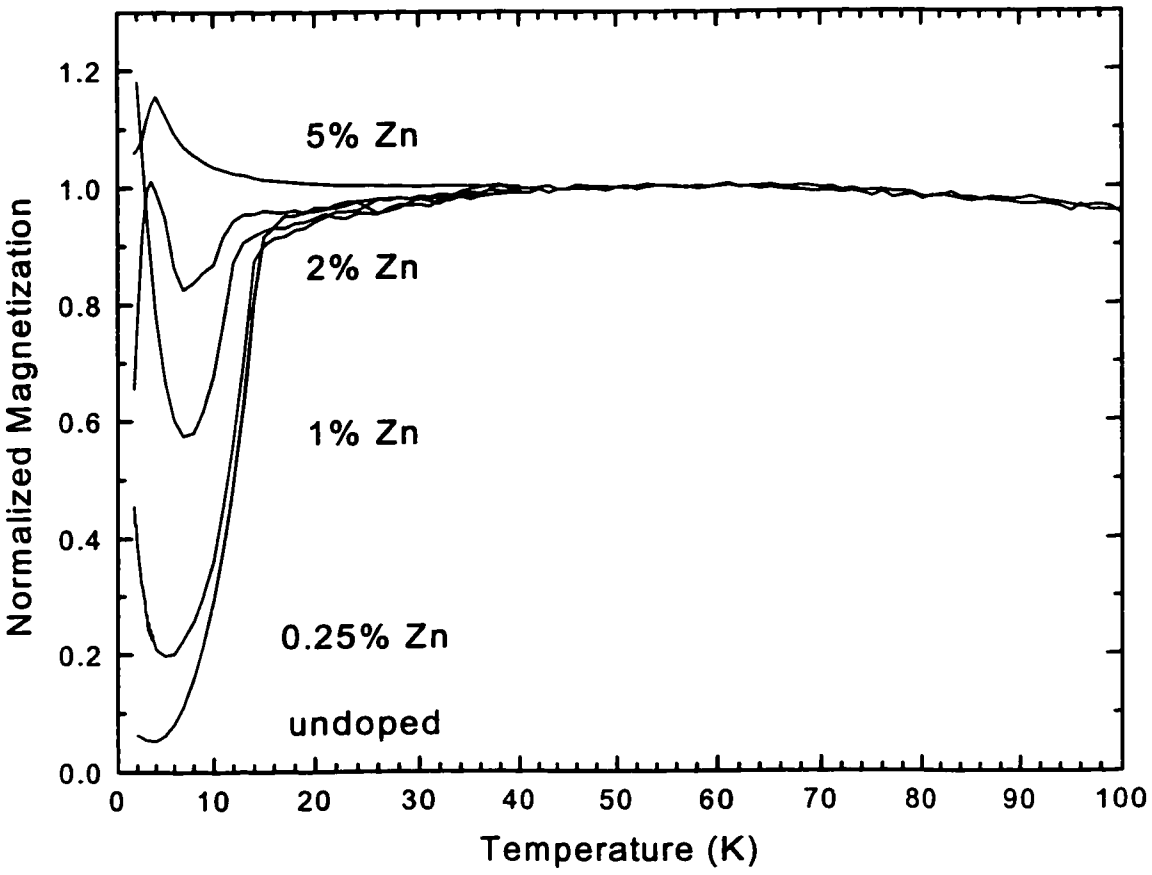

Figure 2.10: Magnetization of doped $CuGeO_3$
The magnetization in a 50 Oe field normalized to unity at 40 K for samples with various Zn concentrations. The decrease in magnetization below 14 K is due to the SP transition, and the decrease below 4 K in the two most highly doped samples is due to the Néel transition.

2.3 Transmittance measurements of doped $CuGeO_3$

Several single crystals were studied including an undoped sample and various doped samples: $Cu_{0.999}Cd_{0.001}GeO_3$, $CuGe_{0.997}Si_{0.003}O_3$, $Cu_{0.98}Ni_{0.02}GeO_3$, and $Cu_{1-x}Zn_xGeO_3$ with $x = 0.003, 0.01, 0.02$ and 0.05. The Néel and SP transition temperatures, T_N and T_{SP}, were determined from the magnetic susceptibility measurements shown in Fig. 2.10. The $x = 0.01$, 0.02 and undoped samples were grown by S.M. Coad at the University of Warwick using a floating zone technique and the $x = 0.001$, 0.003 and 0.05 samples by H. Dabkowska at McMaster University using a self flux method[9]. Either atomic emission spectroscopy or mass spectroscopy was used by the crystal growers to determine the dopant concentrations and good agreement was found with the phase diagrams[26, 32, 33, 36, 27] for T_{SP} and T_N *vs.* concentration x.

Sample sizes were about $0.6 \times 2.5 \times 4$ mm^3 in the directions of the a, b and c crystallographic axes[43] respectively. The **k**-vector of the light was aligned along the a-axis (**k**$\|$**a**). To establish the symmetry of the transitions, additional measurements were performed with **k**$\|$**b** for one of the Zn-doped samples ($x = 0.01$). The DC magnetic field was in the direction of light propagation (Faraday geometry), and most of the spectra were measured at 1 cm^{-1} resolution. To use Eq. 2.3 to calculate the absorption coefficient α from the transmittance it was necessary to estimate the refractive index using the interference fringes from a thin sample with parallel faces. A constant value of $n = 3.0 \pm 0.3$ was determined for the entire range from 3 to 100 cm^{-1}.

The absorption spectra for several samples at 1.2 K are shown in Fig. 2.11. The sample doped with $x = 0.003$ Si is very similar to the undoped sample (not shown) in that the only far-infrared features are the lines at 44 and 48 cm^{-1}. In contrast, the $x = 0.003$ Zn sample shows a line at 10 cm^{-1} in addition to the features present in the Si-doped sample (or in the undoped samples). Increased doping results in a broadening

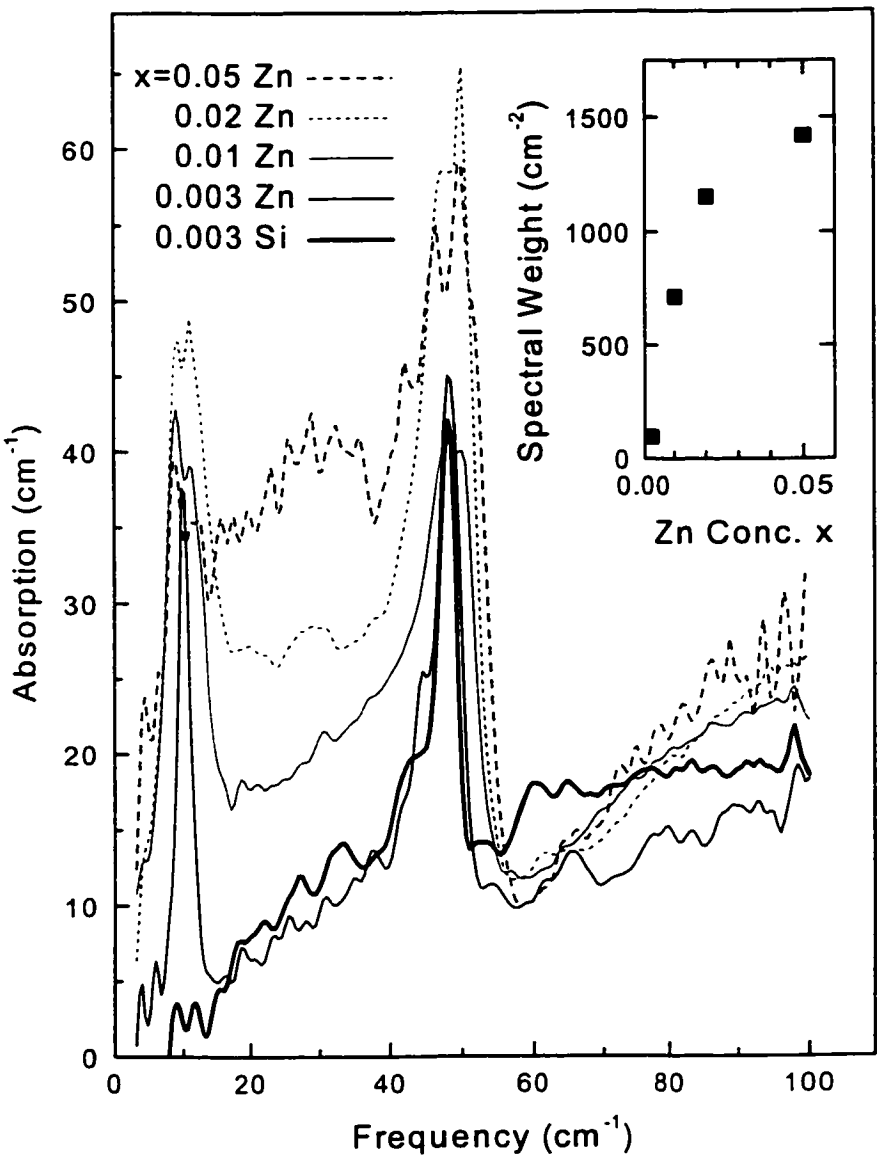

Figure 2.11: Doping dependence of far-infrared absorption of $CuGeO_3$. The spectra were measured at 2 K with *b*-polarization and $\mathbf{k}\|\mathbf{a}$. The inset shows spectral weight from 3 to 60 cm^{-1} as a function of Zn concentration. The spectral weight does not include the background which is taken to be the Si-doped sample spectrum.

of the 10 cm^{-1} line and the development of a broad absorption band between 5 and 55 cm^{-1}. The variation of the spectral weight from 3 to 60 cm^{-1} (background and phonon line subtracted) is shown in the inset to Fig. 2.11 as a function of concentration. Here spectral weight is expressed as a squared plasma frequency proportional to the area under the curve according to Eq. 2.6. The dependence on Zn concentration appears to be linear at low concentrations, but quickly saturates above $x = 0.02$.

Absorption spectra for the $x = 0.003$ Zn-doped sample were also obtained at higher temperatures. While the shoulder at 44 cm^{-1} disappears above the SP transition temperature as expected, the 10 cm^{-1} line and another line at 20 cm^{-1} show a temperature dependence that has no obvious relationship to the SP transition. The spectra are shown in Fig. 2.12, and Fig. 2.13 shows the spectral weight ω_p^2 of the 10 and 20 cm^{-1} lines as functions of temperature. The 10 cm^{-1} line loses intensity as temperature is increased, but the 20 cm^{-1} line, which is absent at low temperatures, grows in intensity until it peaks near 40 K. Both lines shift to higher frequencies with temperature (inset to Fig. 2.13), and the 20 cm^{-1} line broadens significantly. Although the 10 and 20 cm^{-1} lines are broader in the more highly doped samples, they still show this temperature dependence. The broad absorption from 5 to 55 cm^{-1} in the samples with $x > 0.003$ is temperature independent up to 100 K, and no difference is seen between spectra above and below the Néel temperature which can be attributed to the antiferromagnetic transition.

The temperature dependence of the 20 cm^{-1} line suggests that it is a transition from an excited state. A simple three level model with two excited states 10 and 30 cm^{-1} above the ground state accounts for the temperature dependences of the line intensities as shown by the solid curves in Fig. 2.13. The form of the curves comes from the fact that the populations of the levels N_1, N_2 and N_3 will be related by Boltzmann factors:

$$N_2 = N_1 e^{-\Delta_{10}\beta}, \qquad N_3 = N_2 e^{-\Delta_{20}\beta} = N_1 e^{-(\Delta_{10}+\Delta_{20})\beta} \tag{2.7}$$

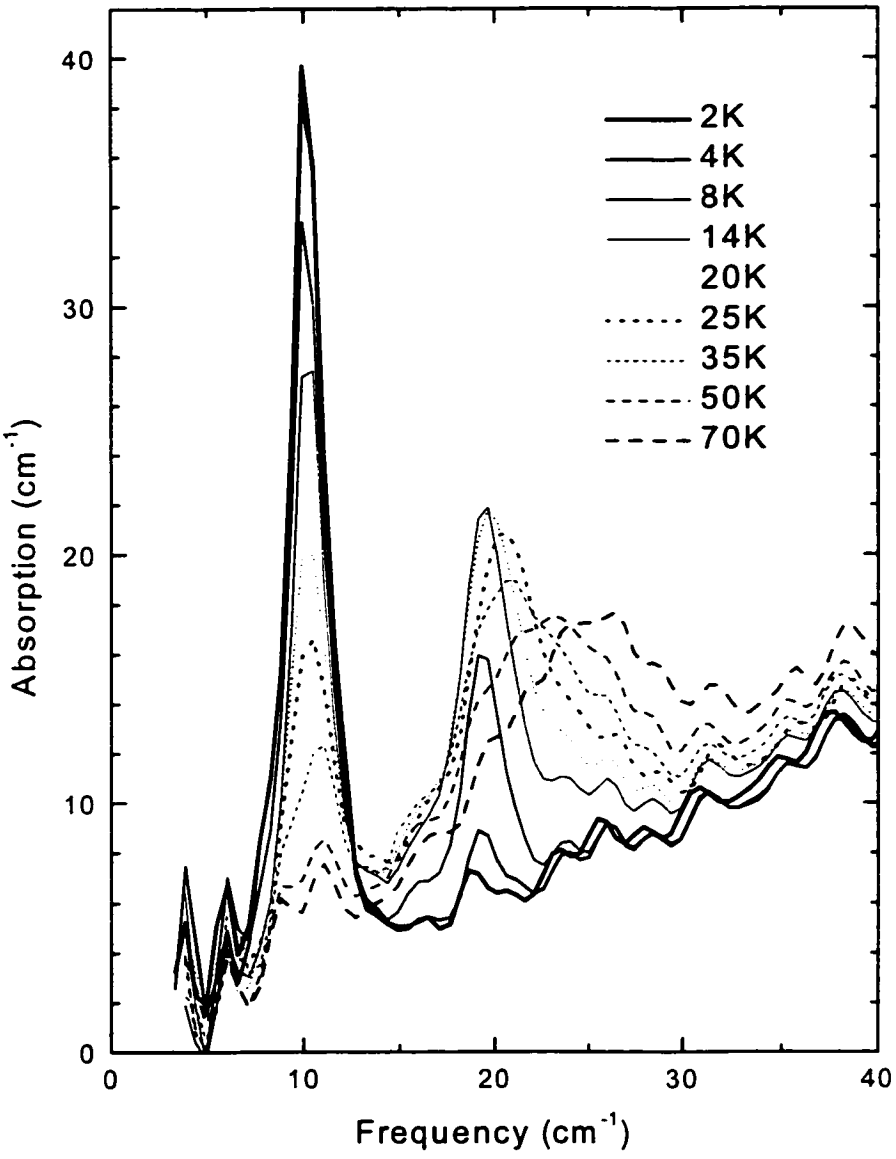

Figure 2.12: Temperature dependence of 10 and 20 cm^{-1} lines.
The spectra were measured with b-polarization and $\mathbf{k}\|\mathbf{a}$ on the $x = 0.003$ Zn-doped sample.

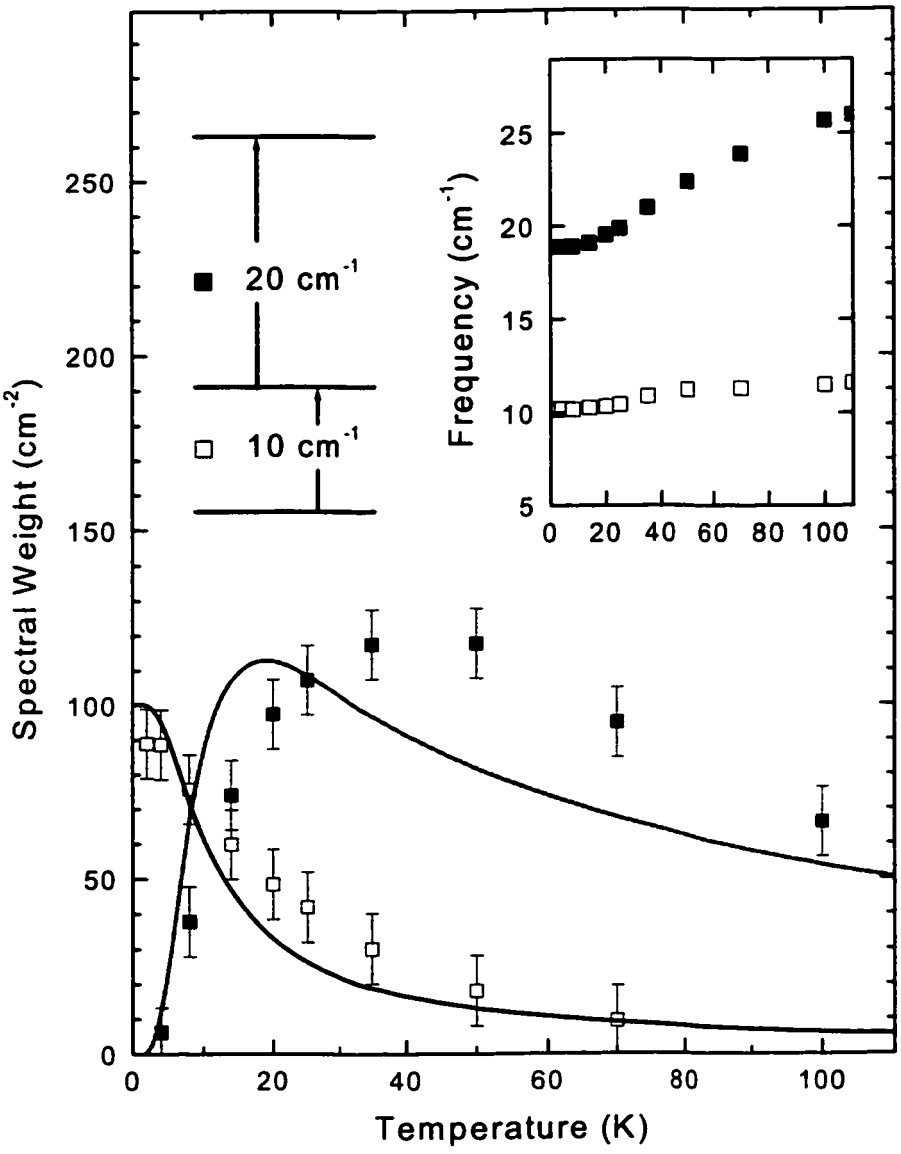

Figure 2.13: A three-level model for the 10 and 20 cm^{-1} lines.
The data show the spectral weight ω_p^2 of the lines calculated using Lorentzian fits with the frequencies shown in the inset. Solid lines are fits to the simple three-level model.

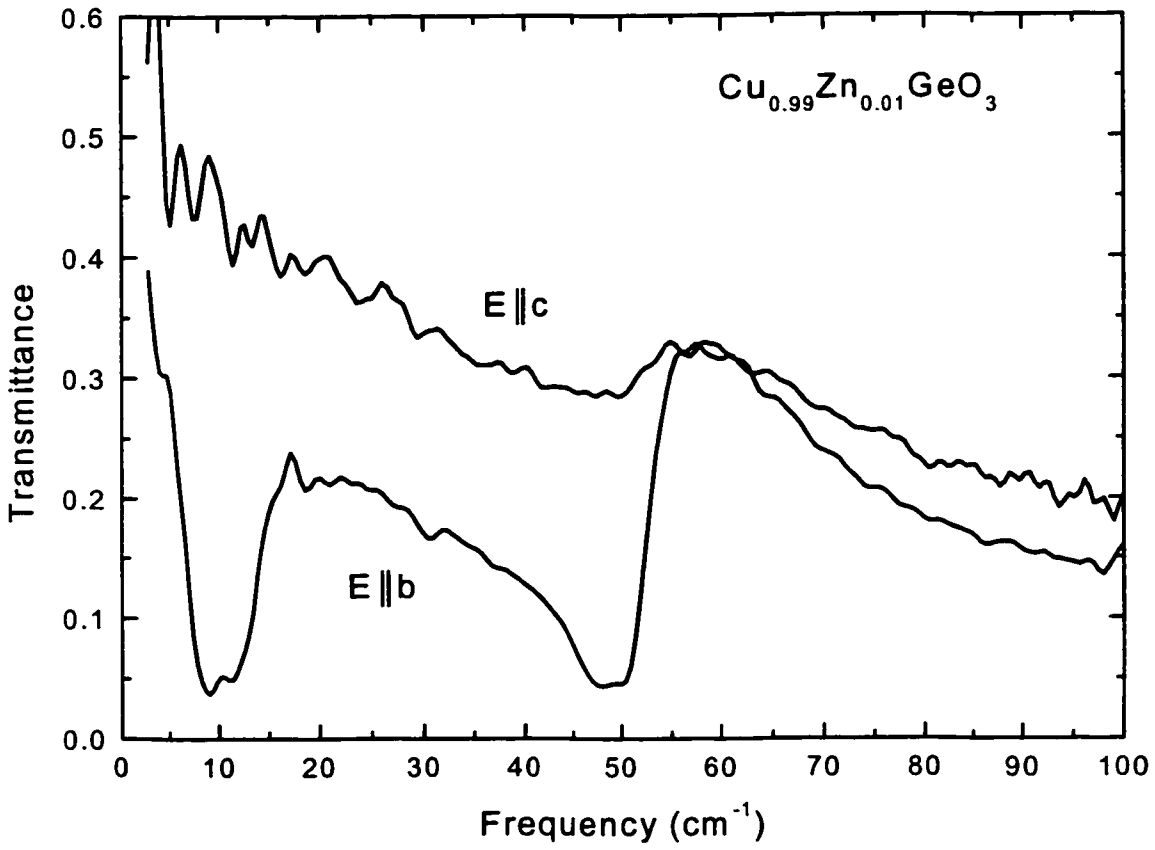

Figure 2.14: Polarization dependence of the Zn-induced absorption features. Transmittance spectra at 2 K with $\mathbf{k}\|\mathbf{a}$ show that the features are strongest with b-polarization and nearly absent with c-polarization.

where Δ_{10} and Δ_{20} are the temperature dependent transition frequencies (inset of Fig. 2.13) and $\beta = (k_B T)^{-1}$. The intensity of the transition between two levels is proportional to the population difference, and the total population is constant giving:

$$I_{10}(T) = \frac{A_{10}(1 - e^{-\Delta_{10}\beta})}{1 + e^{-\Delta_{10}\beta} + e^{-(\Delta_{10}+\Delta_{20})\beta}} \tag{2.8}$$

$$I_{20}(T) = \frac{A_{20}e^{-\Delta_{10}\beta}(1 - e^{-\Delta_{20}\beta})}{1 + e^{-\Delta_{10}\beta} + e^{-(\Delta_{10}+\Delta_{20})\beta}} \tag{2.9}$$

where $A_{10} = 100$ and $A_{20} = 500$ are adjustable parameters. The trends in the data are correctly reproduced, and the quality of the fit, though not particularly good, can be improved by adding higher energy levels to the model. This points to a multilevel, very anharmonic excitation, that is made possible by the replacement of a Cu^{2+} ion with Zn^{2+}, but not by the substitution of Si for Ge.

The polarization dependence of the Zn-induced features was also obtained. With $\mathbf{k}||\mathbf{a}$, the 10 and 20 cm^{-1} lines as well as the 5 to 55 cm^{-1} band were strongest when the electric field was along the *b*-axis (*b*-polarization) and nearly absent with *c*-polarization as shown in Fig. 2.14. When the $x = 0.01$ Zn sample was oriented with $\mathbf{k}||\mathbf{b}$, the features were strongest for the *a*-polarization. Thus, if these are magnetic dipole transitions, they require that the magnetic field component of the light is along the *c*-axis. If they are electric dipole transitions then the electric field must be in the *ab*-plane and have components both in the *a* and *b* directions.

Magnetic dipole transitions can be ruled out by comparing the spectral weight of the Zn-induced absorption with that of a known magnetic dipole transition in the system, the magnetic dipole transition in the incommensurate phase shown in Fig. 2.8 at 15 cm^{-1} with a spectral weight of $\omega_p^2 = 2.5$ cm^{-2}. The spectral weight of the 10 cm^{-1} line is 100 cm^{-2}, a factor of 40 larger than the magnetic dipole transition. This discrepancy, which is even larger considering the dilution due to the low Zn concentration, in combination with the

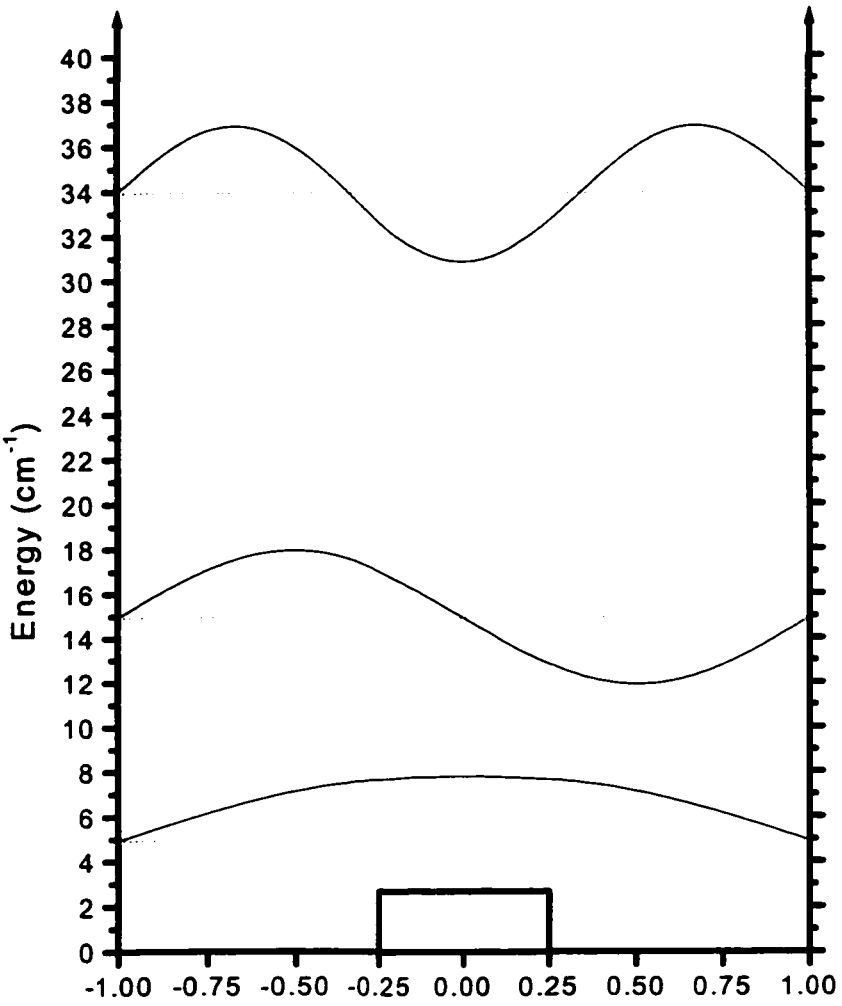

Figure 2.15: Potential well for the three-level model.
The simple one-dimensional potential that gives energy levels separated by 10 and 20 cm^{-1} is a square well with a central barrier. The corresponding wave-functions are also shown. Note that a forth level 55 cm^{-1} above the ground state is also consistent with the data.

fact that the frequency of the Zn-induced absorption is not affected by magnetic field up to 16 T, leads to the conclusion that it is not a magnetic dipole transition.

It is also possible to rule out forbidden electronic electric dipole transitions such as the transition in the SP phase from the singlet ground state to the excited triplet state which produces the 44 cm^{-1} line. That line splits in a magnetic field as shown in Fig. 2.8 due to the splitting of the excited triplet state. If the Zn-induced features are similar transitions, it is unclear which states could be involved. Since they are not split by a magnetic field, they are unlikely to involve transitions to or from triplet states. In-gap states, predicted by Martins *et al.*[44], are also excluded because they would be absent above the SP transition temperature.

Local vibronic modes are another possibility. For a pure Zn translational mode for $x = 0.003$ Zn a spectral weight of 530 cm^{-2} is estimated from the plasma frequency $\omega_p = (4\pi n Z^2 e^2/M)^{1/2} = 13$ cm^{-1}, where n is the Zn concentration, M is the mass of the Zn ion and Z is the effective charge which is taken to be +2. This is over 5 times larger than the observed spectral weight. It is therefore likely that the mode also involves motion of other atoms.

The three level system shown in Fig. 2.13 can be modeled with a square well with a central barrier as shown in Fig. 2.15. An appropriate choice of parameters gives levels at 10, 30 and 55 cm^{-1} above the ground state, and electric dipole transitions between adjacent levels will give lines at 10, 20 and 25 cm^{-1}. The line at 25 cm^{-1} could very well be present in the spectra and account for the apparent broadening with temperature of the 20 cm^{-1} line. In general, the addition of the level at 55 cm^{-1} will improve the agreement between the calculated and observed temperature dependence of the line intensities shown in Fig 2.13. The broadening of the 10 and 20 cm^{-1} lines with increased doping can also be explained as being due to interaction between the defects.

The combination of a low intensity, a very anharmonic flat potential and a polarization

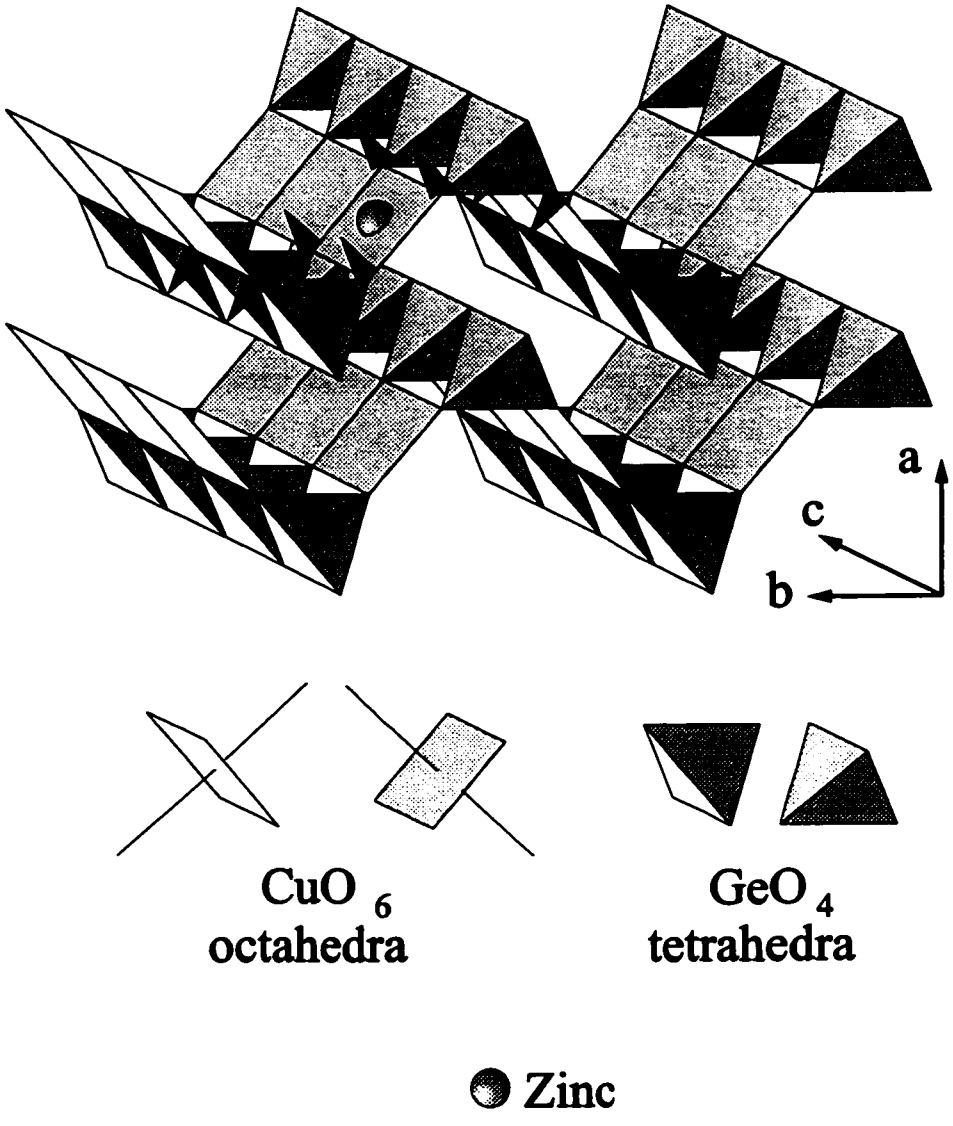

Figure 2.16: Lattice structure of $CuGeO_3$.
Arrows show possible motion of the rigid GeO_4 tetrahedra associated with a Zn-induced local vibrational mode.

in the *ab*-plane suggests that the lines at 10 and 20 cm^{-1} involve the Zn defect and the libration about the *c*-axis of the surrounding four GeO_4 tetrahedra as shown in Fig. 2.16. This mode would have a polarization with components in both the *a* and *b* directions and is consistent with the model of a potential well with a central barrier. Since Zn is known to favour a higher coordination number than Cu it will have a tendency to move off center towards one of the apical oxygens.

There are at least two indications that the GeO_4 tetrahedra can be readily tipped. Libration of GeO_4 tetrahedra is a component of the *static* SP distortion in the undoped material[17, 45], although it is not optically active since it involves odd combinations of the rotations of the GeO_4 tetrahedra and no displacement of the Cu in the *ab*-plane. The 48 cm^{-1} phonon is a similar low energy mode. It is optically active[24] and involves the motion of the Cu in the direction of the apical oxygens. It is possible that the Zn doping has the effect of moving the mode at 48 cm^{-1} to 10 cm^{-1} by a dramatic reduction of the already weak restoring force for displacements of the planar oxygens in the direction of the apical oxygens around the Zn.

The identity of the ion that replaces the copper, however, does not appear to be critical since similar absorption lines are seen in Ni- and Cd-doped samples. Fig. 2.17 shows the transmittance at 15 K divided by the transmittance at 2 K for samples with the three dopants. Where the Zn-doped sample has lines at 10 and 20 cm^{-1}, the Cd-doped sample has lines at 11 and 16 cm^{-1}, and the Ni-doped sample has lines at 11 and 18 cm^{-1}. These variations are surprisingly small considering the significantly larger size of the Cd^{2+} ion and the difference in the magnetic character of the Ni^{2+} ion which has spin $S = 1$ instead of $S = 0$. This insensitivity to the dopant ion suggests that the vibration is dominated by the relatively massive GeO_4 tetrahedra.

Table 2.1 shows the line positions for the various ions along with their crystal radii for various coordination numbers as reported by Shannon[46]. In the undoped material.

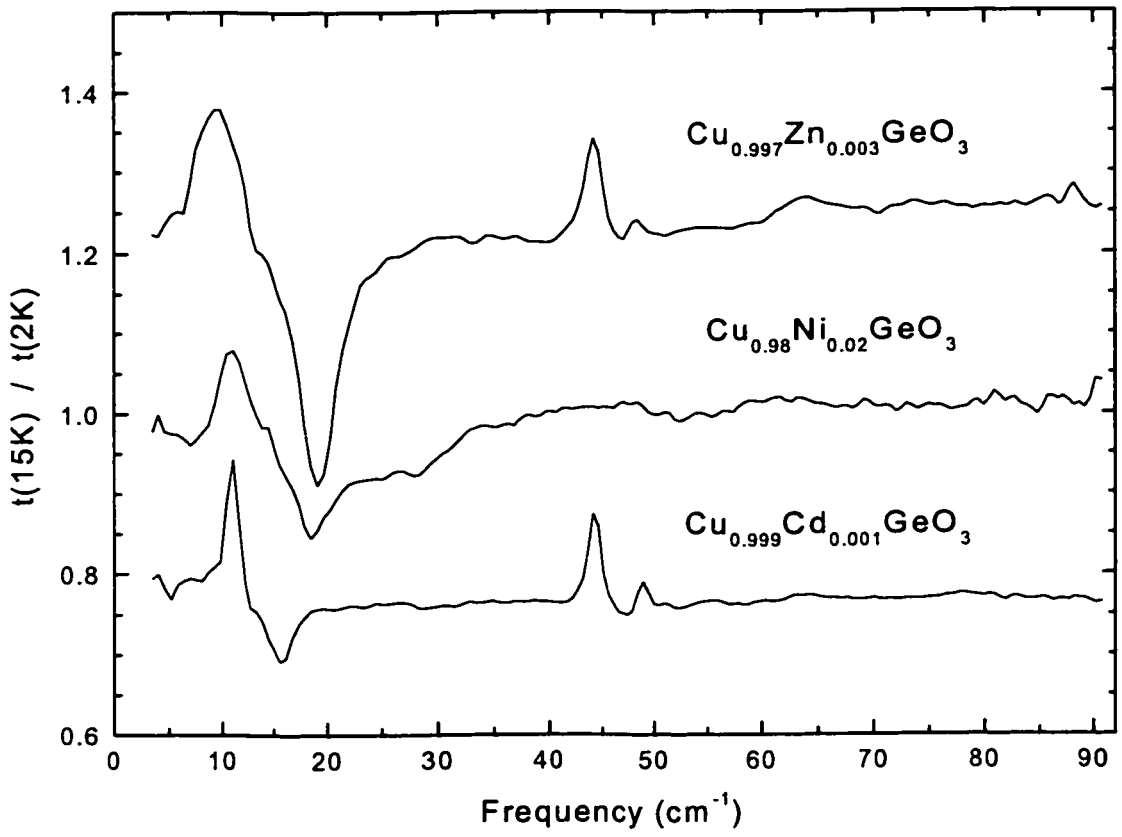

Figure 2.17: Spectra of $CuGeO_3$ doped with Zn, Ni and Cd. Transmittance at 15 K divided by transmittance at 2 K of $x = 0.003$ Zn-, 0.02 Ni- and 0.001 Cd-doped $CuGeO_3$ with the Zn and Cd data offset for clarity. Lines similar to those at 10 and 20 cm^{-1} in the Zn-doped sample can also be seen in the Ni- and Cd-doped samples.

Table 2.1: Line positions in wavenumbers for various dopant ions.
Electron configuration (EC), coordination number (CN), and crystal radius are from Shannon[46]. The value reported for CN= 4 is for a square planar configuration.

ion	line1/line2	EC	CN	crystal radius (Å)
Ni^{2+}	11/18	$3d^8$	4	0.63
			5	0.77
			6	0.83
Cu^{2+}	48?	$3d^9$	4	0.71
			5	0.79
			6	0.87
Zn^{2+}	10/20	$3d^{10}$	5	0.82
			6	0.880
Cd^{2+}	11/16	$4d^{10}$	5	1.01
			6	1.09
Mg^{2+}		$2p^6$	5	0.80
			6	0.860
O^{2-}		$2p^6$	3	1.22

the Cu^{2+} ions are surrounded by six O^{2-} ions forming a distorted octahedron. The nearest four oxygens are only 1.93 Å from the Cu^{2+} ion, while the two apical oxygens are considerably farther away at 2.75 Å[45]. From Table 2.1 it is clear that the Cu^{2+} ions should be considered as having a coordination number of four since the corresponding crystal radius, when added to that of oxygen, gives the correct spacing of $0.71 + 1.22 = 1.93$ Å. As mentioned above, the 10 and 20 cm^{-1} lines seen in the doped samples could be due to the modification of the 48 cm^{-1} phonon in the presence of the impurity. As with most phonons, the 48 cm^{-1} phonon appears as a single line in undoped samples because its potential in nearly harmonic, or quadratic, so that the energy levels within the potential well are all equally spaced. Whether the transitions are between the lowest levels at low temperatures or between higher levels at high temperatures, the absorbed energy is always 48 cm^{-1}, and since the total spectral weight is independent of temperature. the single line has a constant strength.

When Cu^{2+} is replaced by Ni^{2+} this quadratic potential is apparently modified. As can be seen in Table 2.1, Ni^{2+} also exists with a square planar coordination, but its crystal radius is typically about 10% smaller than that of Cu^{2+}. This may give the ion more freedom of motion in the direction perpendicular to the oxygen plane making its potential well more square. An infinite square well has energies proportional to the square of the quantum number of the level so that levels 1, 2 and 3 have energies proportional to 1, 4 and 9. This gives 3:5 as the ratio of the lowest excitations which nearly matches the ratio 11:18 for the line energies in the Ni-doped sample.

Zn^{2+}, on the other hand, has a crystal radius very similar to that of Cu^{2+} at high coordination numbers. It is not, however, typically found with a square planar coordination, and no corresponding crystal radius is reported by Shannon[46]. This difference is probably responsible for the central barrier in the potential well needed to reproduce the 10:20 ratio for the line energies in the Zn-doped samples as shown in Fig. 2.15.

Doping with Cd^{2+} creates a different situation. Like Zn^{2+}, Cd^{2+} is not typically found with square planar coordination, but this may not be as important as its size. As can be seen in Table 2.1, the crystal radius of Cd^{2+} is about 30% larger than that of Cu^{2+} and Zn^{2+}. While it may not be obvious what effect this should have, the line energies in the Cd-dope sample suggest that the potential well is closer to quadratic for Cd^{2+} than it is for the other dopants. Of the three ratios measured, 11:16 is closest to 1:1.

No Mg-doped samples were measured in this study, but it is worth considering what one would expect since much of the most recent research has been done on such samples[28, 37, 38, 39, 40]. From Table 2.1, it is clear that although Mg^{2+} is far lighter than the other dopants, its crystal radius is about the same as Cu^{2+} and Zn^{2+}. Since it is not commonly found with square planar coordination, it is likely that far-infrared spectra of Mg-doped samples would look similar to those of Zn-doped samples with lines near 10 and 20 cm^{-1}.

In contrast to the large changes in dynamics caused by dopants on the Cu sites, the replacement of Ge by Si will have the minor effect of reducing the size of one of the tetrahedra thereby affecting four Cu sites equally and, by symmetry, giving rise to a low frequency optical mode polarized in the b direction. No such mode is observed in the Si-doped samples between 3 and 100 cm^{-1}, however lines have been observed at 500 and 960 cm^{-1} by Damascelli *et al.*[47]. They also observe the emergence with increasing Si concentration of broad absorption bands over the entire range below 2000 cm^{-1} and attribute this to a reduction of the k-conservation rule due to impurities which results in the measurement of bands averaged over the entire Brillouin zone instead of only $k \approx 0$.

This mechanism may explain the 5 to 55 cm^{-1} band at high doping levels reported in this thesis. Its lower boundary is approximately defined by the 10 cm^{-1} line, and the upper boundary more or less coincides with the phonon at 48 cm^{-1}. The saturation of the absorption above a concentration of $x = 0.02$ (inset to Fig. 2.11) is reminiscent of

the phase diagram[26, 27, 28] in which T_N stops changing at this same concentration. Another explanation, suggested by the unusual flat shape of the band, is that it represents a disordered state of the local excitations as they begin to interact strongly at $x = 0.02$ Zn and above. This state may also be relevant to the saturation of T_N at the same doping level, and is consistent with the suggestion by Wang *et al.* that doped $CuGeO_3$ has many characteristics, such as randomness, slow dynamics and hysteresis, that are reminiscent of what is seen in spin-glass systems[37, 39].

Some comment should be made concerning the other, more recent, inorganic SP compound α'-NaV_2O_5. Actually, its identity as a true SP compound is controversial. While it does have an isotropic activated magnetic susceptibility[48], superlattice peaks in x-ray diffraction data[49], and a spin-gap observed with neutron scattering[49], all of which suggest a SP transition at $T_{SP} = 34$ K, it also has less magnetic field dependence of T_{SP} than expected[50] and the transition involves some charge ordering[51]. Nevertheless, it has many similarities to $CuGeO_3$, and one might expect to see some of the same far-infrared features. Infrared measurements have been made between 50 and 50,000 cm^{-1} [52, 53], and like $CuGeO_3$, several phonons are observed with the lowest one at 90 cm^{-1} with the light polarized perpendicular to the chains[53]. Unlike $CuGeO_3$, α'-NaV_2O_5 shows a broad temperature dependent continuum of excitations extending from the lowest frequencies out to about 7500 cm^{-1} for this same polarization[53]. This has been interpreted as a two-magnon absorption[53] since it increases with decreasing temperature and becomes gapped in the dimerized phase below about 136 cm^{-1} which corresponds to twice the value of the spin-gap seen in inelastic neutron scattering experiments[49]. The signal-to-noise ratio was too low to detect any sharp line at the gap energy, and no work has been done on doped samples.

Local vibrational modes are known to occur in a wide variety of systems with various impurities[3]. Often the local mode exists at a frequency well separated from the

frequency bands of the other lattice modes, either above or between bands, and this isolation accounts for its long lifetime and narrow linewidth. Such modes have been extensively studied, particularly in semiconductors such as Si or Ge[54]. Local modes are also found to exist within the band of normal frequencies, and these low-frequency local modes are usually referred to as resonant modes. They are most commonly found in alkali halides, and almost always involve an impurity ion with an ionic radius smaller than that of the host ion it replaces[3]. By considering the magnitude of the repulsive forces from the surrounding ions which push the impurity toward the centre, and the attractive polarization and electrostatic forces which pull it away from centre, it is often found that the net restoring force is small, leading to a low-frequency mode. A notable example is the mode due to Li^+ in KBr which shows up as a sharp line in the far-infrared near 17 cm^{-1}[55].

It would appear that the local vibrational mode in $CuGeO_3$ belongs to the resonant mode category, although it is unique in at least two ways. The first unusual property of the $CuGeO_3$ mode is its multiline spectrum. Usually, a local mode is observed as a single line in the infrared spectrum corresponding to the transition energy from the ground state to the first excited state. Overtones at about twice this energy are also sometimes observed corresponding to the transition from the ground state to the second excited state. Transitions between excited states are not observed because the potentials for these modes are usually only slightly anharmonic[3] so that their energies are the same as the fundamental. Also, measurements are usually made at low temperatures to minimize features due to the host lattice. This means that unless the mode occurs at a very low frequency, the excited states will be mostly unpopulated. Greene and Sievers have reported what could be the observation of an excited-state transition in Li^+-doped KBr[56]. They observe a weak, thermally activated line near 8 cm^{-1} and speculate that this and a similar feature seen in Cu^+-doped NaCl may be due to transitions between

the first and second excited states. They propose a potential with a central barrier, but are unable to reconcile this with the overtones seen in Raman spectra[57, 58].

The second unusual aspect of the $CuGeO_3$ mode is that the impurity ion is similar in size to the host ion it replaces (see Table 2.1) so that the mechanism that reduces the restoring force, and hence the frequency of the mode, seems to be different than in other resonant modes. As mentioned earlier, it is presumed that the easily tipped GeO_4 tetrahedra might be involved. One might expect to find low-energy local vibrational modes due to the low-energy structural degrees of freedom found in systems containing networks of rigid units, such as AlO_4 or SiO_4 tetrahedra. Groups of these units can often shift and pivot cooperatively so as to distort the network without distorting the individual rigid units, and thus without requiring a lot of energy. Such a mode is referred to in amorphous systems as a 'floppy mode' and in crystalline systems as a 'rigid unit mode'[16]. Such modes have been used to describe structural phase transitions[59, 60], dynamic disorder[61], fragility[62], and the boson peak in silicate glasses and crystals[63, 64]. Simulations of amorphous silica have revealed individual modes involving about thirty tetrahedra with a barrier energy of about 500 cm^{-1}[65, 66]. Experimentally they show up as a continuum of excitations below 200 cm^{-1} in inelastic neutron scattering[64]. Since the local modes in $CuGeO_3$ appear to involve the motion of relatively rigid GeO_4 tetrahedra, it would be interesting to model $CuGeO_3$ using 'rigid unit mode' techniques.

In summary, far-infrared transmittance measurements have been made on pure and doped $CuGeO_3$ between 3 and 100 cm^{-1} below 100 K and up to 16 T. In addition to features that have been seen by other researchers, a low lying resonant mode in Zn-, Cd- and Ni-doped $CuGeO_3$ has been observed. It has been identified with the librational motion of GeO_4 tetrahedra combined with the displacement of the dopant ion in a very anharmonic potential.

Chapter 3

κ-$(ET)_2Cu[N(CN)_2]Br$

The organic conductors exhibit a variety of interesting phenomena including the spin-Peierls transition, spin-density waves, charge-density waves and superconductivity. Many of these are directly related to their low dimensionality, and the two-dimensional materials are of particular interest because of their similarity to the layered high-temperature superconductors. κ-$(ET)_2Cu[N(CN)_2]Br$, which is the subject of this chapter, is the organic superconductor with the highest transition temperature at ambient pressure. $T_c = 12$ K. Like the high-temperature superconductors, its transport properties are highly anisotropic with clearly metallic behaviour only within its conducting planes. Perpendicular to the planes, the nature of the transport remains poorly understood. In this chapter, this is investigated by analyzing measurements of the interplane reflectance.

Section 3.1 is a description of the experimental apparatus used to measure the reflectance and an overview of the techniques used to analyze the data. Section 3.2 reviews the organic superconductors, particularly the two-dimensional ones based on the ET molecule and begins a discussion of the nature of the interplane transport. Section 3.3 continues this discussion in light of far-infrared interplane reflectance measurements of κ-$(ET)_2Cu[N(CN)_2]Br$ which are presented and analyzed.

3.1 Measurement and analysis of reflectance

If light is incident on the surface of a material, then the reflectance of that material is simply the fraction of the light which is reflected. In other words, it is the ratio of the

reflected intensity I_r to the incident intensity I_i. If the sample surface to be measured is large and flat, then this ratio is relatively easy to measure experimentally. One simply uses a light beam with a cross-section smaller than the sample and arranges the apparatus so that, when the sample is present, the light reflects from the sample along a certain path to a detector, while if the sample is removed, the light travels along a different but equivalent path to the same detector.

If the sample is very small, however, then accurate reflectance data can be obtained by mounting the sample on the tip of a polished metal cone and using a light beam that is larger than the sample[67]. This takes full advantage of the available sample surface, and any light which misses the sample is scattered away by the cone and doesn't reach the detector. This introduces the complication that the incident intensity is no longer due to the entire incoming beam, but only to that part which hits the sample. In order to measure this incident intensity one can try to replace the first sample with a second sample of known reflectance, cut to the same size and shape as the first sample and positioned in the same way, but this is difficult to do accurately. Evaporating a thin layer of gold or some other metal onto the surface of the sample solves this problem, but has the disadvantage of not being easy to undo. Typically during an experiment, which might take several hours, it is desirable to alternate periodically between measurements of incident and reflected intensity to insure that long-term drifts in the light intensity or detector sensitivity cancel out.

The adopted procedure for measuring reflectance involves a combination of these techniques[67]. The sample and a similarly sized stainless steel reference mirror are each mounted on a polished brass cone, and these two cones are then mounted at right angles to each other on the cold finger of a helium-cooled cryostat. The cryostat allows the temperature to be varied between 10 and 400 K and can be rotated by 90° to place either the sample or the reference into the light beam. During the first half of the experiment, ratios

of sample intensity to reference intensity are measured at all temperatures of interest. Then a layer of gold is evaporated onto the sample and everything is repeated, this time producing a set of ratios of gold-covered sample intensity to reference intensity. Finally, the first set of ratios is divided by the second set to give the reflectance of the sample relative to the known reflectance of gold. Dividing by the reference intensity cancels out long term drifts, while dividing by the gold-covered sample intensity accurately cancels out the size, shape, alignment and roughness of the sample.

The accuracy of the measurement can be estimated by comparing spectra measured at various stages of the experiment. One procedure is to first measure the sample-to-reference ratios at various temperatures starting with room temperature. After this the room-temperature measurement is repeated, and gold is evaporated onto the sample. The second half of the experiment is then performed in the same order as the first half, beginning with a room-temperature measurement, followed by measurements at other temperatures, and concluding with another room-temperature measurement. Ideally the two room-temperature measurements before evaporation should be identical as should the two after evaporation. The difference is a measure of the accuracy of the experiment which is typically about ± 0.5 %.

At high frequencies the reflectance is measured one frequency at a time using a diffraction grating to isolate individual frequency components from a broad band source. Fig. 3.1 depicts the Spex grating spectrometer used to measure reflectance between 8000 and 40000 cm^{-1}. In order to cover such a wide range of frequencies, a variety of light sources and detectors are used. The light sources are either an incandescent tungsten lamp or a deuterium arc lamp. The detectors include diodes made of silicon, lead sulphide and indium antimonide as well as a photomultiplier tube.

At low frequencies, below 8000 cm^{-1}, where the light intensity is much weaker, the

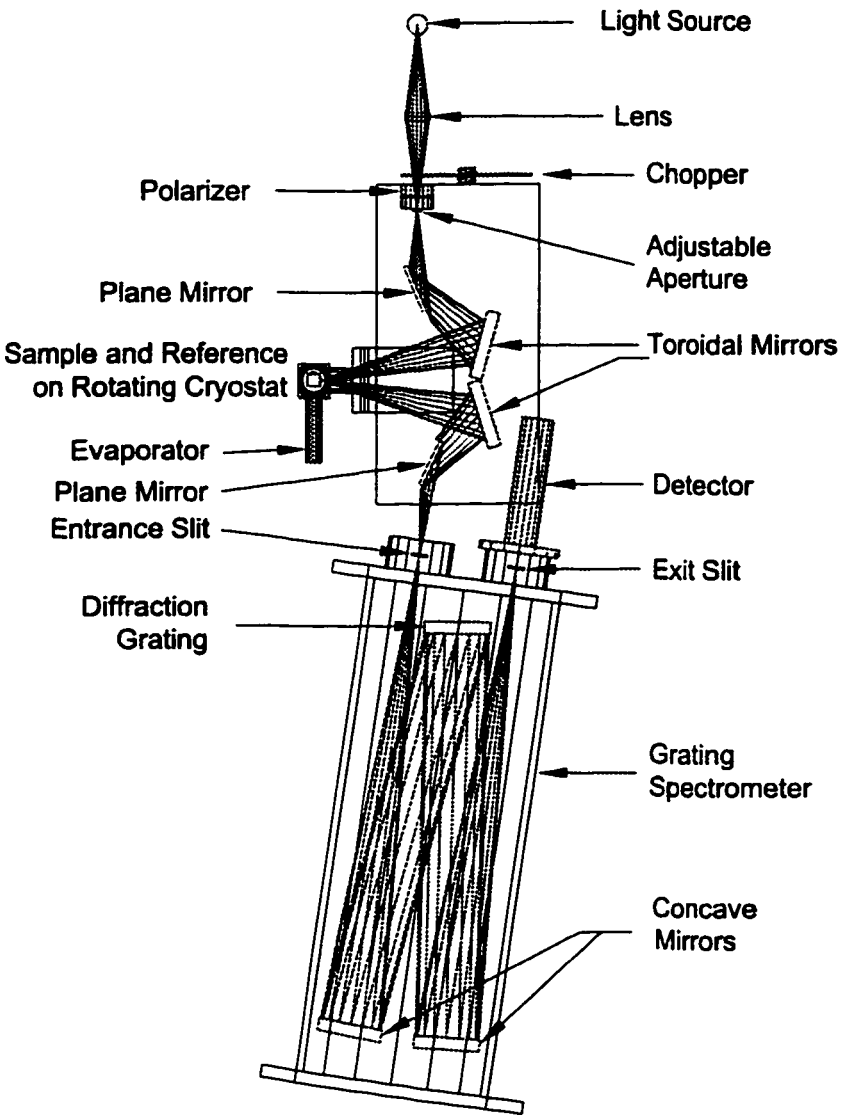

Figure 3.1: Spex spectrometer.
This spectrometer uses a diffraction grating to measure light intensity reflected from a sample, one frequency at a time, for frequencies between 8000 and 40000 cm^{-1}.

reflectance is measured at many frequencies simultaneously using a Michelson interferometer. The beam from the source is split into two equal components which are later recombined and sent to a detector. One of the components travels a fixed distance, while the distance traveled by the other is varied by moving a mirror. The interference between the two components depends on the path difference, and the signal as a function of path difference can be Fourier transformed to give the intensity of the source as a function of frequency[12].

The rapid-scan Fourier transform spectrometer used to measure reflectance between 30 and 8000 cm^{-1} is depicted in Fig. 3.2. When the reflectance is measured below 800 cm^{-1}, the light source is a mercury arc lamp, the beamsplitter is a sheet of mylar either 12 or 3 μm thick, and the detector is a silicon bolometer with an operating temperature of either 1.2 or 4.2 K. To measure reflectance between 800 and 8000 cm^{-1}, an incandescent tungsten lamp, a potassium bromide beamsplitter and a mercury cadmium telluride detector are used. The moving mirror is mounted on an oil bearing that is moved back and forth using a solenoid and a permanent magnet. Two additional light sources (and detectors) are used to precisely determine the mirror location. The first of these is a small incandescent lamp that produces a signal that peaks when the mirror path difference is zero. The second is a He-Ne laser that produces a sinusoidal signal, the periods of which can be counted to keep track of the mirror's position as it moves.

As discussed in Chapter 1, the optical response of a material can be characterized by a complex function of frequency. Due to causality, the real and imaginary parts of the response function are related by the Kramers-Kronig relations:

$$G_1(\omega) = \frac{1}{\pi}\mathcal{P}\int_{-\infty}^{\infty}\frac{G_2(\Omega)}{\Omega-\omega}d\Omega, \qquad G_2(\omega) = -\frac{1}{\pi}\mathcal{P}\int_{-\infty}^{\infty}\frac{G_1(\Omega)}{\Omega-\omega}d\Omega \tag{3.1}$$

where $G(\omega)$ is a response function and $\mathcal{P}$ means principal part. These equations can be applied to the real and imaginary parts of the optical constants discussed in Chapter 1.

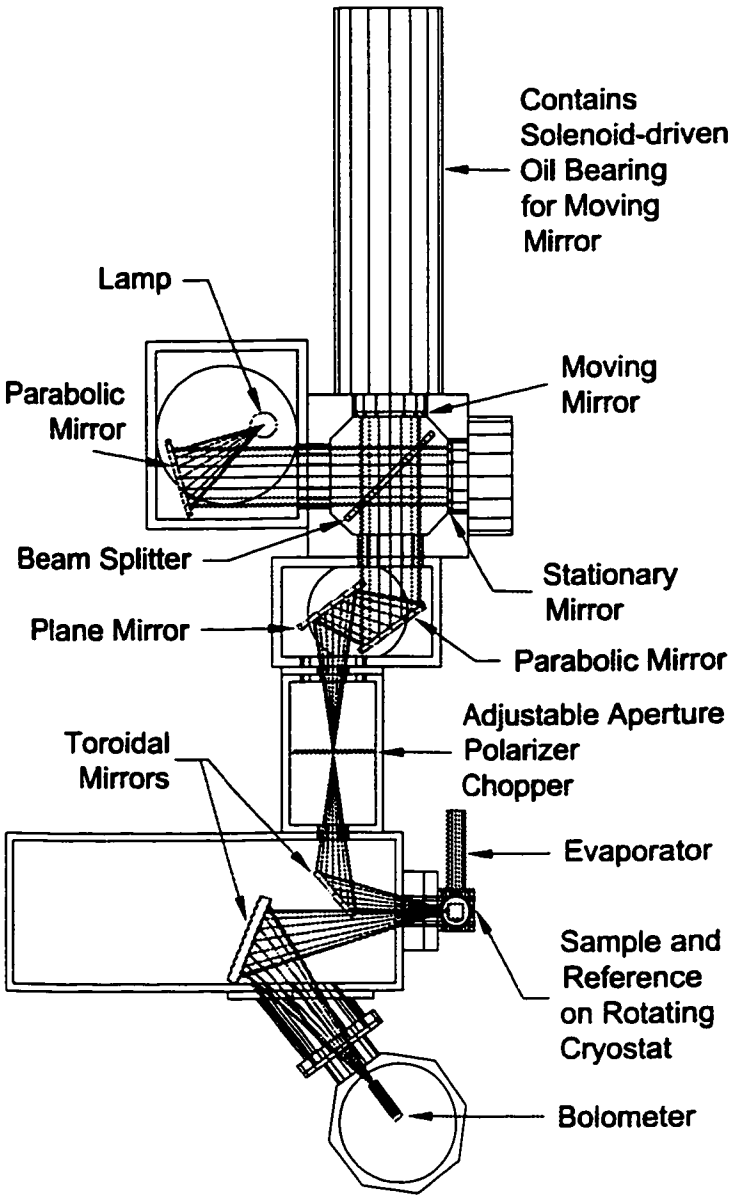

Figure 3.2: Michelson spectrometer.
This spectrometer produces a signal that can be Fourier transformed to measure light reflected from a sample for frequencies between 30 and 8000 cm^{-1}.

$N = n + i\kappa$, $\epsilon = \epsilon_1 + i\epsilon_2$, and $\sigma = \sigma_1 + i\sigma_2$.

The quantity measured in the experiment, however, is the reflectance R which is the ratio of the reflected and incident light intensities:

$$R = \frac{I_r}{I_i} = \left|\frac{E_r}{E_i}\right|^2 = |r|^2 \tag{3.2}$$

where I_r and I_i are the intensities and E_r and E_i are the magnitudes of the electric fields of the reflected and incident light. The complex quantity r is the reflectivity which can be related to the other optical constants by considering the continuity of the electric and magnetic fields at the surface of a material. At normal incidence,

$$E_i + E_r = E_t, \qquad H_i - H_r = H_t \tag{3.3}$$

where the sign change in the second equation follows from the fact that the electric and magnetic fields are mutually perpendicular and the reflected component travels in the direction opposite to that of the incident and transmitted components. Since with $\mu = 1$ Maxwell's equations (Eq. 1.1) give $H = NE$, we have:

$$r = \frac{E_r}{E_i} = \frac{1 - N}{1 + N} \tag{3.4}$$

so that N can easily be calculated from r.

In order to get the reflectivity r from the measured reflectance R one must obtain the phase θ of the reflectance:

$$r = \sqrt{R}e^{i\theta}, \qquad \ln r = \frac{1}{2}\ln R + i\theta \tag{3.5}$$

θ can be obtained by applying the Kramers-Kronig relations (Eq. 3.1) to the complex function $\ln r$.

$$\theta = \frac{1}{2\pi}\mathcal{P}\int_{-\infty}^{\infty}\frac{\ln R}{\omega - \Omega}d\Omega = \frac{\omega}{\pi}\mathcal{P}\int_{0}^{\infty}\frac{\ln R}{\omega^2 - \Omega^2}d\Omega \tag{3.6}$$

This procedure allows one to determine all of the optical constants from a measurement of the reflectance R, since R can be used to calculate θ, and R and θ give r which can be used to calculate N, ϵ or σ.

Of course, the application of the Kramers-Kronig relations requires a knowledge of the reflectance at all frequencies in order to perform the integral from zero to infinity. In practice, the reflectance is measured over as wide a range of frequencies as possible and then extrapolated to all other frequencies. At high frequencies free electron behaviour is assumed with $R \approx \omega^{-4}$. At low frequencies an insulator is assumed to have $R \approx$constant, and a metal is assumed to follow Hagen-Rubens behaviour ($R \approx 1 - (2\omega\rho_{DC}/\pi)^{\frac{1}{2}}$, where ρ_{DC} is the DC resistivity).

3.2 Organic superconductors

It may seem strange to find superconductivity, which involves the pairing of conduction electrons and hence arises from the metallic state, in organic materials which are usually insulators, but many organic conductors and superconductors do exist[68, 69]. Most metals contain atoms whose orbitals do not contain enough electrons to completely fill the electronic bands they form in the solid, and because these bands are unfilled, they are able to carry current. Bands formed from nonmetal atoms, on the other hand, are full and therefore nonconducting. In the organic conductors this is overcome by building the solid from organic molecules that ionize in the crystal to form stable radicals so that the bands formed from the molecular orbitals are unfilled. The molecules used are large and flat so that their size makes them easy to ionize and their shape allows them to be stacked close together, at least in one direction, giving good overlap of the molecular orbitals. The organic conductors are therefore made up of two components, the anion and the cation, and because it is difficult to have good overlap of large-molecule molecular

orbitals in all directions, the organic conductors are typically quasi-one-dimensional or quasi-two-dimensional in nature.

The first organic conductors were quasi-one-dimensional materials. Tetrathiafulvalene (TTF) which forms a cation radical was combined in 1972 with tetracyanoquinodimethane (TCNQ) which forms an anion radical to form TTF-TCNQ. The crystal contains segregated stacks of TTF and TCNQ molecules which conduct primarily in the stacking direction. Although the conductivity is still orders of magnitude less than that of a good metal like Cu, it is much larger than that of an insulator and increases with decreasing temperature as is typical of a metal. Another example is $(TMTTF)_2PF_6$ which has a similar cation $(TMTTF)_2^+$ combined with the simple monovalent charge-compensation anion PF_6^-. This material undergoes a spin-Peierls transition at low temperature like $CuGeO_3$ which was discussed in Chapter 2. The first organic superconductor discovered was $(TMTSF)_2PF_6$ in which superconductivity was observed only when hydrostatic pressure was applied in order to suppress a spin density wave transition at low temperatures. $(TMTSF)_2ClO_4$ is superconducting at atmospheric pressure. Of all the quasi-one-dimensional superconductors, the highest superconducting transition temperature is about $T_c = 2$ K.

Higher superconducting transition temperatures were achieved by stacking the molecules into conducting sheets rather than chains. Many of these quasi-two-dimensional superconductors contain bis(ethylenedithio)tetrathiafulvalene (BEDT-TTF) or ET. The ET molecules have been observed in several different stacking configurations. Two of the most common, the β and κ networks, are shown in Fig. 3.3 along with diagrams of three common molecular components of organic metals. In the β network the ET molecules form a honeycomb pattern, while in the κ network they are arranged as an array of face-to-face dimers. The κ materials have the highest transition temperatures with κ-$(ET)_2Cu[N(CN)_2]Br$ having the highest at atmospheric pressure[70]. $T_c = 12$ K.

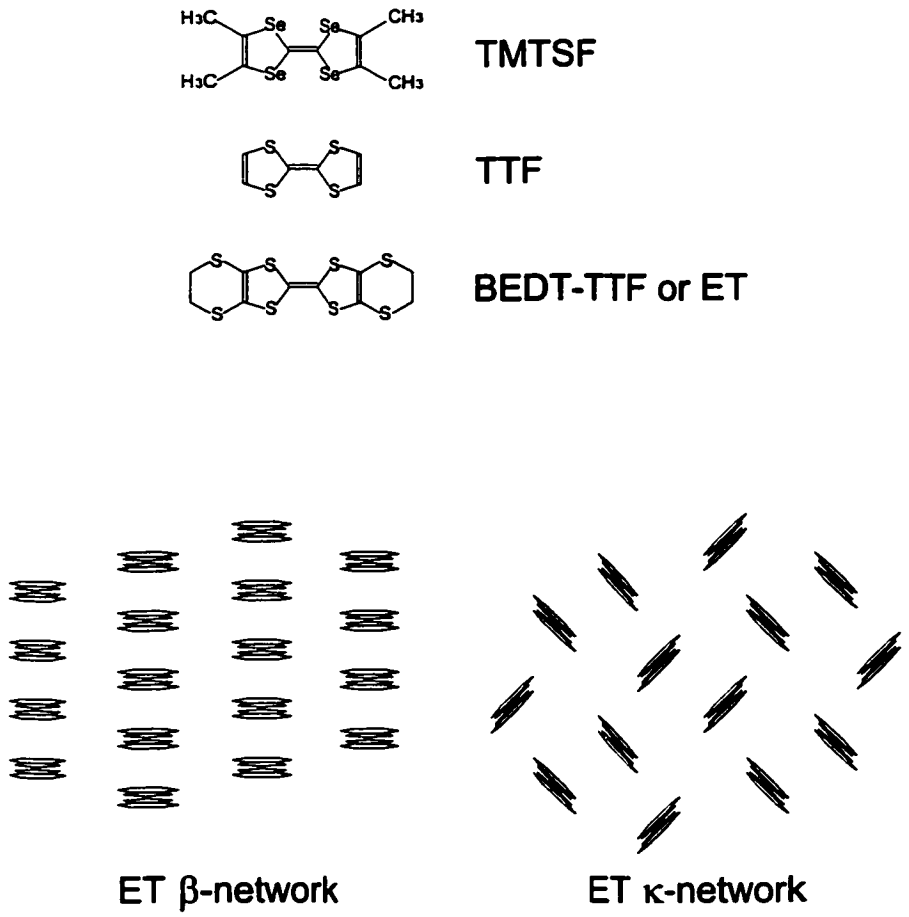

Figure 3.3: Components of organic conductors and superconductors. (After Williams *et al.*[68]) The upper part shows three of the large flat organic molecules which are common in organic conductors. The lower part shows two different stacking networks for the ET molecules that form conducting sheets in two-dimensional organic superconductors.

Much research has been done on κ-$(ET)_2Cu[N(CN)_2]Br$. DC resistivity and magnetoresistance studies show a strange peak in the resistivity near 100 K[71, 72, 73, 74, 75]. In addition, the transport below about 80 K is dependent on the cooling rate which is thought to be related to an order-disorder transition involving the terminal ethylene groups on the ET molecules in this temperature range[76, 77, 78, 79, 80]. In deuterated samples, this effect becomes more important and results in the coexistence of metallic and magnetically ordered insulating phases [81, 82, 83, 84]. Evidence for strong antiferromagnetic spin fluctuations is seen even in the undeuterated samples[85, 86, 87, 88]. Measurements of the Fermi surface have been inconsistent, perhaps due in part to a superstructural transition that occurs below 200 K[89, 90, 91, 92, 93]. There has even been evidence for a pseudogap in the density of states near the Fermi surface[77, 85, 86] and for line nodes in the superconducting gap[94, 95, 96, 97]. Two-dimensionality, line nodes in the gap, a pseudogap, and proximity to an antiferromagnetic phase, all make the material of great interest due to its potential similarity to the high-temperature superconductors[98].

Fig. 3.4 shows the crystal structure of κ-$(ET)_2Cu[N(CN)_2]Br$ emphasizing its quasi-two-dimensional nature. One important issue that will be addressed in this chapter is the nature of the interlayer transport: is it coherent giving rise to a three dimensional Fermi liquid at sufficiently low temperature, or does it remain incoherent to the lowest temperatures? This issue is well illustrated by two model systems, Sr_2RuO_4 and $Bi_2Sr_2CaCu_2O_{8+\delta}$ (Bi-2212).

Sr_2RuO_4 is isostructural with the cuprate superconductor $La_{2-x}Sr_xCuO_4$, and has a superconducting T_c of 1.5 K[99]. Although highly anisotropic, its interplane transport is considered to be coherent[100]. Bi-2212 is the most two-dimensional cuprate superconductor, and its interplane transport has been shown to be due to an incoherent

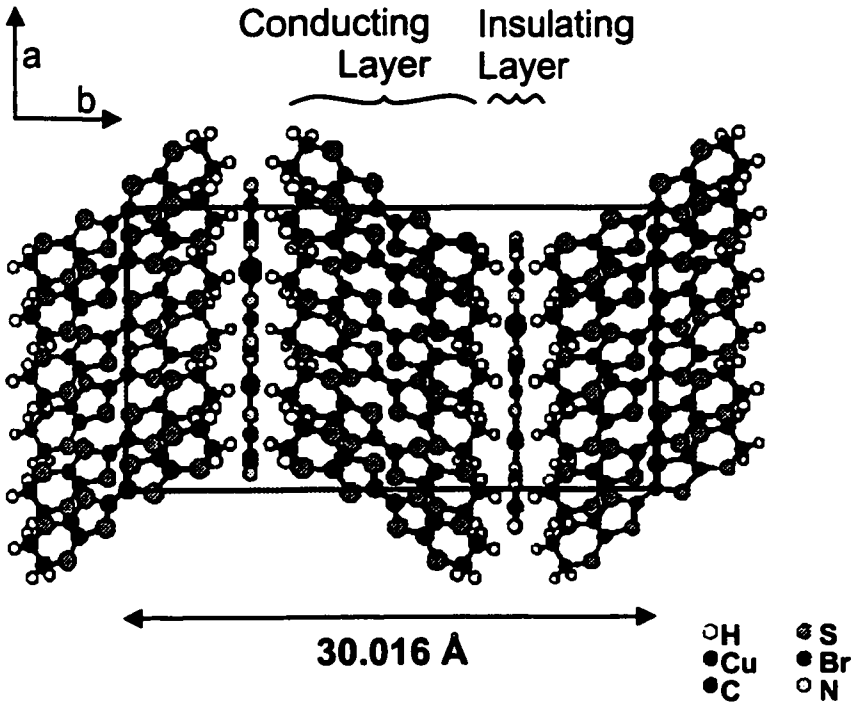

Figure 3.4: The crystal structure of κ-$(ET)_2Cu[N(CN)_2]Br$.
This picture emphasizes the two-dimensional nature of the material with conducting sheets of ET separated by insulating layers of anions.

tunneling mechanism[101]. The DC resistivity of optimally doped Bi-2212 in the conducting *ab*-planes is nearly linear with temperature up to several hundred Kelvin, while the interplane *c*-axis resistivity is four orders of magnitude higher and increases with decreasing temperature[101, 102]. In contrast Sr_2RuO_4 shows metallic resistivity both in the in-plane and interplane directions, although the resistivity in the interplane direction is two orders of magnitude higher than that of the in-plane direction and has a metallic temperature dependence only below 100 K[99].

The transport properties of κ-$(ET)_2Cu[N(CN)_2]Br$ are also highly anisotropic[72, 103]. Within the conducting *ac*-planes, the resistivity shows an unusual broad peak near 100 K, but has a clearly metallic behaviour at low temperature with resistivity decreasing with decreasing temperature. The interplane *b*-axis resistivity has qualitatively the same metallic temperature dependence as the in-plane resistivity, but is three orders of magnitude higher. At 15 K it is about 1 Ωcm, although the exact value depends somewhat on how quickly the sample is cooled[73]. This is six orders of magnitude higher than that of a good metal. As a result, in the interplane direction there is an apparent contradiction between the temperature dependence of the resistivity that suggests coherent transport, and the magnitude of the resistivity that suggests incoherent transport.

One criterion for evaluating the coherence of the interplane conductivity is the Ioffe-Regel-Mott minimum metallic conductivity. Modified for the open Fermi surfaces of these highly anisotropic systems[104] it gives a lower limit on conductivity which corresponds to a coherence length comparable to the size of a unit cell in the interlayer direction:

$$\sigma_{min} \approx \sqrt{\frac{\sigma_\perp}{\sigma_\parallel}} \frac{e^2}{2\pi^2\hbar} \frac{l_\perp}{l_{\parallel 1} l_{\parallel 2}} \tag{3.7}$$

where $\sigma_\perp$ and $l_\perp$ are the conductivity and lattice constant in the interplane direction and $\sigma_\parallel$, $l_{\parallel 1}$ and $l_{\parallel 2}$ are the conductivity and lattice constants in the planes. Table 3.1 lists these parameters for Sr_2RuO_4, Bi-2212 and κ-$(ET)_2Cu[N(CN)_2]Br$. The conductivity

Table 3.1: Ioffe-Regel-Mott minimum metallic conductivity for anisotropic systems. $l_{\parallel 1}$, $l_{\parallel 2}$ and $l_\perp$ are the two in-plane and one interplane room temperature lattice constants[99, 105, 70] in Å, T is temperature in Kelvin, and $\sigma_\parallel$, $\sigma_\perp$ and σ_{min} are the in-plane, interplane and minimum conductivities in $(\Omega cm)^{-1}$ at temperature T.

	$l_{\parallel 1}$	$l_{\parallel 2}$	$l_\perp$	T	$\sigma_\parallel$	$\sigma_\perp$	σ_{min}
Sr_2RuO_4	3.9	3.9	12.7	52	28600	37	37
$Bi_2Sr_2CaCu_2O_{8+\delta}$	3.8	3.8	30.9	85	25000	0.17	3.4
κ-$(ET)_2Cu[N(CN)_2]Br$	12.9	8.5	30.0	12.5	1000	1	11

anisotropy ratio should be evaluated at $\sigma_\perp = \sigma_{min}$. For Sr_2RuO_4 this gives coherent conductivity below 52 K which is indeed the temperature where the resistivity starts to deviate from the usual T^2 dependence. For Bi-2212 and κ-$(ET)_2Cu[N(CN)_2]Br$, however, $\sigma_{min} > \sigma_\perp$ even near T_c where the anisotropy is largest. This suggests that the low temperature interplane conductivity of Sr_2RuO_4 is coherent but becomes incoherent above 52 K due to thermal fluctuations, while both Bi-2212 and κ-$(ET)_2Cu[N(CN)_2]Br$ remain incoherent at all temperatures.

Optical conductivity provides another method of investigating the coherence of interplane transport since in a coherent system the optical conductivity σ_1 shows a Drude peak centered at zero frequency with a maximum corresponding to the DC conductivity σ_{DC} and a width equal to the scattering rate Γ of the free carriers.

$$\sigma_1(\omega) = \frac{\sigma_{DC}\Gamma^2}{\omega^2 + \Gamma^2} \tag{3.8}$$

The real part of the optical conductivity of Bi-2212 shows a Drude-like peak centered at zero frequency in the in-plane direction[106] but no such peak in the interplane direction[107]. Instead, the interplane conductivity consists entirely of phonon lines. In Sr_2RuO_4 the in-plane conductivity again shows a Drude-like peak, but in this case a weak Drude component can also be seen in the interlayer direction[100, 108]. These results are

in accord with the notion that the interplane conductivity of Bi-2212 is incoherent and that of Sr_2RuO_4 is coherent.

In the same way, the question of the coherence of the interplane transport in the ET-based organic superconductors can be addressed with measurements of low temperature, far-infrared optical conductivity. To date however, infrared studies have focused on the in-plane properties [109, 110, 111, 112, 113, 114, 115], and the few interplane measurements that have been made [116, 117, 118, 119] were at room temperature and above 600 cm^{-1}. Fig. 3.5 shows the in-plane reflectance and optical conductivity of κ-$(ET)_2Cu[N(CN)_2]Br$ measured by Eldridge *et al.*[109]. The lack of interplane data is due to the difficulty of growing crystals with large faces perpendicular to the conducting planes. Recently, however, high quality crystals of sufficient size for far-infrared interplane measurements have become available. The interplane reflectance measurements of κ-$(ET)_2Cu[N(CN)_2]Br$ presented in this thesis are the first such measurements on any ET based superconductor.

3.3 Interplane reflectance of κ-$(ET)_2Cu[N(CN)_2]Br$

The single crystals of κ-$(ET)_2Cu[N(CN)_2]Br$ were synthesized at Argonne National Laboratory by an electrocrystallization technique[70]. Typical crystal sizes were 1.5 × 1.5 × 1.5 mm^3 with faces as large as 1 mm^2 parallel to the interlayer b-axis. Polarized reflectance measurements between 40 and 8000 cm^{-1} were performed on these as-grown faces using three different detectors and the Michelson interferometer shown in Fig. 3.2. The grating spectrometer, shown in Fig. 3.1. with three additional detectors was used to make measurements at 300 K for the rest of the range up to 40,000 cm^{-1} (5 eV).

The reflectance of κ-$(ET)_2Cu[N(CN)_2]Br$ with the light polarized in the interplane direction is shown in Fig. 3.6 for four temperatures above the superconducting transition

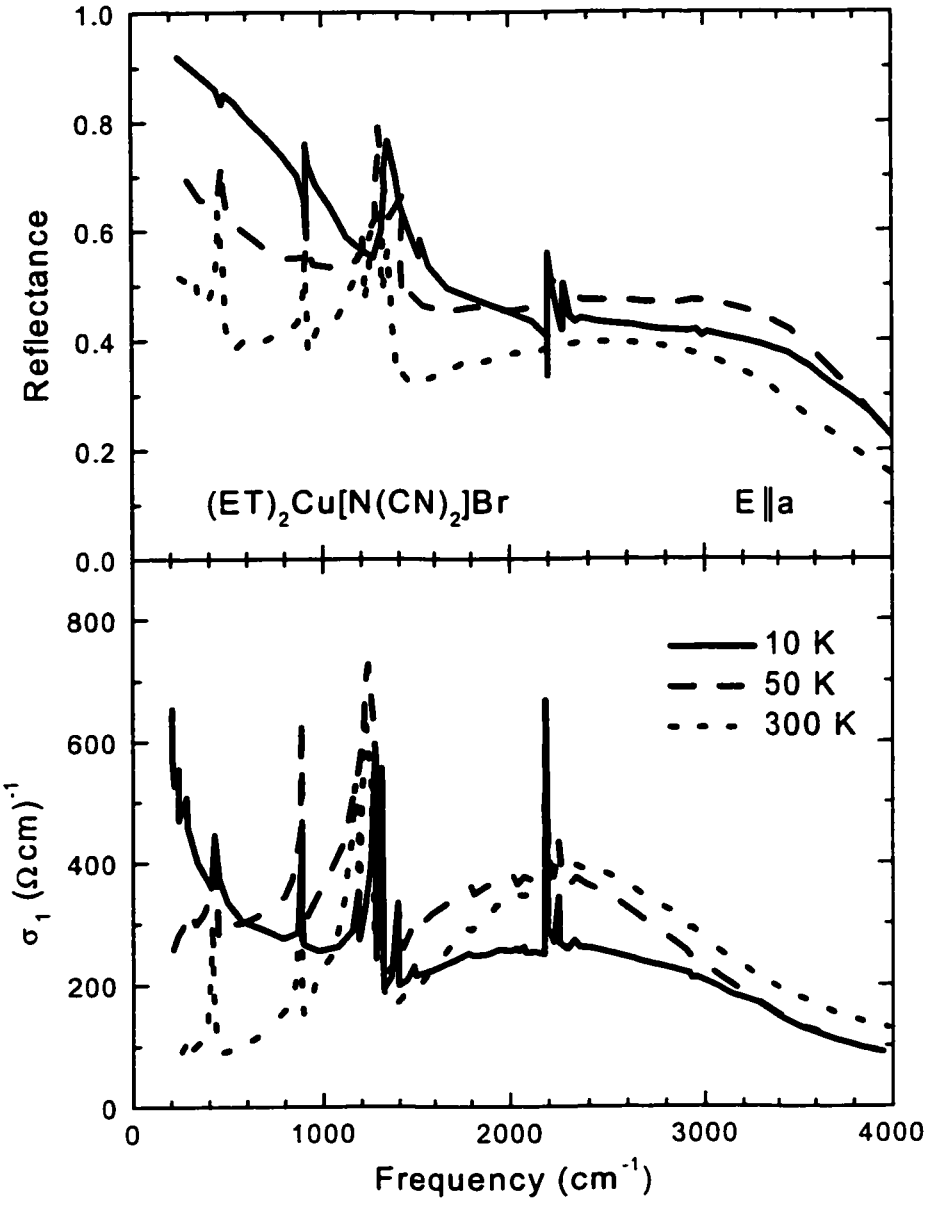

Figure 3.5: In-plane reflectance and optical conductivity of κ-(ET)$_2$Cu[N(CN)$_2$]Br The data measured by Eldridge *et al.*[109] show a Drude-like peak in the conductivity at low temperatures consistent with coherent transport.

temperature. The reflectance is approximately 0.15 over the entire range with several sharp phonon peaks at low frequencies and some broader interband-like features at higher frequencies. The resolution of the spectra is 2 cm^{-1} up to 200 cm^{-1}, 4 cm^{-1} up to 680 cm^{-1}, and 15 cm^{-1} up to 8000 cm^{-1}.

It should also be pointed out that there was some sample-to-sample variation of the interplane reflectance, particularly the temperature dependence of the background reflectance above 200 cm^{-1}. Fig. 3.7 is a comparison of the sample discussed above (upper panel) with a sample showing a strong temperature dependence (lower panel). The phonon lines below 200 cm^{-1} also appear to be stronger in this second sample although the optical conductivity should be calculated for a true comparison. Unfortunately the reflectance above 800 cm^{-1} was not successfully measured for this second sample, and the reason for the variation is not known. Complete data sets need to be collected on more samples to properly investigate this phenomenon. It is interesting to note that the feature has the appearance of a gap, and evidence for a pseudogap in κ-$(ET)_2Cu[N(CN)_2]Br$ at $T^* = 50$ K in ESR[77] and ^{13}C NMR[85, 86] measurements has been reported. This would give $2\Delta/k_BT^* = 5.7$ which is not far from the value 4.3 reported for the high-temperature cuprate superconductors[120].

The calculation of the optical conductivity requires extrapolation of the reflectance to all frequencies for the Kramers-Kronig analysis. The spectra were extrapolated to high frequencies using power law extrapolations: ω^{-1} above 5 eV and ω^{-4} above 62 eV. Below the lowest measured point at 25 cm^{-1} a Drude extrapolation is used, although an insulating extrapolation gives very similar results. The experimental uncertainty of the reflectance is estimated to be ± 0.005. Combined with uncertainties due to the extrapolations, this gives an uncertainty in the optical conductivity of $\pm 8\%$ between 200 and 2000 cm^{-1}. Outside this range the uncertainty rises, reaching $\pm 40\%$ at 25 and 5000 cm^{-1}.

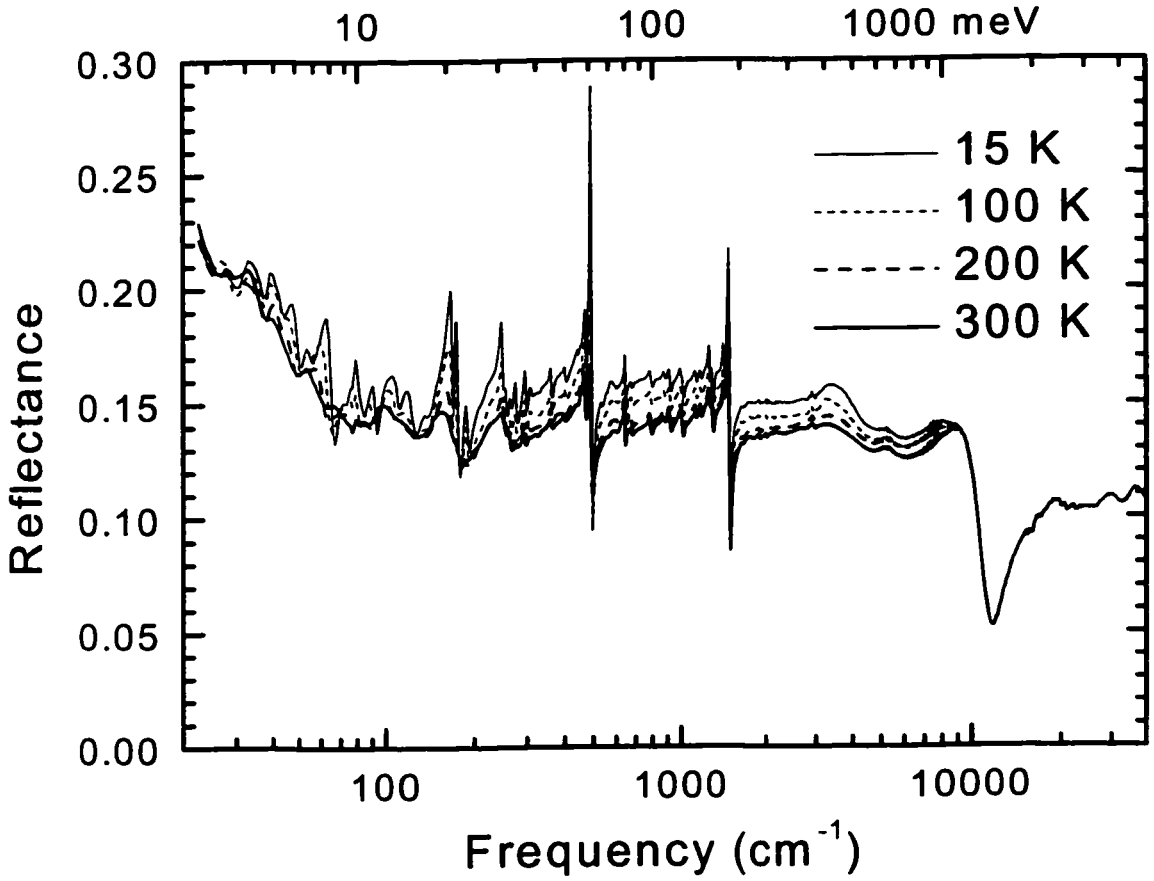

Figure 3.6: The interplane reflectance of κ-$(ET)_2Cu[N(CN)_2]Br$.

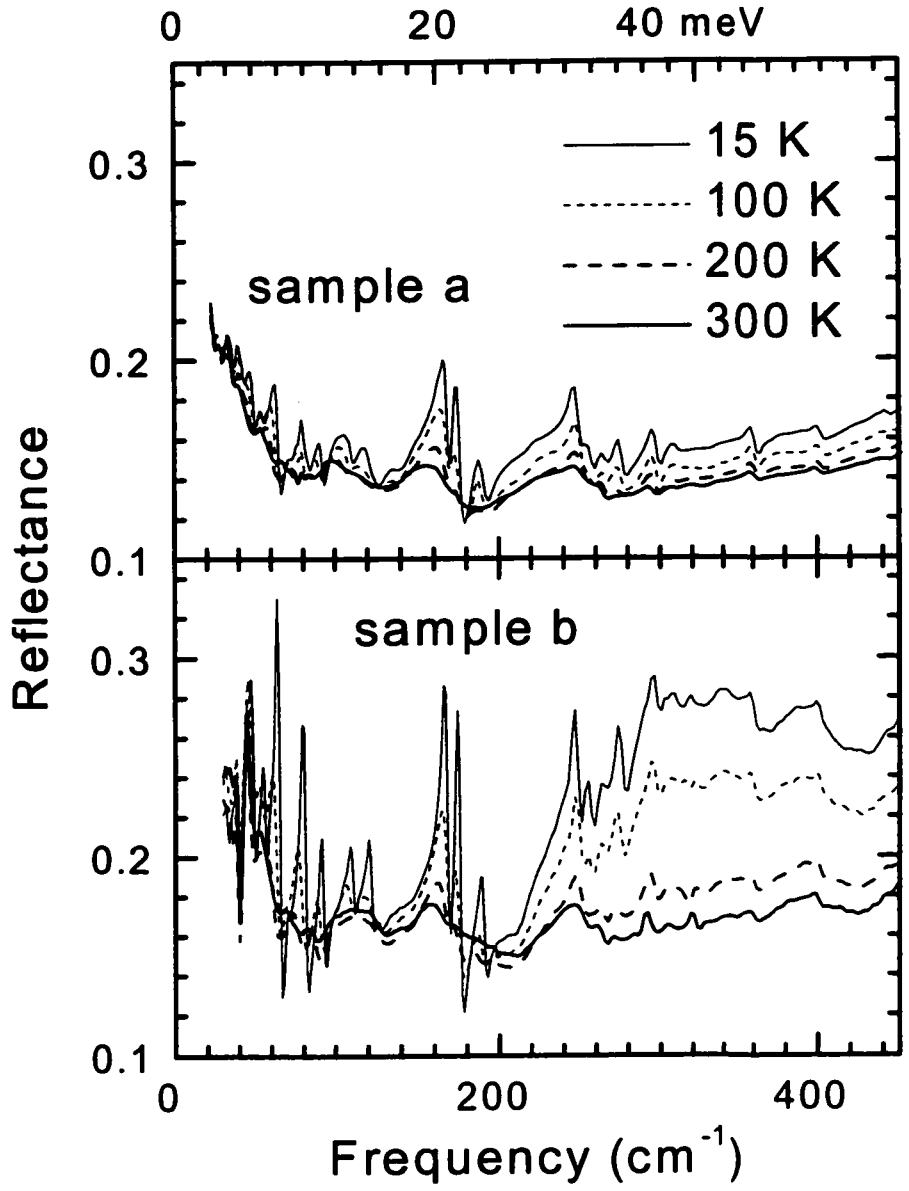

Figure 3.7: A comparison of the interplane reflectance of two crystals. The one in the lower panel shows stronger temperature dependence of the background above 200 cm^{-1}.

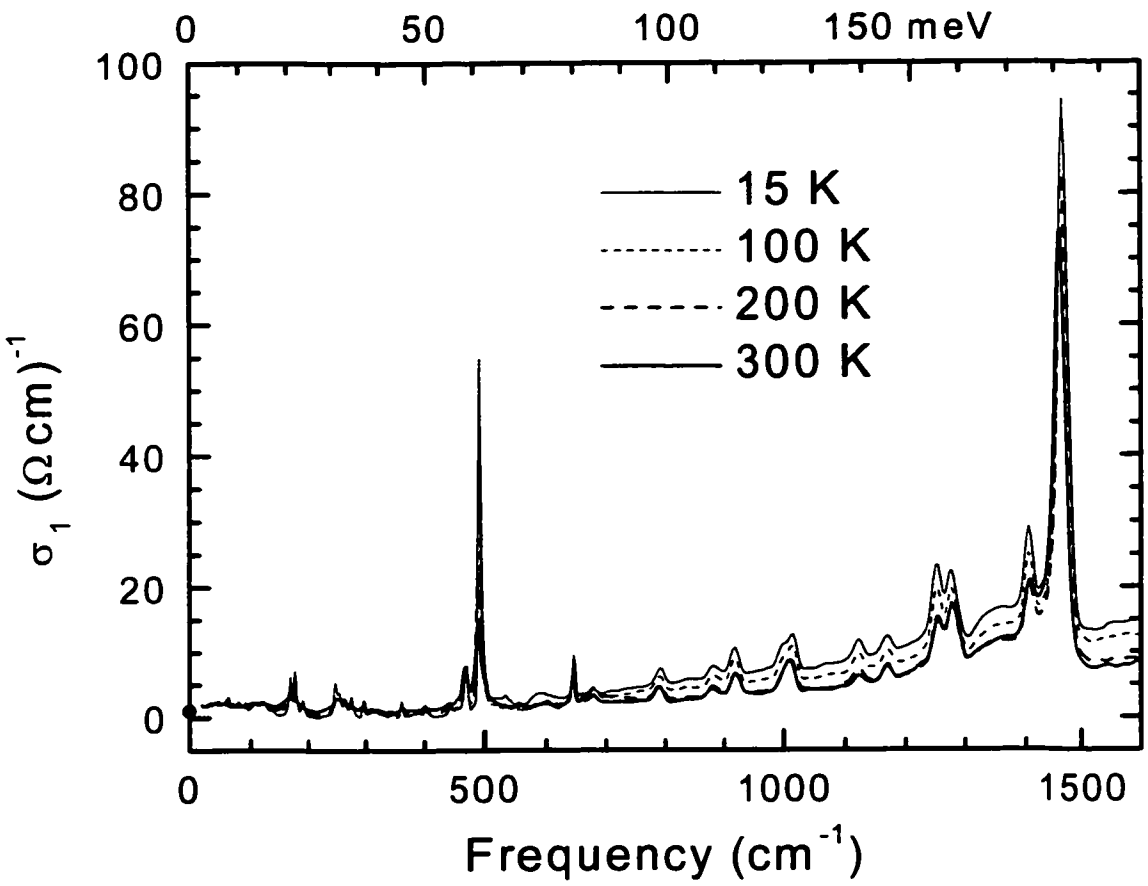

Figure 3.8: The interplane optical conductivity of κ-$(ET)_2Cu[N(CN)_2]Br$. The DC value is marked on the vertical axis at 1 $(\Omega cm)^{-1}$. There is no sign of the usual Drude peak that accompanies coherent conductivity.

The real part of the interplane optical conductivity is shown in Fig. 3.8. The value of the DC conductivity at 15 K[73] is shown at 1 $(\Omega\text{cm})^{-1}$ on the vertical axis. Clearly there is no sign of the usual Drude peak that accompanies coherent conductivity. Instead the conductivity is dominated by sharp phonon lines on a background due to interband-like features in the mid-infrared. This confirms that the interlayer conductivity in κ-(ET)$_2$Cu[N(CN)$_2$]Br is incoherent.

A fit to Lorentz oscillators, which will be discussed later, shows no sign of any free carrier component to the optical conductivity above 30 cm^{-1}. This is similar to what has been reported for Bi-2212[107]. An upper limit for the plasma frequency of a hypothetical Drude peak is estimated to be $\omega_p = 50$ cm^{-1} with a scattering rate $\Gamma = 40$ cm^{-1}. This in turn can be used with a simplified tight-binding model to estimate an upper limit for the interplane transfer integral using[115]:

$$\omega_p^2 = \frac{e^2}{\epsilon_0 \hbar^2} \sum_{BZ} f(E_{\mathbf{k}}) \frac{\partial^2 E}{\partial k_\mu^2} \tag{3.9}$$

where $f(E_{\mathbf{k}})$ is the Fermi-Dirac occupation number and the derivative is to be taken in the direction of the field. The form used for the tight-binding band is:

$$E_{\mathbf{k}} = -2t_a \cos(k_a d_a) - 2t_b \cos(k_b d_b) - 2t_c \cos(k_c d_c) \tag{3.10}$$

where d are the average ET molecular repeat distances and t are the average transfer integrals along the various directions. An open Fermi surface is assumed in the interplane direction[121] with $t_b \ll t_{ac}$ and the in-plane anisotropy is ignored to give

$$\omega_{pb}^2 \approx \frac{e^2}{\epsilon_0 \hbar^2} \frac{b^2/V_m}{\sqrt{\pi}\sin(\sqrt{\pi})} \frac{t_b^2}{t_{ac}} \tag{3.11}$$

where b is the interplane lattice constant and V_m the volume per ET molecule. This gives $t_b^2/t_{ac} \approx 10^{-7}$ eV.

Values for the in-plane transfer integral of $t_{ac} \approx 0.15$ eV have been reported for κ-$(ET)_2Cu[N(CN)_2]Br$[122, 123, 124], and similar values have been reported for other ET-based materials [115, 122, 125, 126, 124]. Using this value gives an interplane transfer integral of $t_b \approx 0.1$ meV. Of course, this analysis assumes a coherent component to the conductivity which seems unlikely given the earlier discussion of minimum metallic conductivity. Reported interplane transfer integrals for some other materials are 0.1 meV for Bi-2212[127] and 1.5 meV for Sr_2RuO_4[128, 129]. For the quasi-one-dimensional materials $(TMTSF)_2X$ the transfer integrals in the three directions are 250, 25 and $\approx$ 0.1 meV[130, 131]. The values for Bi-2212 and for the least conducting direction of $(TMTSF)_2X$ are for hopping integrals which describe incoherent transport.

If the interplane transport of κ-$(ET)_2Cu[N(CN)_2]Br$ is in fact incoherent, then why does the temperature dependence of the interplane DC conductivity show a clear metallic character and in fact follow rather accurately the in-plane conductivity although it is a factor of 1000 smaller? Since the interplane conductivity is below the minimum metallic limit it is highly likely that its metallic temperature dependence is due to some special process that makes it mirror the in-plane conductivity. There are several models that can do this[132, 133], and the focus here will be on a model originally proposed for Bi-2212 by Martin *et al.*[102], where the conducting planes are connected by a random network of shorts approximated as a regular array of links of resistance R_{lb} distance ξ apart along the conducting plane. Given the resistance R_{lac} along the plane between the shorts and the interplane distance d, the apparent interplane resistiyity is given by:

$$\rho_b = (R_{lb} + R_{lac}) \times \frac{(\xi/2)^2}{d} \tag{3.12}$$

Assuming $R_{lac} = \rho_{ac}/d$ the anisotropy is then:

$$\frac{\rho_b}{\rho_{ac}} = \left(1 + \frac{dR_{lb}}{\rho_{ac}}\right) \times \left(\frac{\xi}{2d}\right)^2 \tag{3.13}$$

Buravov's data[72] above 50 K are nearly temperature independent with $\rho_b/\rho_{ac} \approx 1000$, while below 50 K the anisotropy rises dramatically. Fig. 3.9 compares the interplane resistivity and anisotropy of Buravov *et al.* with a least squares fit using Eq. 3.13 assuming a temperature-independent R_{lb}. The fit, which reproduces both the temperature independence of the anisotropy at high temperatures and the dramatic increase in anisotropy at low temperatures, gives $R_{lb} = 138 \pm 9$ kΩ and $\xi = 802 \pm 7$ Å taking $d = 15$ Å. The model explains the rise of the anisotropy below 50 K as being due to the rapid drop of R_{lac} relative to the temperature-independent R_{lb}, whereas models where the proportionality between the in-plane and interplane resistivity is built in[132, 133] predict a constant anisotropy that is independent of temperature. The observed sample-to-sample variation shown in Fig. 3.7 is also consistent with a process controlled by defects.

The model of a meandering current will fail at high frequency. To estimate the characteristic maximum frequency the current path can be modeled as a transmission line of series resistors R_{lac} shunted to ground by capacitors C_s, where $C_s \approx 2\pi\xi$. The impedance of such a transmission line is:

$$Z = \frac{R_{lac}}{2}\left(1 + \sqrt{1 + \frac{4i}{\omega R_{lac} C_s}}\right) \tag{3.14}$$

Thus, above a frequency given by $\omega_0 = (R_{lac}C_s)^{-1}$ the capacitors short the AC current and the in-plane fields do not have time to build up. With the parameters determined above this gives $\omega_0 \approx 10\ \mathrm{cm}^{-1}$. A test of the model would be a reduction of the interplane conductivity from its DC value to a much lower value at this frequency. This is consistent with the observations of Dressel *et al.*[103] who find in the millimeter wave range (1-3 cm^{-1}) conductivities that agree with DC values. Unfortunately the strong phonon background discussed in the next paragraphs prevents an accurate determination of the value of the interplane electronic conductivity in the far-infrared range other than to give an upper limit of about 1 $(\Omega\mathrm{cm})^{-1}$.

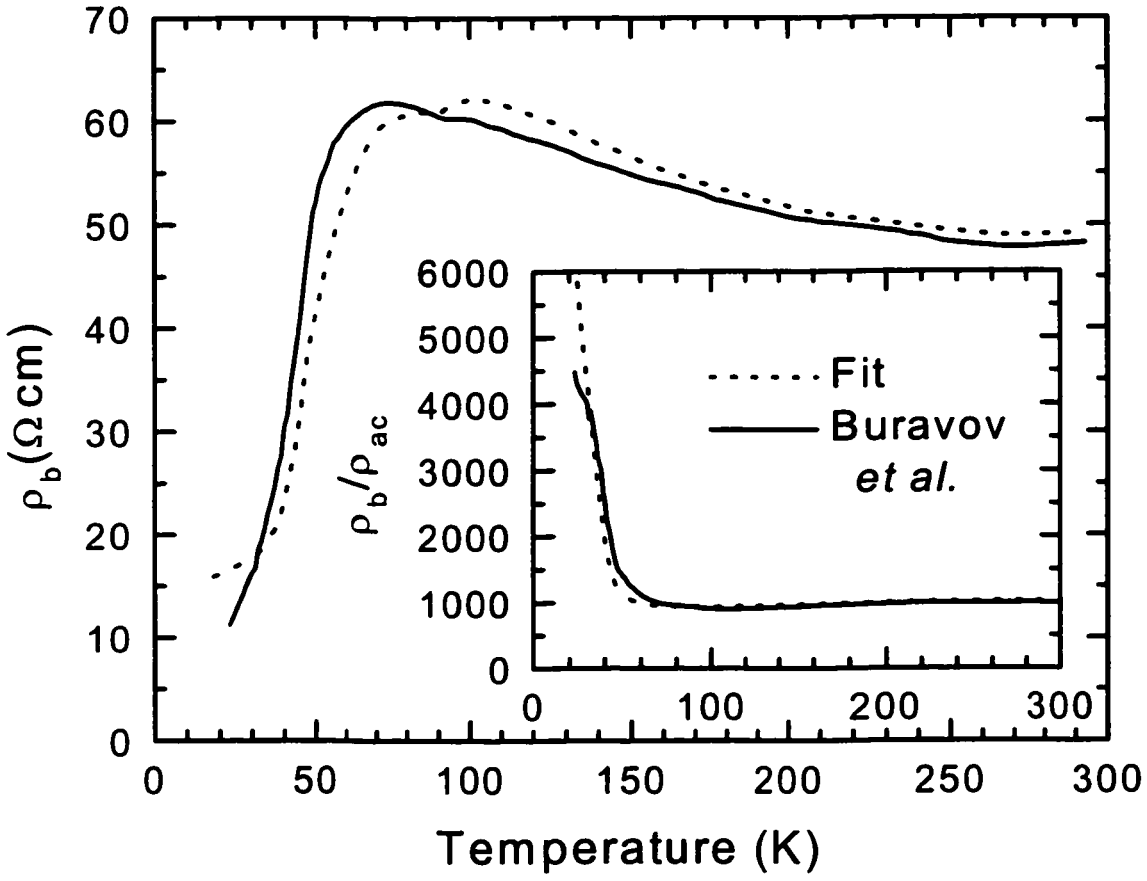

Figure 3.9: Interplane resistivity of κ-$(ET)_2Cu[N(CN)_2]Br$.
A comparison of the resistivity data of Buravov *et al.* [72] to a fit to the model of Martin *et al.* [102].

It was possible to fit the conductivity with a series of Lorentzian oscillators as discussed in Chapter 1 according to:

$$\sigma_1(\omega) = \frac{1}{4\pi}\sum_i \frac{\omega_{pi}^2\omega^2\Gamma_i}{(\omega_{0i}^2-\omega^2)^2+\omega^2\Gamma_i^2} \tag{3.15}$$

Fifty-one oscillators were used in the fit along with a weak Drude term to account for phonons below the measurement range and one strong oscillator at high frequency to provide the background tail of the mid-infrared features. It was necessary to add some asymmetry to the strongest oscillators at 492 and 1450 cm $^{-1}$ by introducing a phase angle θ into the expression for the complex conductivity so that the real component becomes a mixture of the symmetric σ_1 and the antisymmetric σ_2.

$$\sigma = (\sigma_1 + i\sigma_2)e^{i\theta} = (\sigma_1\cos\theta - \sigma_2\sin\theta) + i(\sigma_2\cos\theta + \sigma_1\sin\theta) \tag{3.16}$$

Values of θ were -0.24 and 0.14 for the lines at 492 and 1467 cm $^{-1}$ respectively, and zero for the rest of the lines.

Table 3.2 lists the frequency ω_0, plasma frequency ω_p and width Γ of the oscillators at all four temperatures. Most of the low frequency lines seem to be lattice modes as their frequencies increase with decreasing temperature[134]. Some of these lines were previously reported in a powder absorption experiment[134] and are marked with an asterisk. The rest of the lines are related to internal vibrations of the ET molecule, and these mode assignments were made by comparison with Eldridge *et al.* who assign the normal modes of the ET molecule[135] and relate these ET modes to observed lines in in-plane infrared and Raman spectra of κ-$(ET)_2Cu[N(CN)_2]Br$ [136, 137].

In general, infrared spectra are sensitive to asymmetric (ungerade) modes while Raman spectra are sensitive to symmetric (gerade) modes. Since the ET molecule consists of two mirrored halves joined by a single C=C bond (see Fig. 3.3), the infrared and Raman spectra of ET contain similar sets of lines[135]. Each vibration of atoms in one

Table 3.2: Lorentz oscillator parameters for κ-(ET)$_2$Cu[N(CN)$_2$]Br.
All values are in wavenumbers and were derived from fits to the real part of the interplane optical conductivity. Vertical lines associate one or more mode assignments with a set of oscillators. Asterisks indicate lines seen by Dressel *et al.*[134].

	15 K			100 K			200 K			300 K		
	ω_0	ω_p	Γ	ω_0	ω_p	Γ	ω_0	ω_p	Γ	ω_0	ω_p	Γ
	28.4	4.3	1.9	27.9	5.7	2.4	29.4	7.6	4.0	29.2	5.5	3.9
	34.4	15.3	5.8	34.5	15.7	6.4	34.6	17.1	7.2	34.0	17.2	7.2
	41.3	21.8	7.5	41.0	19.0	6.8	40.9	15.0	5.9	41.1	18.1	9.3
*	47.9	19.2	5.6	47.0	21.5	7.7	46.1	21.9	8.9	46.3	19.8	11.5
*	55.5	25.4	10.8	54.7	21.5	9.6	53.9	18.8	9.5	54.6	20.2	10.9
*	63.5	27.3	5.7	61.6	27.7	7.6	59.6	23.6	8.6	59.6	20.0	12.4
	72.0	12.4	4.4	71.4	19.1	8.4	69.9	27.2	14.4	69.5	28.5	15.4
	75.7	5.0	2.1	75.8	8.1	2.7	75.4	13.0	6.0	75.3	8.5	5.1
*	81.2	30.2	8.9	80.2	23.3	8.0	80.4	8.5	3.8	80.3	5.4	2.5
*	91.3	20.7	5.1	89.5	23.1	8.2	86.7	25.1	12.8	84.8	17.6	10.5
	103.0	21.8	9.4									
*	109.1	24.7	7.6	106.3	31.0	12.3	103.7	18.6	9.7			
*	121.2	39.8	13.3	118.9	30.4	15.8	113.4	35.3	27.8			
	136.5	14.7	7.1									
*	167.1	39.7	4.6	166.1	47.2	9.5	165.0	52.1	17.3			
*	175.3	42.9	4.7	175.1	37.7	7.5	175.9	35.1	14.9			
*	190.0	27.7	5.5	190.0	27.2	7.4	189.2	22.0	11.8			
*	248.7	39.0	5.3	249.7	23.7	4.9	251.4	30.6	8.9			
*	255.9	39.2	8.6	253.2	51.5	15.2						
$\nu_{53}(B_{2u})$	265.6	21.8	5.6	265.7	17.1	4.9	265.0	19.2	6.2			
$\nu_{36}(B_{1u})$*	276.3	32.0	5.8	275.8	29.3	6.8	275.5	22.0	9.8			
*	297.7	24.0	3.1	297.6	21.4	3.5	296.7	20.0	4.8	295.3	20.0	7.7
	311.1	22.1	8.0	311.7	16.6	7.0	310.2	10.5	5.1	308.5	14.0	8.6
	325.5	33.3	26.5	321.9	23.3	13.7	324.6	29.9	30.0	321.5	24.1	18.2
$\nu_{52}(B_{2u})$	360.9	27.6	5.2	361.6	20.2	3.8	361.6	22.5	6.5	361.6	16.4	5.9
$\nu_{35}(B_{1u})$	402.2	28.2	7.6	402.6	21.9	6.3	402.3	19.6	6.8	401.4	17.2	7.2
$\nu_{34}(B_{1u})$	471.3	57.8	6.4	471.1	58.6	7.5	470.3	63.9	9.6	469.4	65.4	11.4
	492.1	125.5	4.6	491.3	112.7	5.2	490.4	101.9	8.0	489.8	94.3	12.0
$\nu_{33}(B_{1u})$	595.3	91.8	54.2	598.9	68.7	48.0	596.9	63.0	54.0	595.3	33.2	25.1
$\nu_{51}(B_{2u})$	645.8	48.6	5.2	645.8	48.1	5.6	644.8	48.1	6.4	644.1	44.9	6.9
$\nu_{50}(B_{2u})$	676.5	68.5	40.7	677.8	68.8	33.6	676.7	63.8	28.5	677.5	37.4	19.0
$\nu_{32}(B_{1u})$	791.2	73.8	23.4	790.5	62.7	21.5	790.0	61.6	21.0	788.9	53.4	17.4
$\nu_{15}(A_u)$	837.7	105.0	61.2	837.4	85.8	56.2	836.1	63.4	49.3	839.2	38.2	34.6
$\nu_{49}(B_{2u})$	881.9	92.2	34.5	881.9	83.4	31.9	881.0	69.1	28.3	879.4	63.9	29.5
$\nu_{48}(B_{2u})$	917.2	92.1	22.0	917.8	85.0	20.4	919.1	75.9	20.0	919.0	73.8	20.5
$\nu_{31}(B_{1u})$												
$\nu_{30}(B_{1u})$	998.7	93.7	28.3	999.6	83.4	27.3	1001.7	78.0	27.5	1002.8	78.3	24.2
$\nu_{47}(B_{2u})$	1015.4	78.6	17.8	1015.0	76.4	17.6	1013.7	61.1	16.0	1012.8	51.3	13.1
$\nu_{14}(A_u)$	1121.8	103.9	31.9	1122.2	97.5	31.8	1122.2	78.1	27.6	1123.2	83.1	38.5
$\nu_{67}(B_{3u})$	1167.3	113.3	36.3	1168.9	104.9	36.3	1168.6	78.6	27.2	1168.3	76.1	25.5
$\nu_{46}(B_{2u})$	1251.3	132.3	21.1	1251.7	119.3	20.3	1252.5	100.9	19.8	1253.0	98.0	21.2
$\nu_{29}(B_{1u})$	1277.3	138.2	24.6	1278.2	131.3	24.1	1278.9	130.1	24.6	1279.4	131.1	26.2
$\nu_{28}(B_{1u})$	1404.4	134.7	19.2	1405.4	133.9	21.2	1406.1	129.4	24.3	1406.9	123.0	24.6
$\nu_{45}(B_{2u})$												
$\nu_{27}(B_{1u})$	1467.7	343.9	22.9	1467.3	325.0	19.9	1465.5	316.9	20.8	1462.5	321.1	24.0
$\nu_{26}(B_{1u})$	2921.0	62.7	17.8	2920.4	60.9	18.1	2922.4	55.0	18.7	2920.4	52.0	20.2
	2938.6	53.7	24.0	2937.4	49.4	25.0	2938.9	48.7	24.4	2939.6	48.6	26.0
$\nu_{44}(B_{2u})$	2960.5	52.5	20.2	2960.8	58.0	24.9	2963.1	54.5	23.2	2962.8	51.4	20.2
$\nu_{66}(B_{3u})$	2982.4	44.5	13.6	2983.2	46.1	15.6	2982.0	38.6	18.1	2981.3	48.3	24.9

half of the molecule can be in phase or out of phase with an identical vibration in the other half producing symmetric/asymmetric pairs of modes. Since the two halves are nearly independent, the members of each mode pair have nearly the same energy. This argument does not apply to modes involving the central C=C bond.

As for ET, the in-plane infrared and Raman spectra of κ-$(ET)_2Cu[N(CN)_2]Br$ also have similar sets of lines, however in this case both sets of lines are ascribed to the symmetric modes of ET[136]. The reason the symmetric ET modes are infrared-active in κ-$(ET)_2Cu[N(CN)_2]Br$ is the arrangement of ET molecules into dimers so that the members of a dimer can vibrate out of phase transferring charge back and forth and producing the dipole moment required for infrared activity. The Raman line positions in κ-$(ET)_2Cu[N(CN)_2]Br$ are shifted from the ET line positions due to the charge on the ET molecules, and the infrared line positions are further shifted by their coupling to the charge transfer between members of a dimer[136]. To assist them in their mode assignments, Eldridge *et al.* also cause further shifts using several isotopic substitutions.

The lines in the interplane infrared spectra can be assigned to the asymmetric modes of the ET molecule. The mechanism that makes the symmetric modes infrared-active in the in-plane measurements does not apply to the interplane measurements since the electric vector of the light is perpendicular to the direction of charge transfer between members of a dimer. Fig. 3.10 shows a comparison of σ_1 from the current study to the ET powder absorption spectrum of Eldridge *et al.*[135]. For the most part, the mode assignments in Table 3.2 are based on this comparison since measurements on many isotopic analogs were not made. A partial reflectance spectrum, however, was measured for a κ-$(^{13}C(2)\text{-}ET)_2Cu[N(CN)_2]Br$ crystal in which the two central carbon atoms have been substituted with ^{13}C. Fig. 3.11 shows the 23 cm^{-1} shift of a line at 791.2 cm^{-1} confirming its identity as the $\nu_{32}(B_{1u})$ mode[135]. Since this mode involves the central C=C bond, its symmetric counterpart is at a very different frequency and is

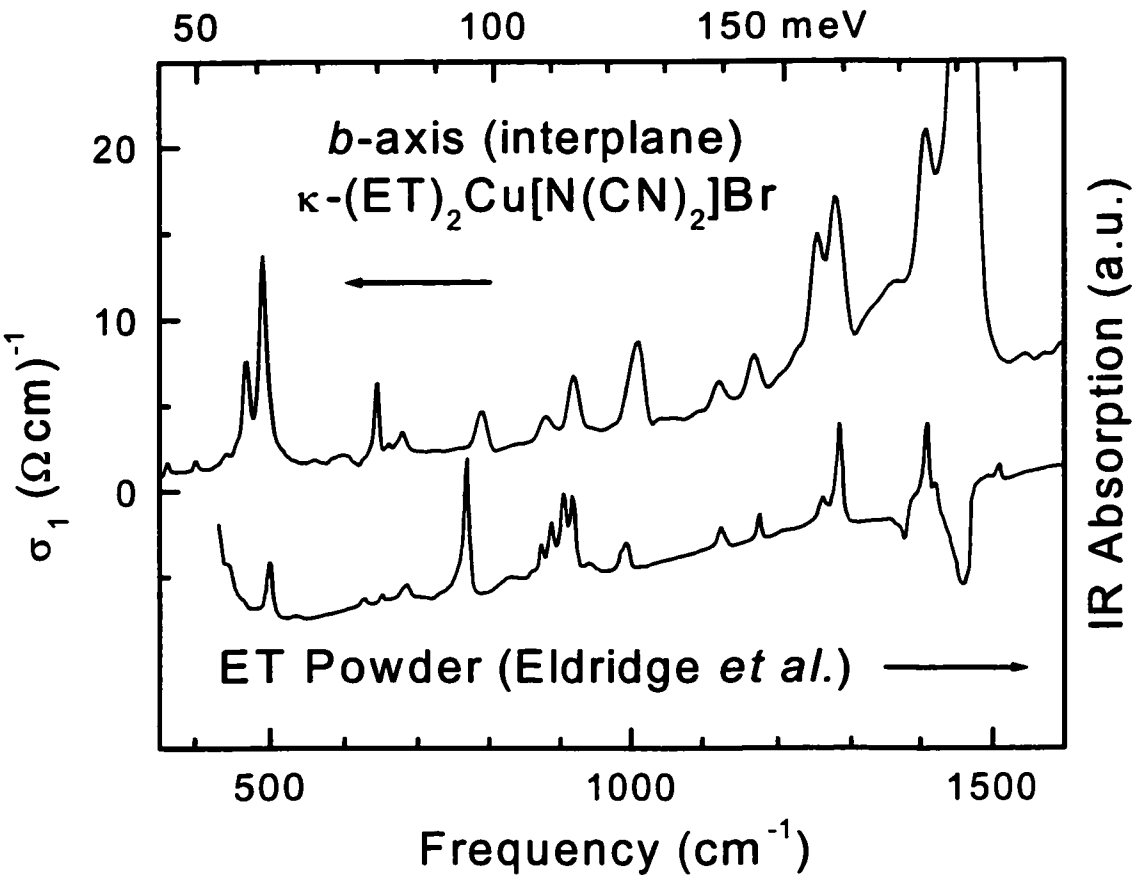

Figure 3.10: Powder absorption spectrum of ET.
A comparison at 300 K of the real part of the interlayer optical conductivity of κ-(ET)$_2$Cu[N(CN)$_2$]Br with the powder absorption spectra of ET measured by Eldridge *et al.*[135].

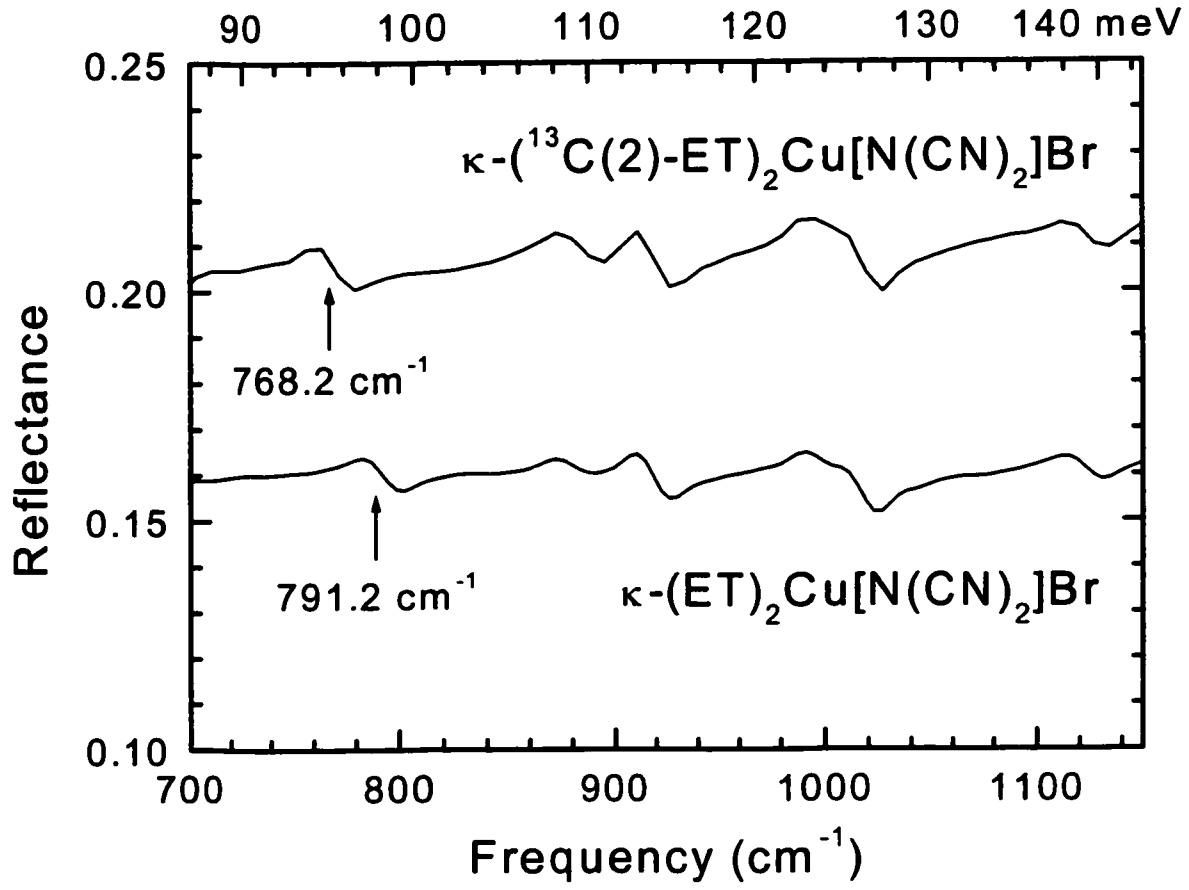

Figure 3.11: The effect of ^{13}C substitution.
A comparison at 15 K of the interlayer reflectance of κ-$(ET)_2Cu[N(CN)_2]Br$ with that of a sample in which the two central carbon atoms have been substituted with ^{13}C.

seen in the in-plane infrared and Raman spectra near 450 cm^{-1} while no line is seen near 791 cm^{-1}[136].

In general, all of the lines become narrower as temperature decreases as expected, however the plasma frequencies, or line strengths, also increase significantly in some cases. In particular, the line at 81 cm^{-1}, which is quite strong at 15 K, has nearly disappeared above 200 K. An increase in line strength with decreasing temperature in organic conductors has generally been interpreted as a signature of charge-density-wave fluctuations[138, 139]. However, temperature-dependent phonon intensities have also been associated with spin-density-wave transitions[140].

In summary the interplane reflectance of the quasi-two-dimensional organic superconductor κ-$(ET)_2Cu[N(CN)_2]Br$ has been measured and the optical conductivity calculated using Kramers-Kronig relations. Strong evidence of incoherent transport has been found as has been reported for the high-temperature superconductors. An upper limit for the free carrier plasma frequency was estimated to be 50 cm^{-1} from which an upper limit on the interplane transfer integral of 0.1 meV was derived. A defect model has been used to explain the crossover from a temperature independent resistivity anisotropy at high temperatures to a rapidly increasing anisotropy at low temperatures. Also, the phonon lines in the conductivity have been fit to a series of Lorentzian oscillators and assigned to the asymmetric modes of the ET molecule.

Chapter 4

$HgBa_2Ca_2Cu_3O_{8+\delta}$

Since the discovery of the first high-temperature superconductor in 1986, these compounds have been among the most studied in condensed matter research. This is due to their potentially important technological applications as well as to the fact that the mechanism behind their superconductivity remains poorly understood even today. They are different from the well-understood conventional superconductors in that they have a quasi-two-dimensional nature, anisotropic gap symmetry, anomalous normal state properties, and of course, remarkably high transition temperatures. The compound with the highest transition temperature is $HgBa_2Ca_2Cu_3O_{8+\delta}$ (Hg-1223). It has been studied using many experimental techniques, but crystals large enough for far-infrared measurements have not been available until recently[141]. The results reported here are in-plane far-infrared measurements on single-crystal Hg-1223 in which a feature called the pseudogap is seen to be larger than that seen in any other material[142].

Section 4.1 is a general overview of high-temperature superconductors. Section 4.2 focuses on an unusual normal state property called the pseudogap and describes its observation using a variety of experimental techniques, particularly in-plane infrared spectroscopy. Section 4.3 contains the far-infrared measurements of Hg-1223 and discusses the implications of these measurements to our understanding of the relationship between transition temperature and pseudogap size.

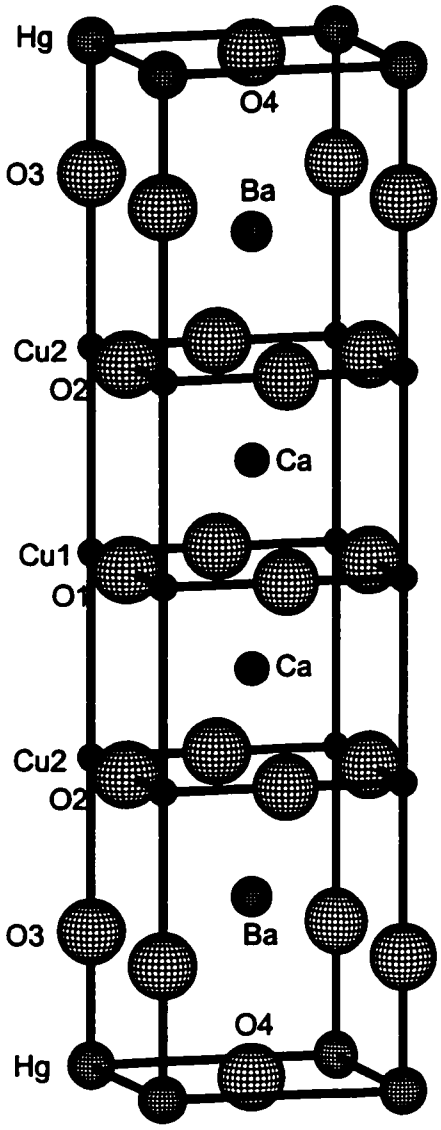

Figure 4.1: Crystal structure of $HgBa_2Ca_2Cu_3O_{8+\delta}$.
(After Colson *et al.*[141]) Note the CuO_2 planes found in all high-temperature superconductors. In this material there are three per unit cell. The dopant oxygens go to the O4 site, and the Hg site typically has about 16% Cu substitution[141].

4.1 High-temperature superconductors

Like the ET-based organic superconductors discussed in Chapter 3, the high-temperature superconductors are two-dimensional in nature. They have a perovskite-based structure with conducting CuO_2 planes separated by layers of anions as depicted in Fig. 4.1 for Hg-1223[141]. The anion layers both insulate the CuO_2 planes from each other and cause them to be conducting by providing charge carriers.

This can be understood as follows. In the undoped material, by neglecting covalency and considering the oxidation states of the individual atoms, one expects one hole per copper giving a half-filled band. This would be a conductor except that strong correlation effects split the band giving an unusual insulating state. Because of the complexity of the chemical structure, it is possible to make slight variations to the stoichiometry without changing the fundamental two-dimensional order. By substituting or adding dopant atoms to the insulating layers, extra holes are added to the CuO_2 planes creating a poor metal similar to a doped semiconductor. It is this poor metal which, at low temperatures, undergoes a superconducting phase transition. In the case of $HgBa_2Ca_2Cu_3O_{8+\delta}$ this doping process involves adding oxygen to increase δ form zero which gives an insulator to a value near 0.2 which gives a superconductor.

Fig. 4.2 shows a generic phase diagram for high-temperature superconductors. At zero doping they are insulators that undergo an atiferromagnetic phase transition at low temperatures due to the ordering of the copper $S = \frac{1}{2}$ spins. At finite doping they are poor metals that, for a certain range of dopings, become superconductors at low temperatures. The doping that corresponds to the highest T_c is referred to as optimal doping, while doping below and above this value is referred to as underdoping and overdoping respectively. Table 4.1 is a list of some high-temperature superconductors along with their T_c at optimal doping. Hg-1223 has the highest at $T_c = 135$ K, but most of the

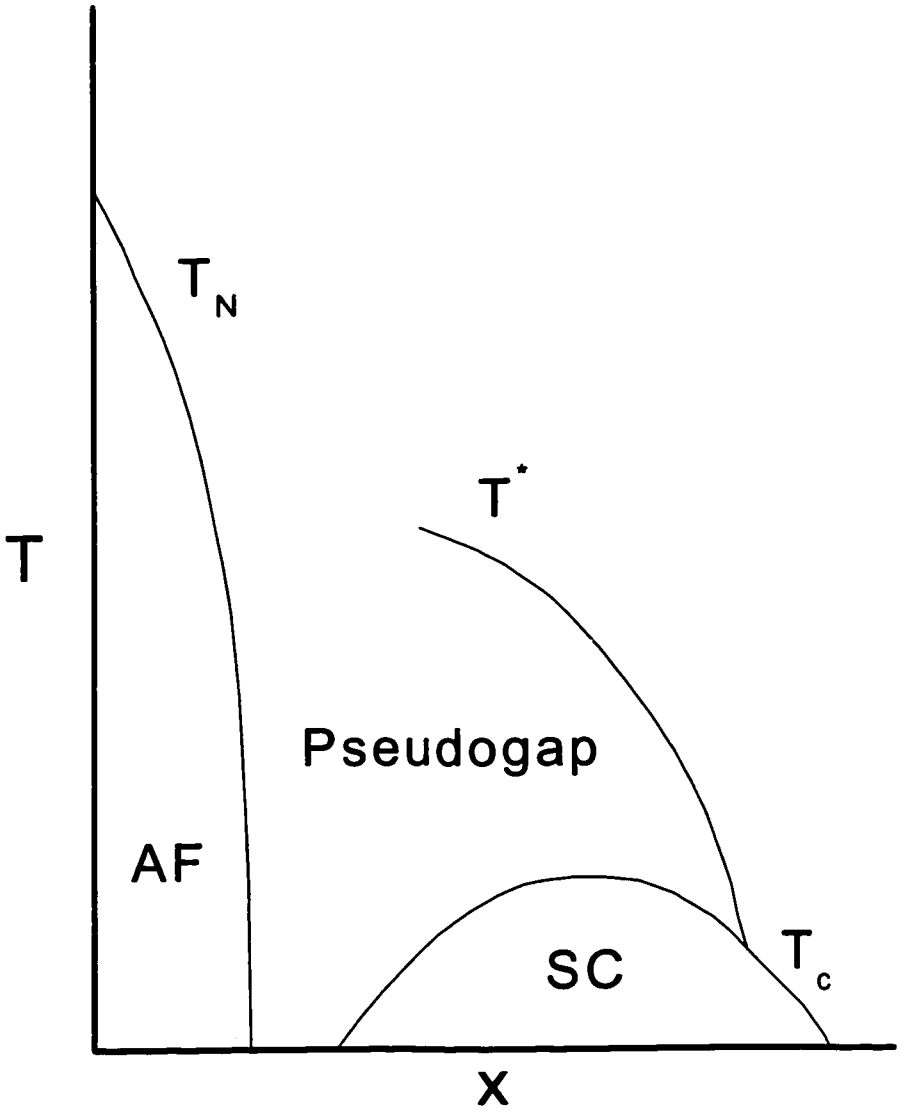

Figure 4.2: Phase diagram for high-temperature superconductors.

Table 4.1: Superconducting transition temperatures of some high-temperature superconductors.

Compound	Abbreviation	CuO_2 Layers	T_c (K)
$La_{2-x}Ba_xCuO_4$	LBCO	1	27
$La_{2-x}Sr_xCuO_4$	LSCO	1	37
$YBa_2Cu_4O_8$	Y-124	2	80
$YBa_2Cu_3O_{7-\delta}$	Y-123	2	92
$Bi_2Sr_2CuO_{6+\delta}$	Bi-2201	1	10
$Bi_2Sr_2CaCu_2O_{8+\delta}$	Bi-2212	2	85
$Bi_2Sr_2Ca_2Cu_3O_{10+\delta}$	Bi-2223	3	110
$Tl_2Ba_2CuO_{6+\delta}$	Tl-2201	1	95
$Tl_2Ba_2CaCu_2O_{8+\delta}$	Tl-2212	2	118
$Tl_2Ba_2Ca_2Cu_3O_{10+\delta}$	Tl-2223	3	125
$HgBa_2CuO_{4+\delta}$	Hg-1201	1	97
$HgBa_2CaCu_2O_{6+\delta}$	Hg-1212	2	128
$HgBa_2Ca_2Cu_3O_{8+\delta}$	Hg-1223	3	135

materials that have been studied in detail with infrared spectroscopy have $T_c \approx 90$ K.

Like the ET-based superconductors discussed in Chapter 3, the high-temperature superconductors differ from the conventional superconductors discussed in Chapter 1 in many ways. In addition to their high transition temperature and two-dimensional nature, it is also clear that the mechanism by which electrons form Cooper pairs is different from the phonon-mediated process of the conventional superconductors. This can be demonstrated using the isotope effect which is the dependence of transition temperature on the mass of atoms in the crystal. A crystal grown with one type of atom replaced by one of its isotopes will have the same crystal structure, but the energy of lattice vibrations, or phonons, will be changed due to the change in mass. In conventional superconductors, where the phonons are involved in the formation of Cooper pairs, the isotope effect is large. In high-temperature superconductors, however, the effect is significantly smaller suggesting a different pairing mechanism.

It is clear, however, that Cooper pairs do form in the high-temperature superconductors and that a superconducting energy gap is involved. Here too there is a difference though. In conventional superconductors the gap is of approximately the same size along all crystallographic directions, but in the cuprates the gap actually goes to zero in certain directions[143]. In fact, the phase of the order parameter changes sign on either side of these zeros giving a d-wave symmetry as opposed to the s-wave symmetry of the conventional materials.

Even in the normal state, at temperatures above the superconducting transition temperature, there are differences. The DC resistivity of optimally doped cuprate superconductors is nearly linear up to temperatures of several hundred Kelvin[101, 102]. This is difficult to understand since it is not seen in other materials and would suggest a coherence length significantly smaller than the lattice constant. In underdoped cuprates, the resistivity deviates from linearity above a temperature T^*, but this seems to be a

signature of another unusual property called the pseudogap.

4.2 The pseudogap

The pseudogap is a suppression of scattering rate below a certain energy and temperature and bears some resemblance to the superconducting gap except that it exists at temperatures significantly higher than the superconducting transition temperature. It has been seen using many experimental techniques[144] including DC resistivity, Hall effect, magnetic susceptibility, specific heat, tunneling experiments, angle resolved photoemission spectroscopy (ARPES), NMR, raman spectroscopy and infrared spectroscopy. ARPES experiments suggest that the pseudogap has the same d-wave symmetry as the superconducting gap. The lack of discontinuity at T_c of any gap properties makes it unclear whether the pseudogap and superconducting gap are in fact distinct entities. however. specific heat experiments[145] have been interpreted to suggest that the gaps do have separate origins. It is hoped that an understanding of the pseudogap will lead to an understanding of high-temperature superconductivity.

The temperature of the onset of the pseudogap T^* can be measured with many techniques. and is generally found to be higher than T_c only in the underdoped state. In DC resistivity measurements T^* is the temperature above which the resistivity has a linear dependence on temperature. It is also the temperature above which the Hall coefficient is nearly temperature independent and below which the magnetic susceptibility decreases sharply[146].

Other techniques measure not only T^* but also the size of the pseudogap. This is the energy below which there is a partial gap in the density of states causing a decrease in scattering. Tunneling spectroscopy, which measures the density of states directly. detects the pseudogap as a decreased density of states at low energies that persists up

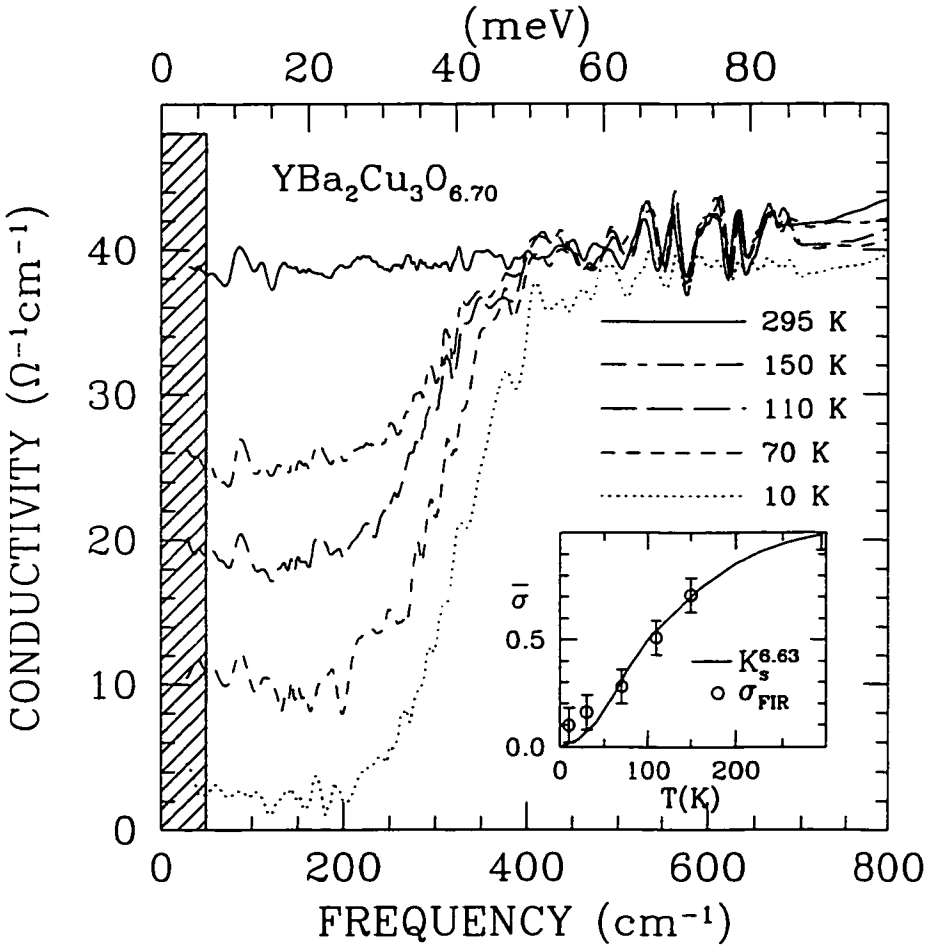

Figure 4.3: c-axis conductivity of YBCO.
(After Homes *et al.*[147]) The pseudogap can be seen below 400 cm^{-1}. The inset compares the low frequency values to the NMR Knight shift normalized at 300 K.

to $T^* > T_c$. ARPES measurements also determine the size of the pseudogap with the additional advantage of being able to determine its dependence on direction within the crystal providing evidence for its d-wave nature. A disadvantage of ARPES is its strong dependence on surface quality which limits it to measurements on materials that can be readily cleaved. Raman spectroscopy can also provide some indication of the gap symmetry as well as a measure of gap size. Infrared spectroscopy gives no indication of gap symmetry, but it does have advantages over the other techniques. It is not particularly surface sensitive and can be performed on relatively small samples, making it possible to compare results from several different materials.

The pseudogap has been seen in the interplane optical conductivity of various high-temperature superconductors. Fig 4.3 shows this for Y-123 after phonon features have been subtracted out[147]. A clear suppression of the conductivity can be seen below 400 cm^{-1} that is different from the signature of the superconducting gap seen in the conductivity spectra of conventional superconductors. The size of a superconducting gap should be maximum at zero temperature and approach zero at T_c, while the size of the pseudogap in Fig 4.3 is 400 cm^{-1} at all temperatures. Instead, it is the depth of the pseudogap that seems to approach zero at high temperatures, but the temperature T^* at which it reaches zero is well above the superconducting transition temperature T_c and correlates well with values of T^* from other experiments.

A signature of the pseudogap can also be seen in the in-plane infrared spectra. Here, however, the pseudogap shows up in the frequency-dependent scattering rate which can be extracted from the conductivity. The simple Drude model (Eq. 1.9) predicts that the real part of the optical conductivity due to free carriers should go as ω^{-2} for $\omega \gg \Gamma$:

$$\sigma_1 = \frac{\omega_p^2}{4\pi} \frac{\Gamma}{\Gamma^2 + \omega^2} \tag{4.1}$$

In high-temperature superconductors, the frequency dependence is closer to $\sigma_1 \propto \omega^{-1}$.

This can be described in terms of a two-component model in which the conductivity is the sum of a free carrier Drude term peaked at zero frequency and terms due to polarizable bound-state electrons peaked in the mid-infrared. The ω^{-1} arises then from the overlap. An alternate description is a one-component model in which the low frequency conductivity is described by a Drude term in which the scattering rate, which is frequency independent in the simple Drude model, is allowed to vary with frequency, $\Gamma = 1/\tau(\omega)$. This is referred to as the Extended Drude Model which gives for the conductivity:

$$\sigma = \frac{\omega_p^2}{4\pi} \frac{1}{1/\tau(\omega) - i\omega[1 + \lambda(\omega)]} \tag{4.2}$$

where $\lambda(\omega)$ is the mass enhancement factor. Thus,

$$1/\tau(\omega) = \frac{\omega_p^2}{4\pi} Re\left(\frac{1}{\sigma(\omega)}\right), \qquad 1 + \lambda(\omega) = -\frac{\omega_p^2}{4\pi\omega} Im\left(\frac{1}{\sigma(\omega)}\right) \tag{4.3}$$

Figs. 4.4, 4.5 and 4.6 show the scattering rates and mass enhancement factors for several high-temperature superconductors as reported by Puchkov *et al.*[148] for underdoped, optimally doped and overdoped samples respectively. The scattering rates are generally linear with frequency with an intercept near $1/\tau$=1000 cm^{-1} except for a suppression of scattering below 700 cm^{-1} at low temperatures. In the underdoped state, and occasionally in the optimally doped state, this suppression persists even above T_c indicating a pseudogap. The scattering rate above the pseudogap is nearly temperature independent except in the overdoped state where it seems to be proportional to temperature.

There is some disagreement between infrared measurements and other techniques as to the doping dependence of the pseudogap. According to these techniques, the size of the gaps in the one- and two-layer materials are of the order of $9.5k_BT_c$ at optimal doping and essentially independent of temperature, but as T_c is reduced below optimal doping the gaps increase in size[145, 149, 150]. This is not true in the *ab*-plane infrared response.

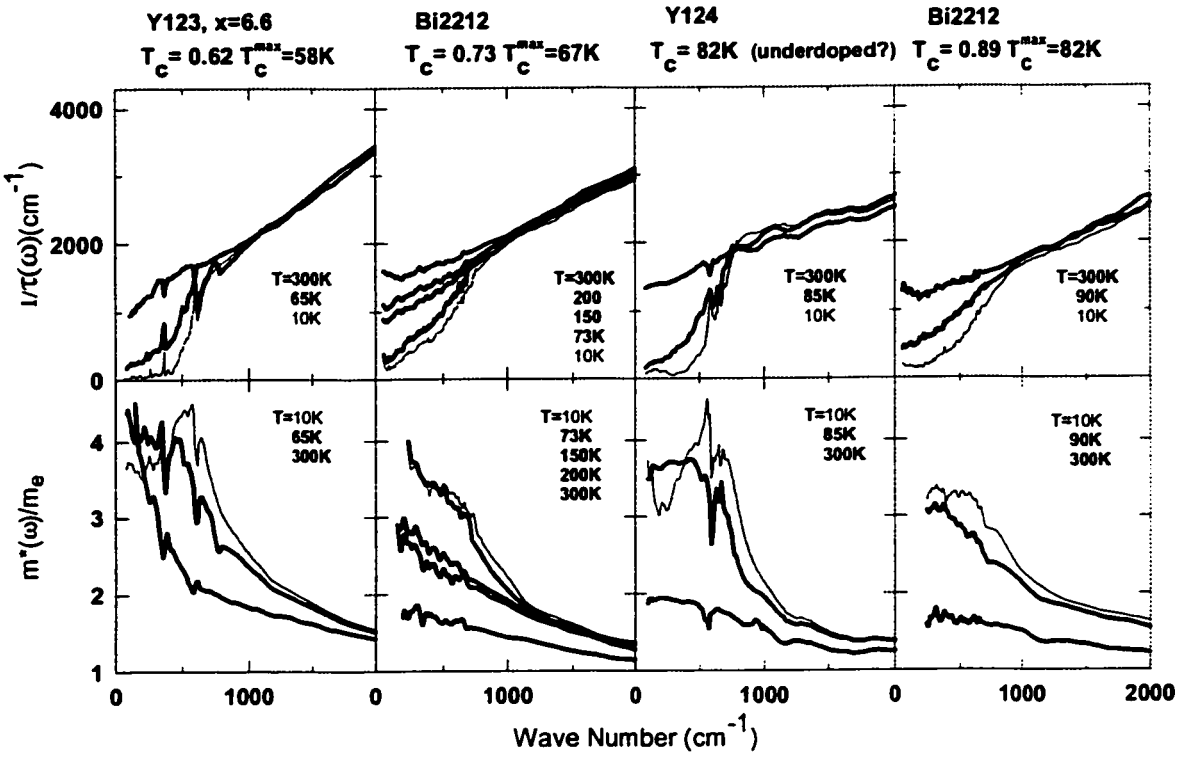

Figure 4.4: Scattering rate and effective mass for underdoped cuprates. (After Puchkov *et al.*[148]) The suppression below 700 cm^{-1} of the scattering rate in the top row and enhancement of the effective mass in the bottom row are signatures of the pseudogap.

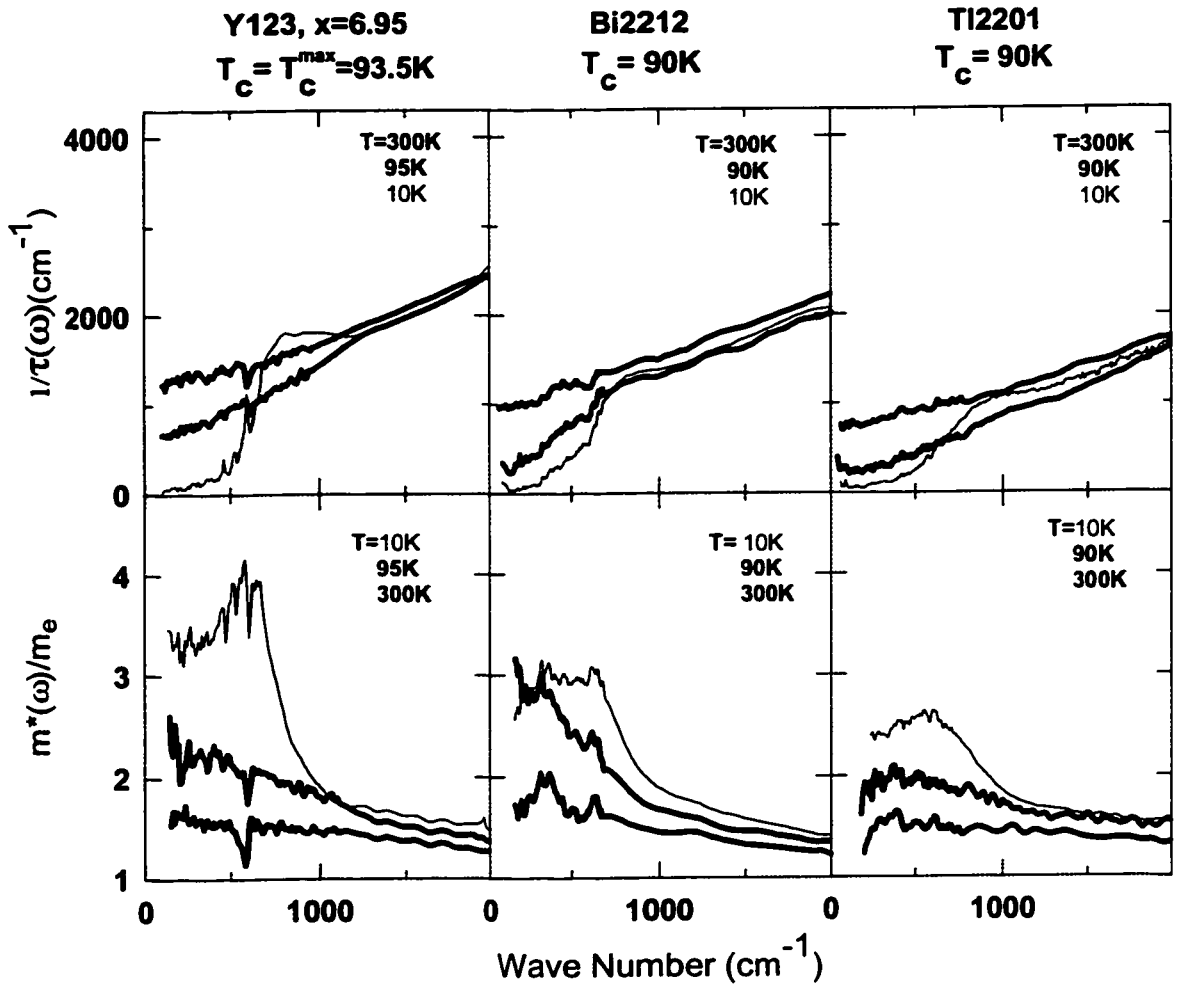

Figure 4.5: Scattering rate and effective mass for optimally doped cuprates. (After Puchkov *et al.*[148]) The 700 cm^{-1} feature associated with the pseudogap in underdoped samples is, for the most part, only seen in the superconducting state in optimally doped samples.

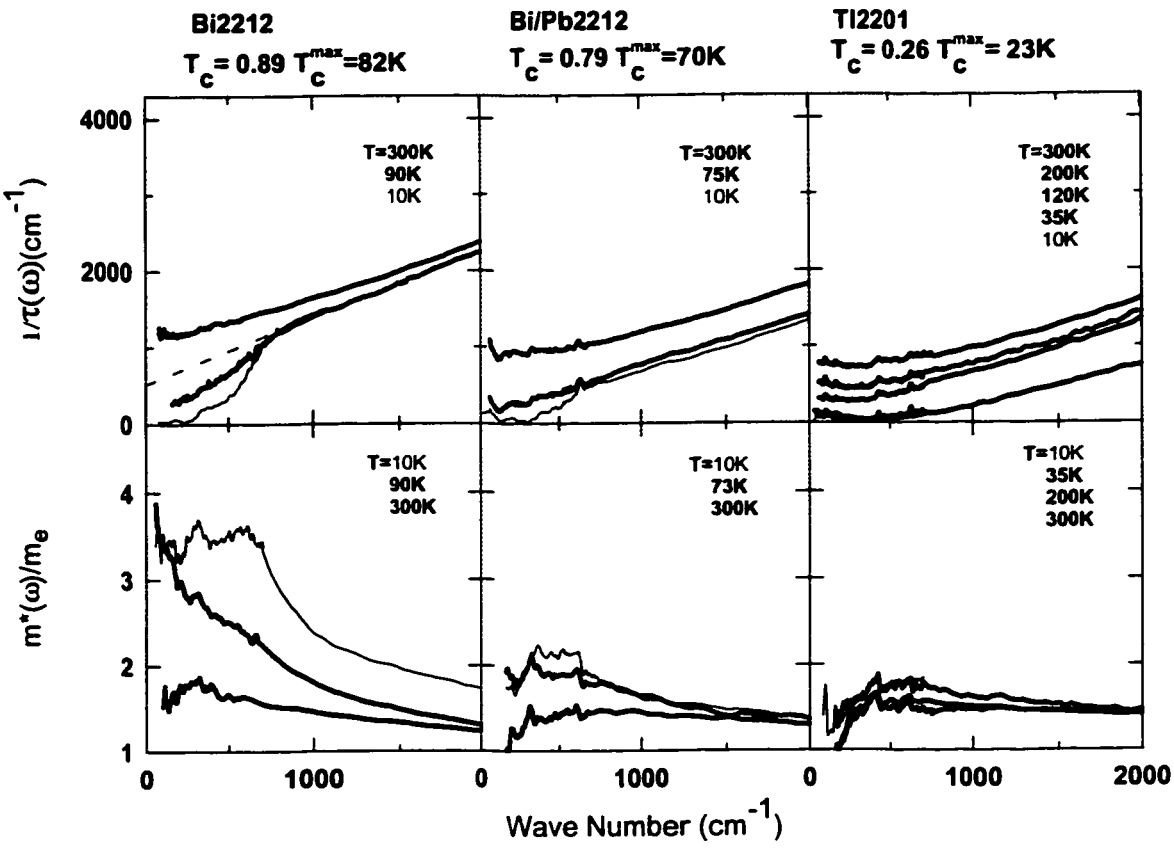

Figure 4.6: Scattering rate and effective mass for overdoped cuprates. (After Puchkov *et al.*[148]) In overdoped samples a temperature dependence is present at all frequencies although a feature at 700 cm^{-1} can often still be seen.

The comparison[148] in Figs. 4.4, 4.5 and 4.6 of infrared spectra of $YBa_2Cu_3O_x$ (Y-123), $YBa_2Cu_4O_8$ (Y-124), $Bi_2Sr_2CaCu_2O_{8+\delta}$ (Bi-2212) and $Tl_2Sr_2CuO_{6+\delta}$ (Tl-2201) show no dependence of gap size on doping level or even on which system is being measured. All samples show a gap of ≈ 700 cm^{-1}.

One explanation for this difference between the doping dependence of the gap in infrared measurements and that seen using other techniques may be that for reflectance in the clean limit, where $1/\tau(\omega) \ll 2\Delta$, onset of absorption does not occur until $\hbar\omega > (2\Delta + \hbar\Omega)$ where $\hbar\Omega$ is the frequency of a momentum conserving inelastic excitation. Gaps in the infrared response will therefore be larger by $\hbar\Omega$ than those seen in tunneling and Raman spectra and may in fact have a different doping dependence depending on the doping dependence of $\hbar\Omega$[151].

While Ref[148] makes it clear that the infrared gap shows no doping dependence and that its magnitude is the same for several materials, a relationship between gap size and maximum T_c cannot be ruled out since all of these materials have T_c near 93 K at optimal doping. In this chapter the *ab*-plane infrared reflectance of single crystal $HgBa_2Ca_2Cu_3O_{8+\delta}$ (Hg-1223) is reported in order to study the gap in the superconducting state of a material with a maximum T_c significantly higher than those of the other systems that have been studied previously[152].

4.3 Reflectance of $HgBa_2Ca_2Cu_3O_{8+\delta}$

The data reported here are for a nearly optimally doped single crystal of Hg-1223. For comparison purposes these results are presented along with data for an underdoped sample that were reported previously[153]. The crystals were grown in gold foil by a single step synthesis[141] and characterized by magnetic susceptibility[141], X-ray diffraction and wavelength dispersive spectrometry[154]. The nearly optimally doped crystal had a

T_c of 130 K and dimensions 0.4 × 0.3 × 0.03 mm^3. It's magnetic susceptibility is shown in Fig. 4.7. The underdoped sample had a T_c of 121 K and dimensions 0.6 × 0.5 × 0.04 mm^3. The smallest dimension is the c-axis or [001] direction with the [100] direction 45° from the two larger edges. In both crystals the width of the transition was about 6 K. Reflectance measurements between 40 and 8000 cm^{-1} were performed on as-grown ab-plane faces with a Michelson interferometer (Fig. 3.2) using three different detectors. A grating spectrometer (Fig. 3.1) with three additional detectors was used for the rest of the range up to 40,000 cm^{-1} (5 eV). The measurement procedure is described in detail in the first section of Chapter 3.

The ab-plane reflectance of the optimally doped crystal is shown in Fig. 4.8. The plasma edge can be seen near 10000 cm^{-1}, and at low temperature there is a striking temperature-dependent feature below 1000 cm^{-1}. In the optimally doped sample this is seen only in the three spectra below T_c. The inset of the figure shows a similar feature in the reflectance of the underdoped sample also at 1000 cm^{-1}. The presence of the feature in the 125 K data, which is now above the 121 K T_c, shows that it persists in the normal state, although at a somewhat lower frequency. Similar behavior in reflectance has been observed in other high T_c materials such as Bi-2212[148] where a feature appears in the region of 700 cm^{-1} well above T_c and shifts to slightly higher frequency in the superconducting state. Detailed analysis shows that the 700 cm^{-1} feature in the reflectance spectrum is the result of depressed quasiparticle scattering below this frequency at low temperature, a gap in the scattering rate spectrum. The observation of the feature at 1000 cm^{-1} in Hg-1223 suggests that in this material, as in other high-temperature superconductors, there is a gap in the scattering rate, but at a substantially higher energy.

The calculation of the optical conductivity and frequency-dependent scattering rate requires extrapolation of the reflectance to all frequencies for the Kramers-Kronig analysis. The spectra were extrapolated to high frequencies using the Bi-2212 data of Terasaki

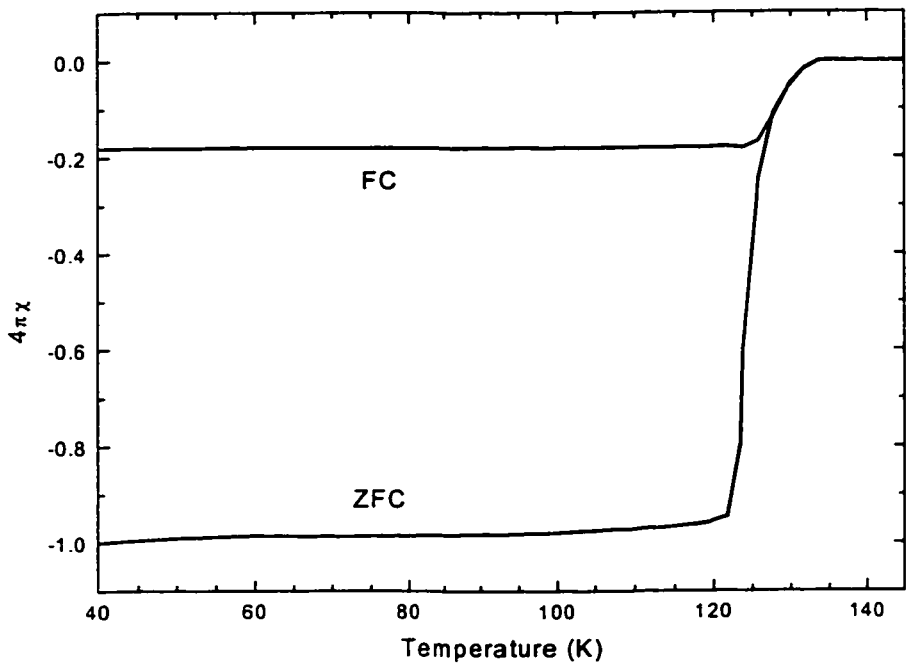

Figure 4.7: Magnetic susceptibility of $HgBa_2Ca_2Cu_3O_{8+\delta}$
The field-cooled (FC) and zero-field-cooled (ZFC) susceptibility of the nearly optimally doped sample shows an onset of superconductivity near 130 K. The susceptibility has been corrected for demagnetizing effects[141].

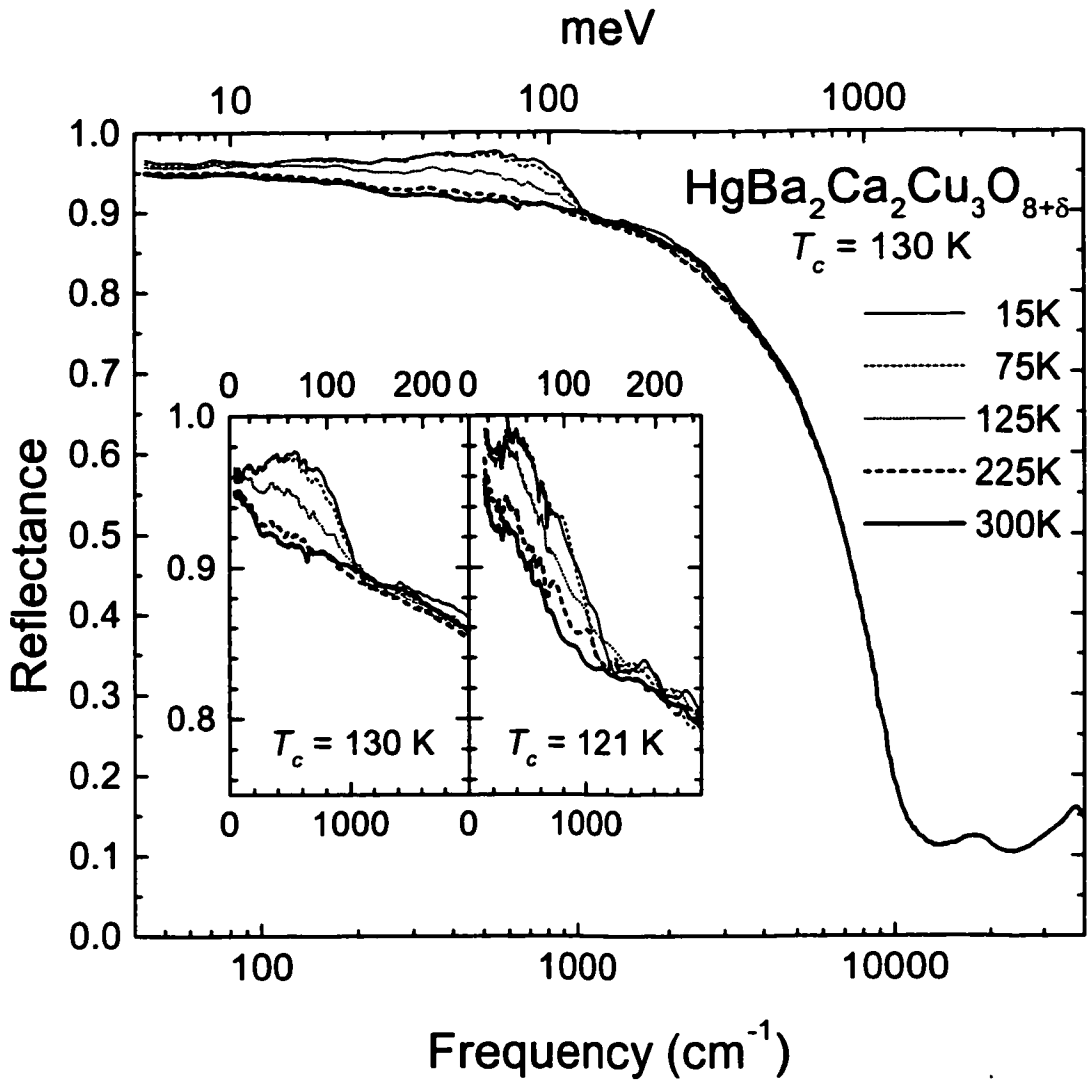

Figure 4.8: *ab*-plane reflectance of $HgBa_2Ca_2Cu_3O_{8+\delta}$.
The semi-log plot is the reflectance of the optimally doped crystal of with $T_c = 130$ K. The inset compares this to the reflectance of the underdoped sample with $T_c = 121$ K. The temperature dependence below 1000 cm^{-1} corresponds to a gap in the scattering rate.

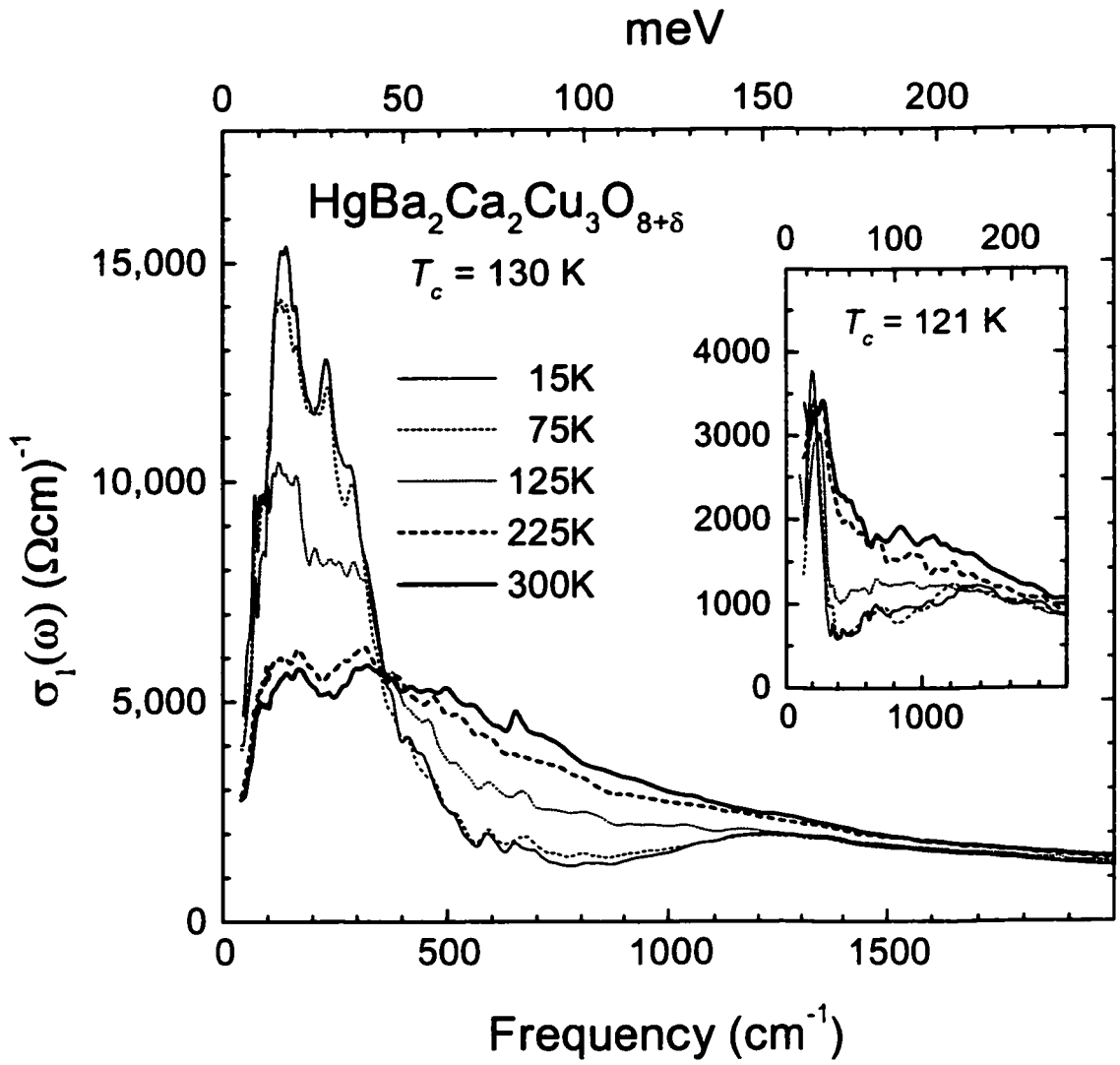

Figure 4.9: Optical conductivity of $HgBa_2Ca_2Cu_3O_{8+\delta}$.
The real part of the optical conductivity of the optimally doped crystal shows a marked transfer of spectral weight from $\omega < 1200$ cm^{-1} to a peak centered at 184 cm^{-1}. This peak is much narrower and weaker in the spectra shown in the inset for the underdoped sample.

et al.[155] above 5 eV, and using power law extrapolations: ω^{-1} above 25 eV and ω^{-4} above 124 eV. Below the lowest measured point at 43 cm^{-1} a Drude conductivity is assumed in the normal state and $1-\omega^2$ reflectance in the superconducting state. The experimental uncertainty of the reflectance is estimated to be ± 0.005. Combined with uncertainties due to the extrapolations, this gives an uncertainty in the optical conductivity of $\pm 8\%$ above 200 cm^{-1}. At low frequencies the uncertainty rises, reaching $\pm 40\%$ at 43 cm^{-1}. The resolution of the spectra is 20 cm^{-1} up to 680 cm^{-1} and 30 cm^{-1} up to 8000 cm^{-1}.

The real part of the optical conductivity of the optimally doped sample is shown in Fig. 4.9. As the temperature is lowered there is a transfer of spectral weight from a region between 360 and 1200 cm^{-1} to a peak centered at 184 cm^{-1}. There is an isosbestic point in the conductivity spectra at 360 cm^{-1} where the curves taken at different temperatures cross suggesting that there is a transfer of spectral weight from one component to another without either component changing lineshape. In this case one component is a Drude-like continuum below 1000 cm^{-1}, and the other is the peak at 184 cm^{-1}.

Such a peak is often seen in high-temperature superconductors where there is oxygen disorder[156, 157, 158] which, in Hg-1223, is expected more in optimally doped samples than in underdoped ones[159]. In agreement with this, the peak in the optical conductivity spectra of the underdoped sample, shown in the inset of Fig. 4.9, is narrower and weaker. It should also be noted that Hg-1223 crystals are prone to surface deterioration with exposure to air[160]. The underdoped sample was measured soon after growth, and it is possible that some of the absorption in the optimally doped sample, measured a year later, could be attributed to the influence of parasitic phases[160]. It is unlikely that the peak is due to diffraction from the small sample. Diffraction effects should nearly cancel out due to the technique of evaporating gold onto the sample to create a reference.

It is possible to estimate the plasma frequency of the superconducting condensate

by comparing the spectral weights, or total area under the conductivity curve, above and below T_c. This follows from the conductivity sum rule which states that the total spectral weight is constant at all temperatures. Below T_c the spectral weight associated with the condensate is contained in a delta function at zero frequency where it cannot be seen directly in the σ_1 spectrum. However, the sum of this hidden spectral weight and the rest of the spectral weight at finite frequency will be equal to the finite-frequency spectral weight in the normal state where there is no condensate. Hence[157],

$$\omega_{pS}^2 = \frac{120}{\pi} \int_0^\infty [\sigma_{1n}(\omega) - \sigma_{1s}(\omega)] d\omega \tag{4.4}$$

where ω_{pS} is the plasma frequency of the condensate in wavenumbers, σ_{1n} and σ_{1s} are the normal and superconducting state conductivities in $(\Omega\text{cm})^{-1}$, and ω is frequency in wavenumbers.

Applying this to the spectra in the inset of Fig. 4.9 for the underdoped sample gives $\omega_{pS} = 7850 \pm 50$ cm^{-1}. This gives a value for the London penetration depth[153] of $\lambda_L = 1/2\pi\omega_{pS} = 200 \pm 30$ nm which is in agreement with penetration depth measurements of Panagopoulos *et al.* on magnetically aligned powders[161]. The result for the nearly optimally doped sample, however, is more perplexing. The application of Eq. 4.4 to the spectra in Fig. 4.9 leads to a superconducting plasma frequency that is essentially zero with an upper limit of about 1000 cm^{-1}. This is because most of the spectral weight which disappears between 360 and 1200 cm^{-1} as the temperature is lowered goes to the peak centered at 184 cm^{-1} leaving very little for the condensate.

This result can be confirmed by analyzing the imaginary part of the conductivity σ_2, or equivalently, the real part of the dielectric function ϵ_1. Fig. 4.10 shows ϵ_1 for the nearly optimally doped sample. The sharp decrease below 400 cm^{-1} is consistent with a suppression of the quasiparticle scattering rate, and the unusual increase below 200 cm^{-1} is due to the 184 cm^{-1} peak in σ_1. A plot of ϵ_1 *vs.* ω^{-2} will have a slope equal

to ω_{pS}^2 at low frequency (see Eq. 1.8). This analysis for the underdoped sample[153] gives $\omega_{pS} = 8000 \pm 500$ cm^{-1} in good agreement with the sum rule analysis. The inset of Fig. 4.10 shows ϵ_1 *vs.* ω^{-2} for the nearly optimally doped sample. At high frequency the slope would give $\omega_{pS} = 14000 \pm 500$ cm^{-1}, but this technique should be applied in the low frequency limit. Below 400 cm^{-1} this gives $\omega_{pS} = 0 \pm 500$ cm^{-1} completely consistent with the result from the sum rule.

It therefore appears that the 184 cm^{-1} peak in σ_1 for the nearly optimally doped sample gains spectral weight at the expense of the condensate. This could also be true for the underdoped sample, although the effect would be less significant since the peak is much weaker in that case. Corson *et al.*[162], using time-domain terahertz spectroscopy on thin films of $Bi_2Sr_2CaCu_2O_{8+\delta}$, also find evidence for a low-frequency quasipartical mode that gains spectral weight at the expense of the condensate. Unlike the mode in Hg-1223 which is centred at 184 cm^{-1} and 300 cm^{-1} wide, they model their mode as a Lorentzian centred at zero frequency with a width of only 8 cm^{-1}. It takes about 30% of the spectral weight of the condensate while the mode in Hg-1223 takes closer to 100%.

For the nearly optimally doped sample, the overall infrared spectral weight up to 8000 cm^{-1}, expressed as a squared plasma frequency from the conductivity partial sum rule, is $I(8000) = \frac{120}{\pi} \int_0^{8000} \sigma_1(\omega) d\omega = 4.3 \times 10^8$ cm^{-2}. This is a factor of 1.3 higher than the comparable figure for the *a*-axis spectral weight of the two-layer Y-123 at optimal doping and a factor of 2.2 higher than that for Bi-2212[148]. In terms of spectral weight per plane copper, the Hg-1223 value is higher by factors of 1.33 and 1.53 respectively.

The frequency-dependent scattering rate was calculated using the extended Drude model (see Eq. 4.3) and is shown in Fig. 4.11 for the optimally doped sample. Here the gap is clearly seen as a temperature-dependent suppression of the scattering rate below 1000 cm^{-1}. There is a substantial residual scattering rate of 300 cm^{-1} at low frequencies which is consistent with the 300 cm^{-1} width of the low frequency peak in the optical

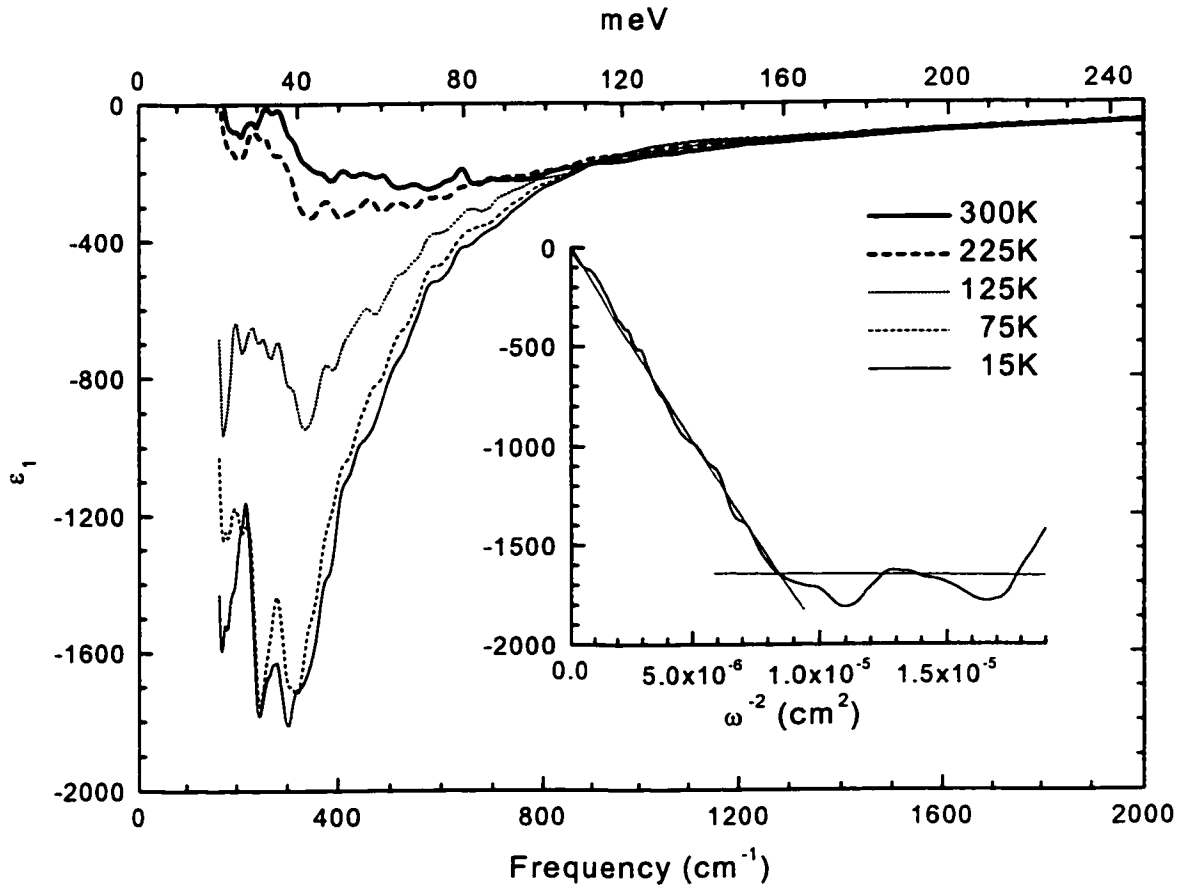

Figure 4.10: The real part of the dielectric function of $HgBa_2Ca_2Cu_3O_{8+\delta}$. The square of the plasma frequency of the condensate can be determined from the slope of ϵ_1 *vs.* ω^{-2} at low frequencies.

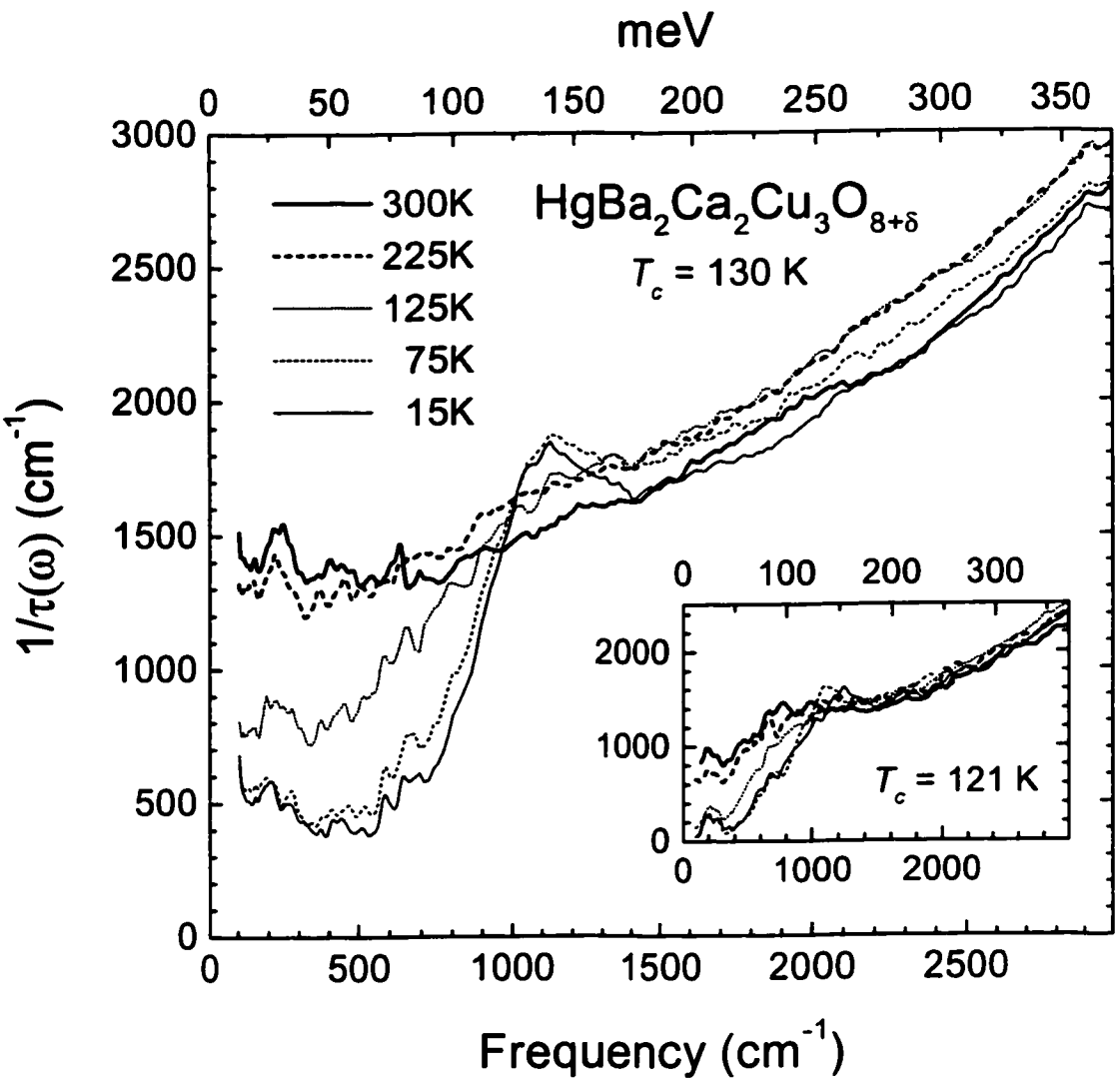

Figure 4.11: Scattering rate of $HgBa_2Ca_2Cu_3O_{8+\delta}$.
The frequency-dependent scattering rate of the optimally doped crystal shows a gap. or suppression of scattering, below 1000 cm^{-1}. The inset shows the spectra for the underdoped sample.

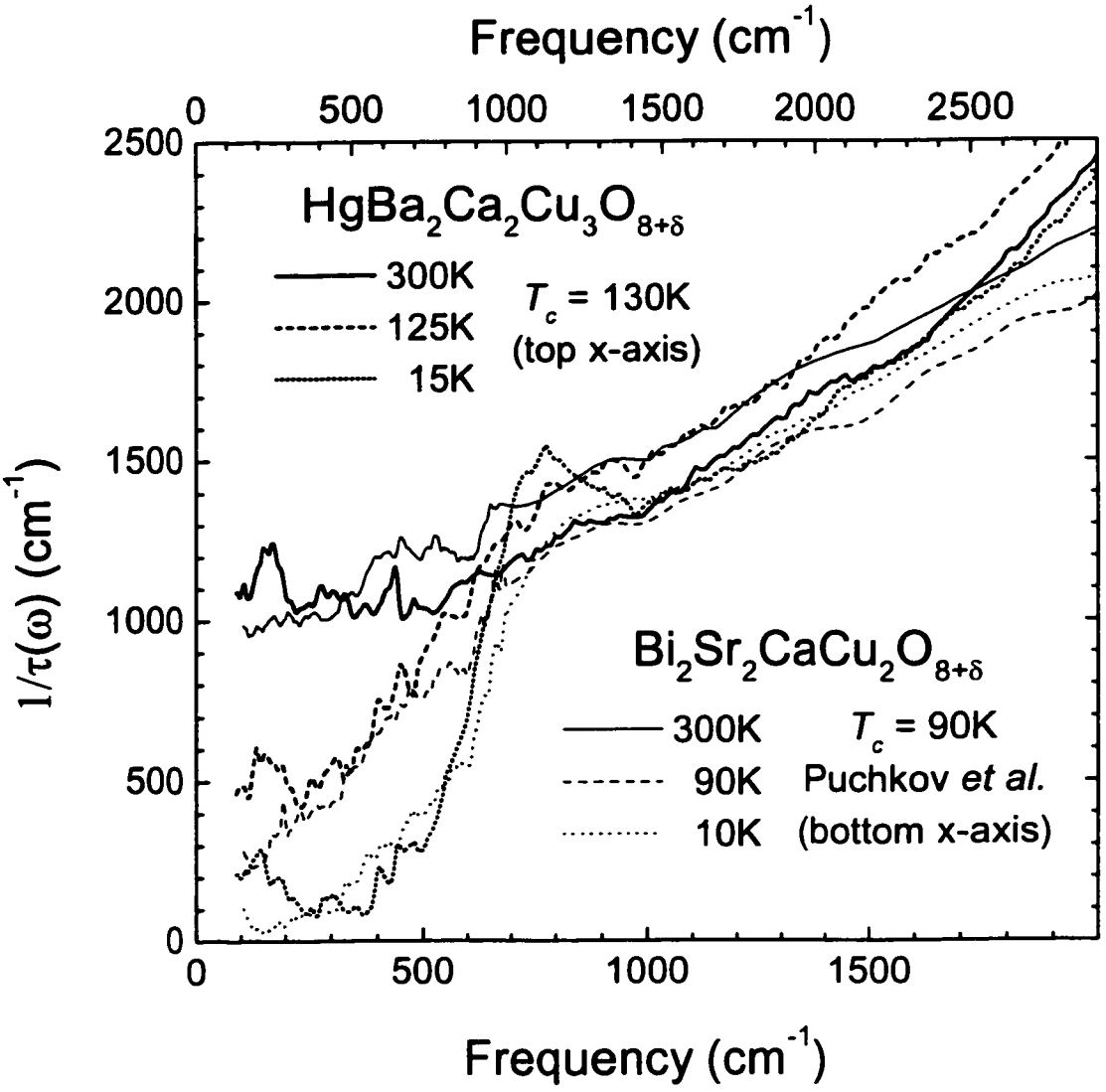

Figure 4.12: A comparison of the scattering rate with that of Bi-2212. The scattering rate is remarkably similar to that of Bi-2212 from Puchkov *et al.*[148]. The frequency scales differ by a factor of 135/93 = 1.45. and a frequency-independent scattering rate of 300 cm^{-1} has been subtracted from the Hg-1223 data.

conductivity at low temperature. The scattering rate of the underdoped sample is shown in the inset of Fig. 4.11. It shows no residual scattering, and is about 300 cm^{-1} lower than that of the optimally doped sample over the entire range shown.

The two samples also show different gap onset temperatures, T^*. For the underdoped sample $T^* > 300$ K, while for the optimally doped sample 125 K $< T^* <$ 225 K. These values are consistent with measurements of DC resistivity[163] and NMR ^{63}Cu T_1[164] that give T^* values of 320 K and 230 K respectively. The doping dependence is similar to that of other high-temperature superconductors[148].

The gap feature at 1000 cm^{-1} in Hg-1223 is at a considerably higher frequency than the corresponding features in Y-123, Y-124, Bi-2212 and Tl2201 which are all at about 700 cm^{-1}[148]. Since these superconductors also have similar values of $T_c \approx 93$ K, the gaps are in the same ratio (1000/700 = 1.43) as the transition temperatures (135/93 = 1.45).

Julien *et al.* analyzing hyperfine NMR shift data find a much higher transferred hyperfine coupling constant B in Hg-1223 than in Y-123, suggesting a higher in-plane superexchange J between the copper spins[164]. With the finding of a larger gap in the Hg-1223 material these results support the idea of a superconducting mechanism closely tied to the antiferromagnetism of the copper oxygen planes.

Fig. 4.12 shows a comparison of the scattering rate of Hg-1223 with that of Bi-2212 from Puchkov *et al.*[148]. The frequency scales differ by the ratio of the values of maximum T_c, 135/93, and a frequency-independent scattering rate of 300 cm^{-1} has been subtracted from the Hg-1223 data to take the residual scattering into account. The similarity of the scattering rate spectra of the two-layer Bi-based superconductor with those of the three-layer Hg material is striking. A slight overshoot like the one seen in the 1200 cm^{-1} region for Hg-1223 is also seen in several other optimally doped materials[148].

$La_{2-x}Sr_xCuO_4$ is the only material for which *ab*-plane reflectance measurements show

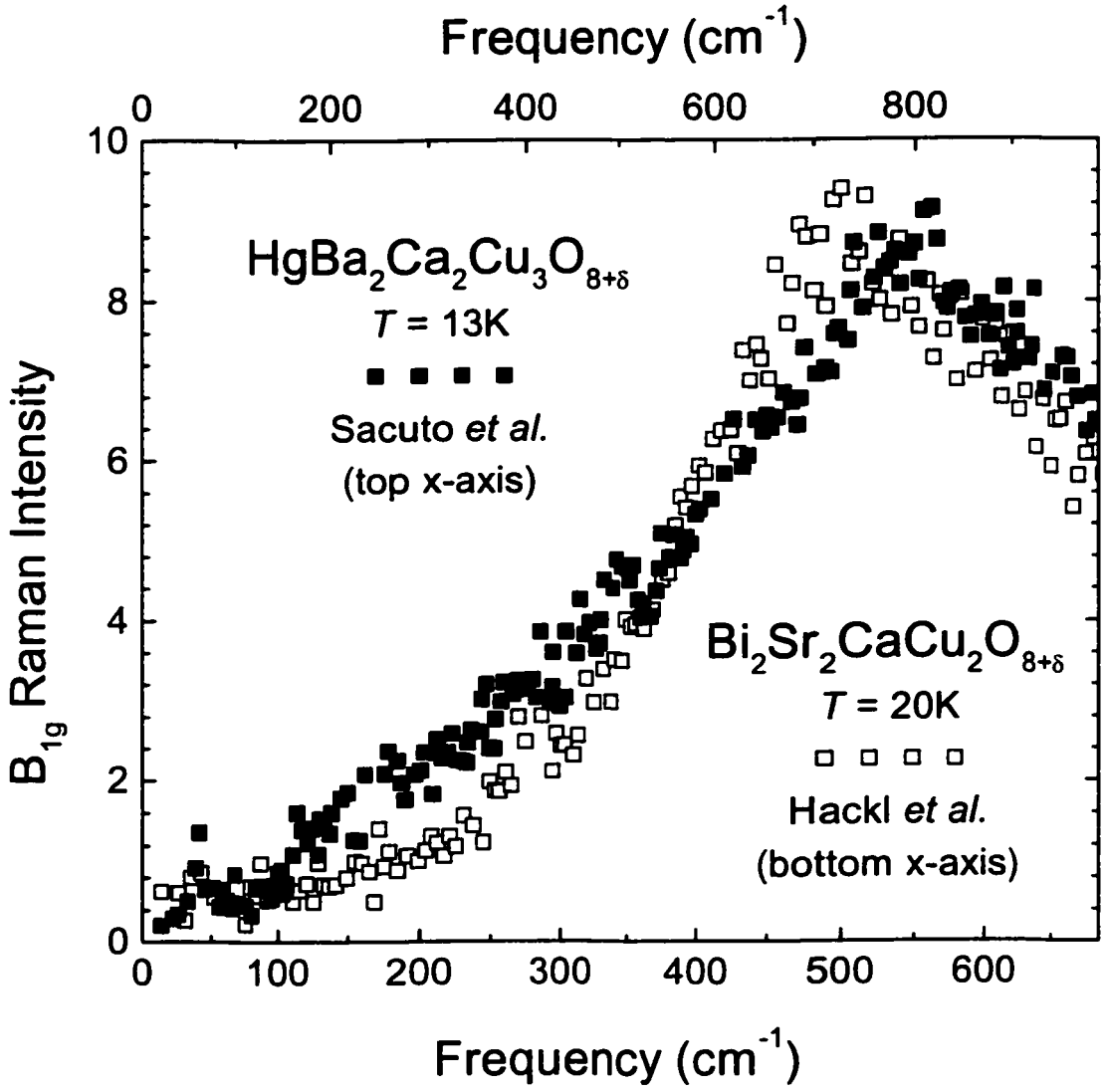

Figure 4.13: B_{1g} Raman Intensity.
A comparison of the data for Hg-1223 measured by Sacuto *et al.*[159] with that of Bi-2212 measure by Hackl *et al.*[167]. The frequency scales differ by a factor of $135/93 = 1.45$.

a gap that does not scale with maximum T_c. It has a gap of about 700 cm^{-1} and a maximum T_c of only 40 K. Many of its other properties, however, are also inconsistent with the gap properties observed in other cuprate superconductors, and it has been suggested that this may be due to the presence of paramagnetic centres intrinsic to the random alloy[144]. It is reasonable to conclude that $La_{2-x}Sr_xCuO_4$ should be treated as a special case.

Because the gap seen in reflectance measurements includes a momentum conserving inelastic excitation of energy $\hbar\Omega$, it is difficult to make direct comparisons to gap sizes measured using other techniques. Nevertheless, these other measurements also show evidence for a universal scaling between gap size and T_c. This is demonstrated in an interpretation by Williams *et al.*[165] of NMR data on several high-temperature superconductors. In an ARPES measurement Harris *et al.*[166] find that the gap in $Bi_2Sr_{2-x}La_xCuO_{6-\delta}$, which has a maximum T_c of 29 K, is roughly three times smaller than the gap in Bi-2212 and hence seems to scale with maximum T_c. A similar scaling can be seen in B_{1g} Raman spectra. Fig. 4.13 is a comparison of the B_{1g} Raman intensity of nearly optimally doped Hg-1223 measured by Sacuto *et al.*[159] with that of Bi-2212 measured by Hackl *et al.*[167]. Again the frequency scales differ by a factor of $135/93 = 1.45$. The positions of the maxima at 500 and 780 cm^{-1} are proportional to the superconducting gaps.

A universal scaling between gap size and maximum T_c is far from trivial. For example, in conventional electron-phonon mediated superconductors, $2\Delta/k_bT_c = 3.5$ for the lowest T_c materials, but *rises* with T_c to as high as 5.2[168]. In the current study no change is seen in the gap ratio as maximum T_c is enhanced by 40%. In addition, this scaling is seen despite the presence of a momentum conserving inelastic excitation which therefore may also scale with maximum T_c. In order to further investigate this remarkable behaviour of the cuprate superconductors, estimates of gap size need to be obtained for more systems

with T_c significantly different from 93 K, particularly the two-layer Hg compound, Hg-1212, and the two- and three-layer Tl compounds, Tl-2212 and Tl-2223.

Chapter 5

CONCLUSIONS

While the three materials discussed in this thesis are different in many respects, they do have several similarities. Both doped $CuGeO_3$ and undoped $HgBa_2Ca_2Cu_3O_{8-\delta}$ undergo antiferromagnetic transitions at low temperature. These same magnetic spins drive the spin-Peierls transition in $CuGeO_3$ and may be responsible for the coupling mechanism in high-temperature superconductors. In κ-$(ET)_2Cu[N(CN)_2]Br$ too, there is evidence for strong antiferromagnetic fluctuations. Another similarity is low dimensionality. The spin-Peierls transition in $CuGeO_3$ is due to its quasi-one-dimensional nature, and the quasi-two-dimensional nature of the high-temperature superconductors may be key to their unconventional superconductivity. Clues to understanding the high-temperature superconductors may come from studying κ-$(ET)_2Cu[N(CN)_2]Br$ and related organic superconductors that share their two-dimensionality. In this thesis, the techniques of far-infrared spectroscopy have proven to be useful in studying all of these materials.

A newly discovered local librational mode has been reported in doped $CuGeO_3$. This mode involves the motion of the GeO_4 tetrahedra surrounding the dopant ion. The effect was demonstrated for Zn, Ni and Cd dopants, all of which replace Cu in the crystal structure. The effect was shown not to occur for Si doping where the Ge atoms are replaced. The low energy of the mode is consistent with the relative ease with which the GeO_4 tetrahedra can be tipped as is also demonstrated by a low energy phonon and the spin-Peierls distortion itself that both involve a tipping of the tetrahedra. The potential well for the librational mode is highly anharmonic, being essentially square with a central

barrier. The resulting multiline spectrum showing a temperature dependence consistent with the Boltzmann factors for the individual levels of the mode is as striking as it is unusual.

The interplane measurements of κ-$(ET)_2Cu[N(CN)_2]Br$ are the first such measurements on any of the two-dimensional ET-based organic superconductors. The interplane resistivity of this material raises questions about the nature of the interplane transport. The magnitude of the resistivity suggests incoherence, while the temperature dependence suggests coherence. The infrared measurements find no evidence of a Drude peak in the optical conductivity down to 30 cm^{-1} confirming that the transport is incoherent. The temperature dependence of the resistivity can be explained with a model of defect-assisted interlayer transport that results in an interplane resistivity that mirrors the temperature dependence of the in-plane resistivity. The infrared spectra also show several phonon lines that can be identified with internal modes of the ET molecule.

The in-plane measurements of $HgBa_2Ca_2Cu_3O_{8-\delta}$ are of particular interest because of the high transition temperature of this material, even compared to other high-temperature superconductors. As in other high-temperature superconductors, a pseudogap can be seen in the spectra, but here the pseudogap is considerably larger. Previously measured materials have all shown a pseudogap of similar magnitude, however their transition temperatures were also very similar. The fact that the pseudogap in $HgBa_2Ca_2Cu_3O_{8-\delta}$ is larger by the same factor by which its transition temperature is higher suggests a relationship between pseudogap size and transition temperature. While there is some evidence in other studies to support this, it is difficult to make strong conclusions because of some of the differences in the pseudogaps seen in infrared studies compared to results using other techniques.

All three studies reported in this thesis call for further research. The highly anharmonic nature of the resonant mode found in doped $CuGeO_3$ provides an opportunity

for studying local lattice dynamics through careful analysis of the shifts in line positions as dopant ions are changed. The work on κ-$(ET)_2Cu[N(CN)_2]Br$ should be extended to other two-dimensional organic materials. The variety of different ET networks which make up the conducting layers in the different materials could very well result in differing degrees of coherence. Due to the relatively small size of the $HgBa_2Ca_2Cu_3O_{8-\delta}$ crystal studied in this thesis, the measurement of the infrared spectra was difficult, limiting the number of temperatures for which data were collected. It would be of great interest to measure spectra just above the transition temperature since this is where the pseudogap is truly distinct from a superconducting gap. There is some evidence for a small change in gap size as the transition temperature is crossed in other materials that might be larger in $HgBa_2Ca_2Cu_3O_{8-\delta}$ which has a larger gap. Also, it is important to measure other materials with T_c significantly different from 93 K, particularly the two-layer Hg compound, Hg-1212, and the two- and three-layer Tl compounds, Tl-2212 and Tl-2223.

Over the years, infrared and far-infrared spectroscopy has helped unravel many of the mysteries of the solid state. It has continued to prove useful in this work on $CuGeO_3$, κ-$(ET)_2Cu[N(CN)_2]Br$ and $HgBa_2Ca_2Cu_3O_{8-\delta}$. It is clear that it will be one of the key experimental techniques of solid state physicists for years to come.

Bibliography

[1] C. Kittel, *Introduvtion to Solid State Physics*, John Wiley & Sons Inc., (New York), 1986.

[2] N.W. Ashcroft and N.D. Mermin, *Solid State Physics*, Saunders College, Philadelphia, 1976.

[3] A.S. Baker and A.J. Sievers, Rev. Mod. Phys. **47**, S2 (1975).

[4] J. Bardeen, L.N. Cooper, and J.R. Schrieffer, Phys. Rev. **108**, 1175 (1957).

[5] H.K. Onnes, Proc. Royal Acad. (Akad. van Wetenschappen, Amsterdam) **14**, 818 (1911) (equivalent with Leiden Comm. **124c**; see also Leiden Comm. **119**, **120b** (1911) and Proc. Royal Acad. (Akad. van Wetenschappen, Amsterdam) **14**, 113 (1911) (equivalent with Leiden Comm. **122b**.

[6] J.G. Bednorz and K.A. Müller, Z. Phys. B **64**, 189 (1986).

[7] J.E. Eldridge and C.C. Homes, Phys. Rev. B **43**, 13971 (1991).

[8] S.B. Nam, Phys. Rev. **156**, 487 (1967).

[9] J.J. McGuire, T. Rõõm, T.E. Mason, T. Timusk, H. Dabkowska, S.M. Coad, and D.McK. Paul, Phys. Rev. B **59**, 1157 (1999).

[10] J.J. McGuire, M.Sc. Thesis, McMaster University, 1996.

[11] D.H. Martin and E. Puplett, Infrared Phys. **10**, 105 (1969).

[12] C.D. Porter and D.B. Tanner, Int. J. Infra. **4**, 273 (1983).

[13] T. Rõõm, U. Nagel, E. Lippmaa, H. Kageyama, K. Onizuka, and Y. Ueda, Phys. Rev. B **61**, 14342 (2000).

[14] M. Hase, I. Terasaki, and K. Uchinokura, Phys. Rev. Lett. **70**, 3651 (1993).

[15] J.W. Bray, L.V. Interrante, I.S. Jacobs, and J.C. Bonner, in *Extended Linear Chain Compounds*, edited by J.S. Miller (Plenum Press, New York, 1983), Vol. 3, p. 353.

[16] K.D. Hammonds, H. Deng, V. Heine, and M.T. Dove, Phys. Rev. Lett. **78**, 3701 (1997).

[17] K. Hirota, D.E. Cox, J.E. Lorenzo, G. Shirane, J.M. Tranquada, M. Hase, K. Uchinokura, H. Kojima, Y. Shibuya, and I. Tanaka, Phys. Rev. Lett. **73**, 736 (1994).

[18] J.L. Musfeldt, Y.J. Wang, S. Jandl, M. Poirier, A. Revcolevschi, and G. Dhalenne, Phys. Rev. B **54**, 469 (1996).

[19] M. Hase, I. Terasaki, K. Uchinokura, M. Tokunaga, N. Miura, and H. Obara, Phys. Rev. B **48**, 9616 (1993).

[20] V. Kiryukhin, B. Keimer, J.P. Hill, S.M. Coad, and D.McK. Paul, Phys. Rev. B **54**, 7269 (1996).

[21] B. Grenier, L.P. Regnault, J.E. Lorenzo, J.P. Boucher, A. Hiess, G. Dhalenne, and A. Revcolevschi, Phys. Rev. B **62**, 12206 (2000).

[22] P.H.M. van Loosdrecht, S. Huant, G. Martinez, G. Dhalenne, and A. Revcolevschi, Phys. Rev. B **54**, R3730 (1996).

[23] K. Takehana, T. Takamasu, M. Hase, G. Kido, and K. Uchinokura, Phys. Rev. B **62**, 5191 (2000).

[24] Z.V. Popović, S.D. Dević, V.N. Popov, G. Dhalenne, and A. Revcolevschi, Phys. Rev. B **52**, 4185 (1995).

[25] T.M. Brill, J.P. Boucher, J. Voiron, G. Dhalenne, A. Revcolevschi, and J.P. Renard, Phys. Rev. Lett. **73**, 1545 (1994).

[26] Y. Sasago, N. Koide, K. Uchinokura, M.C. Martin, M. Hase, K. Hirota, and G. Shirane, Phys. Rev. B **54**, R6835 (1996).

[27] N. Koide, Y. Uchiyama, T. Hayashi, T. Masuda, Y. Sasago, K. Uchinokura, K. Manabe, and H. Ishimoto, preprint cond-mat/9805095.

[28] T. Masuda, A. Fujioka, Y. Uchiyama, I. Tsukada, and K. Uchinokura, Phys. Rev. Lett. **80**, 4566 (1998).

[29] J.-G. Lussier, S.M. Coad, D.F. McMorrow, and D.McK. Paul, J. Phys.: Condens. Matter **7**, L325 (1995).

[30] M. Hase, K. Uchinokura, R.J. Birgeneau, K. Hirota, and G. Shirane, J. Phys. Soc. Jpn. **65**, 1392 (1996).

[31] P. Fronzes, M. Poirier, A. Revcolevschi, and G. Dhalenne, Phys. Rev. B **55**, 8324 (1995).

[32] M.C. Martin, M. Hase, K. Hirota, G. Shirane, Y. Sasago, N. Koide, and K. Uchinokura, Phys. Rev. B **56**, 3173 (1997).

[33] J.P. Renard, K. Le Dang, P. Veillet, G. Dhalenne, A. Revcolevschi, and L.P. Regnault, Europhys. Lett. **30**, 475 (1995).

[34] L.P. Regnault, J.P. Renard, G. Dhalenne, and A. Revcolevschi, Europhys. Lett. **32**, 579 (1995).

[35] M. Poirier, R. Beaudry, M. Castanguay, M.L. Plumer, G. Quirion, F.S. Razavi, A. Revcolevschi, and G. Dhalenne, Phys. Rev. B **52**, R6971 (1995).

[36] S. Coad, J.-G. Lussier, D.F. McMorrow, and D.McK. Paul, J. Phys.: Condens. Matter **8**, 6251 (1996).

[37] Y.J. Wang, V. Kiryukhin, R.J. Birgeneau, T. Masuda, I. Tsukada, and K. Uchinokura, Phys. Rev. Lett. **83**, 1676 (1999).

[38] T. Masuda, I. Tsukada, K. Uchinokura, Y.J. Wang, V. Kiryukhin, and R.J. Birgeneau, Phys. Rev. B **61**, 4103 (2000).

[39] V. Kiryukhin, Y.J. Wang, S.C. LaMarra, R.J. Birgeneau, T. Masuda, I. Tsukada, and K. Uchinokura, Phys. Rev. B **61**, 9527 (2000).

[40] J. Takeya, I. Tsukada, Y. Ando, T. Masuda, and K. Uchinokura, Phys. Rev. B **62**, 9260 (2000).

[41] A. Damascelli, D. van der Marel, F. Parmigiani, G. Dhalenne, and A. Revcolevschi, Phys. Rev. B **56**, R11373 (1997).

[42] A. Damascelli, D. van der Marel, F. Parmigiani, G. Dhalenne, and A. Revcolevschi, Physica B **244**, 114 (1998).

[43] H. Völlenkle, A. Wittmann, and H. Nowotny, Monatsh. Chem. **98**, 1352 (1967).

[44] G.B. Martins, E. Dagotto, and J.A. Riera, Phys. Rev. B **54**, 16032 (1996).

[45] M. Braden, G. Wilkendorf, J. Lorenzana, M. Aïn, G.J. McIntyre, M. Behruzi, G. Heger, G. Dhalenne, and A. Revcolevschi, Phys. Rev. B **54**, 1105 (1996).

[46] R.D. Shannon, Acta Cryst. **A32**, 751 (1976).

[47] A. Damascelli, D. van der Marel, G. Dhalenne, and A. Revcolevschi, Phys. Rev. B **61**, 12063 (2000).

[48] M. Isobe and Y. Ueda, J. Phys. Soc. Jpn. **65**, 1178 (1996).

[49] Y. Fujii, H. Nakao, T. Yosihama, M. Nishi, K. Nakajima, K. Kakurai, M. Isobe, Y. Ueda, and H. Sawa, J. Phys. Soc. Jpn. **66**, 326 (1997).

[50] W. Schnelle, Yu. Grin, and R.K. Kremer, Phys. Rev. B **59**, 73 (1999).

[51] T. Ohama, H. Yasuoka, M. Isobe, and Y. Ueda, Phys. Rev. B **59**, 3299 (1999).

[52] V.C. Long, Z. Zhu, J.L. Musfeldt, X. Wei, H.-J. Koo, M.-H. Whangbo, J. Jegoudez, and A. Revcolevschi, Phys. Rev. B **60**, 15721 (1999).

[53] A. Damascelli, C. Presura, D. van der Marel, J. Jegoudez, and A. Revcolevschi, Phys. Rev. B **61**, 2535 (2000).

[54] R.C. Newman, Adv. Phys. **18**, 545 (1969).

[55] A.J. Sievers and S. Takeno, Phys. Rev. **140**, A1030 (1965).

[56] L.H. Green and A.J. Sievers, Phys. Rev. B **31**, 3948 (1985).

[57] B.N. Ganguly, R.D. Kirby, M.V. Klein, and G.P. Montgomery, Phys. Rev. Lett. **28**, 307 (1972).

[58] S.A. Mabud and F. Luty, Bull. Amer. Phys. Soc. **28**, 452 (1983).

[59] S.A. Hayward, A.K.A. Pryde, R.F. de Dombal, M.A. Carpenter, and M.T. Dove, Phys. Chem. Min. **27**, 285 (2000).

[60] M.T. Dove, A.K.A. Pryde, and D.A. Keen, Mineral. Mag. **64**, 267 (2000).

[61] M. Gambhir, M.T. Dove, and V. Heine, Phys. Chem. Min. **26**, 484 (1999).

[62] G.G. Naumis, Phys. Rev. B **61**, 9205 (2000).

[63] M.J. Harris, S.M. Bennington, M.T. Dove, and J.M. Parker. Physica B **263-264**, 357 (1999).

[64] M.J. Harris, M.T. Dove, and J.M. Parker. Mineral. Mag. **64**, 435 (2000).

[65] K. Trachenko, M.T. Dove, K.D. Hammonds, M.J. Harris, and V. Heine, Phys. Rev. Lett. **81**, 3431 (1998).

[66] M.T. Dove, K.D. Hammonds, M.J. Harris, V. Heine, D.A. Keen, A.K.A. Pryde, K. Trachenko, and M.C. Warren, Mineral. Mag. **64**, 377 (2000).

[67] C.C. Homes, M. Reedyk, D.A. Cradles, and T. Timusk, Appled Optics **32**, 2976 (1993).

[68] J.M. Williams, A.J. Schultz, U. Geiser, K.D. Carlson, A.M. Kini, H.H. Wang, W.-K. Kwok, M.-H. Whangbo, J.E. Schirber, Science **252**, 1501 (1991).

[69] D. Jérome, Science **252**, 1509 (1991).

[70] A.M. Kini, U. Geiser, H.H. Wang, K.D. Carlson, J.M. Williams, W.K. Kwok, K.G. Vandervoort, J.E. Thompson, D.L. Stupka, D. Jung, and M.H. Whangbo. Inorg. Chem. **29**, 2555 (1990).

[71] Yu. V. Suchko, V.A. Bondarenko, R.A. Petrosov, N.D. Kushch, and E.B. Yagubskii. J. Phys. I France **2**, 1375 (1991).

[72] L.I. Buravov, N.D. Kushch, V.A. Merzhanov, M.V. Osherov, A.G. Khomenko, and E.B. Yagubskii, J. Phys. I France **2**, 1257 (1992).

[73] X. Su, F. Zuo, J.A. Schlueter, M.E. Kelly, and J.M. Williams, Phys. Rev. B **57**, R14056 (1998).

[74] F. Zuo, X. Su, P. Zhang, J.A. Schlueter, M.E. Kelly, and J.M. Williams. Phys. Rev. B **57**, 5610 (1998).

[75] F. Zuo, J.A. Schlueter, and J.M. Williams, Phys. Rev. B **60**, 574 (1999).

[76] U. Geiser, A.M. Kini, H.H. Wang, M.A. Beno, and J.M. Williams, Acta Cryst. **C47**, 190 (1991).

[77] V. Kataev, G. Winkel, D. Khomskii, D. Wohlleben, W. Crump, K.F. Tebbe, and J. Hahn, Solid State Commun. **83**, 435 (1992).

[78] X. Su, F. Zuo, J.A. Schlueter, M.E. Kelly, and J.M. Williams, Solid State Commun. **107**, 731 (1998).

[79] M.A. Tanatar, T. Ishiguro, T. Kondo, and G. Saito, Phys. Rev. B **61**, 3278 (2000).

[80] H. Akutsu, K. Saito, and M. Sorai, Phys. Rev. B **61**, 4346 (2000).

[81] H. Ito, M. Watanabe, Y. Nogami, T. Ishiguro, T. Komatsu, G. Saito, and N. Hosoito, J. Phys. Soc. Japan **60**, 3230 (1991).

[82] A. Kawamoto, K. Miyagawa, and K. Kanoda, Phys. Rev. B **55**, 14140 (1997).

[83] X. Su, F. Zuo, J.A. Schlueter, A.M. Kini, and J.M. Williams, Phys. Rev. B **58**, 2944 (1998).

[84] E. Griesshaber, M. Schiller, D. Schweitzer, I. Heinen, and W. Strunz, Physica C **317-318**, 421 (1999).

[85] H. Mayaffre, P. Wzietek, C. Lenoir, D. Jérome, and P. Batail, Europhys. Lett. **28**, 205 (1994).

[86] A. Kawamoto, K. Miyagawa, Y. Nakazawa, and K. Kanoda, Phys. Rev. Lett. **74**, 3455 (1995).

[87] S.M. De Soto, C.P. Slichter, A.M. Kini, H.H. Wang, U. Geiser, and J.M. Williams, Phys. Rev. B **54**, 16101 (1996).

[88] K. Frikach, M. Poirier, M. Castonguay, and K.D. Truong, Phys. Rev. B **61**, 6491 (2000).

[89] Y. Nogami, J.P. Pouget, H. Ito, T. Ishiguro, and G. Saito, Solid State Commun. **89**, 113 (1994).

[90] C.H. Mielke, N. Harrison, D.G. Rickel, A.H. Lacerda, R.M. Vestal, and L.K. Montgomery, Phys. Rev. B **56**, 4309 (1997).

[91] M.A. Tanatar, V.N. Laukhin, T. Ishiguro, H. Ito, T. Kondo, and G. Saito, Phys. Rev. B **60**, 7536 (1999).

[92] H. Weiss, M.V. Kartsovnik, W. Biberacher, E. Steep, E. Balthes, A.G.M. Jansen, K. Andres, and N.D. Kushch, Phys. Rev. B **59**, 12370 (1999).

[93] H. Weiss, M.V. Kartsovnik, W. Biberacher, E. Balthes, A.G.M. Jansen, and N.D. Kushch, Phys. Rev. B **60**, 16259 (1999).

[94] L.P. Le, G.M. Luke, B.J. Sternlieb, W.D. Wu, Y.J. Uemura, J.H. Brewer, T.M. Riseman, C.E. Stronach, G. Saito, H. Yamochi, H.H. Wang, A.M. Kini, K.D. Carlson, and J.M. Williams, Phys. Rev. Lett. **68**, 1923 (1992).

[95] H. Mayaffre, P. Wzietek, D. Jérome, C. Lenoir, and P. Batail, Phys. Rev. Lett. **75**, 4122 (1995).

[96] Y. Nakazawa and K. Kanoda, Phys. Rev. B **55**, 8670 (1997).

[97] M. Pinterić, S. Tomić, M. Prester, D. Drobac, O. Milat, K. Maki, D. Schweitzer, I. Heinen, and W. Strunz, Phys. Rev. B **61**, 7033 (2000).

[98] R.H. McKenzie, Science **278**, 820 (1997), cond-mat/9812113.

[99] Y. Maeno, H. Hashimoto, K. Yoshida, S. Nishizaki, T. Fujita, J.G. Bednorz, and F. Lichtenberg, Nature (London) **372**, 532 (1994).

[100] T. Katsufuji, M. Kasai, and Y. Tokura, Phys. Rev. Lett. **76**, 126 (1996).

[101] T. Watanabe and A. Matsuda, Phys. Rev. B **54**, R6881 (1996).

[102] S. Martin, A.T. Fiory, R.M. Fleming, L.F. Schneemeyer, and J.V. Waszczak, Phys. Rev. Lett. **60**, 2194, 1988

[103] M. Dressel, O. Klein, G. Grüner, K.D. Carlson, H.H. Wang, and J.M. Williams, Phys. Rev. B **50**, 13603 (1994).

[104] Y.B. Xie, Phys. Rev. B **45**, 11375 (1992).

[105] R.M. Hazen, in *Physical Properties of High Temperature Superconductors II*, edited by D.M. Ginsberg (World Scientific, Singapore, 1990), p. 168.

[106] M.A. Quijada, D.B. Tanner, R.J. Kelley, M. Onellion, H. Berger, and G. Margaritondo, Phys. Rev. B **60**, 14917 (1999).

[107] S. Tajima, G.D. Gu, S. Miyamoto, A. Odagawa, and N. Koshizuka, Phys. Rev. B **48**, 16164 (1993).

[108] M.G. Hildebrand, M. Reedyk, T. Katsufuji, and Y. Tokura, to be published.

[109] J.E. Eldridge, K. Kornelsen, H.H. Wang, J.M. Williams, A.V. Strieby Crouch, and D.M. Watkins, Solid State Commun. **79**, 583 (1991).

[110] T. Sugano, H. Hayashi, M. Kinoshita, and K. Nishikida, Phys. Rev. B **39**, 11387 (1989).

[111] K. Kornelsen, J.E. Eldridge, H.H. Wang, and J.M. Williams, Phys. Rev. B **44**, 5235 (1991).

[112] K. Kornelsen, J.E. Eldridge, H.H. Wang, H.A. Charlier, and J.M. Williams, Solid State Commun. **81**, 343 (1992).

[113] M. Meneghetti, R. Bozio, and C. Pecile, J. Phys. **47**, 1377 (1986).

[114] M.G. Kaplunov, E.B. Yagubskii, L.P. Rosenberg, and Y.G. Borodko, Phys. Stat. Solidi (a) **89**, 509 (1985).

[115] C.S. Jacobsen, J.M. Williams, and H.H. Wang, Solid State Commun. **54**, 937 (1985).

[116] M. Tokumoto, H. Anzai, K. Takahashi, N. Kinoshita, K. Murata, T. Ishiguro, Y. Tanaka, Y. Hayakawa, H. Nagamori, and K. Nagasaka, Syn. Metals **27**, A171 (1988).

[117] R.M. Vlasova, S.Y. Priev, V.N. Semkin, R.N. Lyubovskaya, E.I. Zhilyaeva, and V.M. Yartsev, Mater. Sci. **17**, 75 (1991).

[118] R.M. Vlasova, S.Y. Priev, V.N. Semkin, R.N. Lyubovskaya, E.I. Zhilyaeva, E.B. Yagubskii, and V.M. Yartsev, Syn. Metals **48**, 129 (1992).

[119] R.M. Vlasova, O.O. Drozdova, V.N. Semkin, N.D. Kushch, and E.B. Yagubskii, Phys. Solid State **35**, 408 (1993).

[120] T. Nakano, N. Momono, M. Oda, and M. Ido, J. Phys. Soc. Japan **67**, 2622 (1998).

[121] C.S. Jacobsen, D.B. Tanner, and K. Bechgaard, Phys. Rev. B **28**, 7019 (1983).

[122] T. Komatsu, N. Matsukawa, T. Inoue, and G. Saito, J. Phys. Soc. Japan **65**, 1340 (1996).

[123] A. Fortunelli and A. Painelli, J. Chem. Phys. **106**, 8051 (1997).

[124] R.H. McKenzie, Comments Cond. Matt. Phys. **18**, 309 (1998).

[125] C.E. Campos, P.S. Sandhu, J.S. Brooks, and T. Ziman, Phys. Rev. B **53**, 12725 (1996).

[126] M. Rahal, D. Chasseau, J. Gaultier, L. Ducasse, M. Kurmoo, and P. Day, Acta Cryst. **B53**, 159 (1997).

[127] S.L. Cooper and K.E. Gray, in *Physical Properties of High-Temperature Superconductors IV*, edited by D.M. Ginsberg (World Scientific, Singapore, 1994).

[128] A.P. Mackenzie, S.R. Julian, A.J. Diver, G.J. McMullan, M.P. Ray, G.G. Lonzarich, Y. Maeno, S. Nishizaki, and T. Fujita, Phys. Rev. Lett. **76**, 3786 (1996).

[129] K. Yoshida, F. Nakamura, T. Goko, T. Fujita, Y. Maeno, Y. Mori, and S. NishiZaki, Phys. Rev. B **58**, 15062 (1998).

[130] A. Schwartz, M. Dressel, G. Grüner, V. Vescoli, L. Degiorgi, and T. Giamarchi, Phys. Rev. B **58**, 1261 (1998).

[131] L. Balicas, Phys. Rev. B **59**, 12830 (1999).

[132] N. Kumar and A.M. Jayannavar, Phys. Rev. B **45**, 5001 (1992).

[133] L. Forro, V. Ilakovac, J.R. Cooper, C. Ayache, and J.-Y. Henry, Phys. Rev. B **46**, 6626 (1992).

[134] M. Dressel, J.E. Eldridge, J.M. Williams, and H.H. Wang, Physica C **203**, 247 (1992).

[135] J.E. Eldridge, C.C. Homes, J.M. Williams, A.M. Kini, and H.H. Wang, Spectrochimica Acta **51A**, 947 (1995).

[136] J.E. Eldridge, Y. Xie, H.H. Wang, J.M. Williams, A.M. Kini, and J.A. Schlueter, Spectrochimica Acta **52A**, 45 (1996).

[137] J.E. Eldridge, Y. Xie, H.H. Wang, J.M. Williams, A.M. Kini, and J.A. Schlueter, Mol. Cryst. Liq. Cryst. **284**, 97 (1996).

[138] M.J. Rice, Phys. Rev. Lett. **37**, 36, (1976).

[139] M.J. Rice, L. Pietronero and P. Bruesch, Solid State Commun. **21**, 757 (1977).

[140] H.K. Ng, T. Timusk, and K. Bechgaard, Phys. Rev. B **30**, 5842 (1984).

[141] D. Colson, A. Bertinotti, J. Hammann, J.F. Marucco, and A. Pinatel, Physica C **233**, 231 (1994); A. Bertinotti, D. Colson, J. Hammann, J-F. Marucco, D. Luzet, A. Pinatel, and V. Viallet, Physica C **250**, 213 (1995).

[142] J.J. McGuire, M. Windt, T. Startseva, T. Timusk, D. Colson, and V. Viallet-Guillen, Phys. Rev. B **62**, 8711 (2000).

[143] W.N. Hardy, D.A. Bonn, D.C. Morgan, R. Liang, and K. Zhang, Phys. Rev. Lett. **70**, 3999 (1993).

[144] T. Timusk and B. Statt, Rep. Prog. Phys. **62**, 61 (1999).

[145] J.W. Loram, K.A. Mirza, J.R. Cooper, and J.L. Tallon, Physica C **282-287**, 1405 (1997).

[146] B. Batlogg, H.Y. Hwang, H. Takagi, R.J. Cava, H.L. Kao, and J. Kao, Physica C **235-240**, 130 (1994).

[147] C.C. Homes, T. Timusk, R. Liang, D.A. Bonn, and W.N. Hardy, Phys. Rev. Lett. **71**, 1645 (1993).

[148] A.V. Puchkov, D.N. Basov, and T. Timusk, J. Phys.: Condens. Matter **8**, 10049 (1996).

[149] Ch. Renner, B. Revaz, J.-Y. Genoud, K. Kadowaki, and Ø. Fischer, Phys. Rev. Lett. **80**, 149 (1998).

[150] Y. DeWilde, N. Miyakawa, P. Guptasarma, M. Iavarone, L. Ozyuzer, J.F. Zasadzinski, P. Romano, D.G. Hinks, C. Kendziora, G.W. Crabtree, and K.E. Gray, Phys. Rev. Lett. **80**, 153 (1998).

[151] J.P. Carbotte, E. Schachinger, and D.N. Basov, Nature **401**, 354 (1999).

[152] There is a short report of a reflectance ratio on thin films of a three-layer mercury material by E.J. Choi, Journal of the Korean Physical Society **31**, 815 (1997). These reflectivity data are dominated by a prominent structure around 500 cm^{-1}, possibly due to substrate phonons since this structure is absent in our single crystal data.

[153] T. Startseva, Ph.D. Thesis, McMaster University, 1998.

[154] A. Bertinotti, D. Colson, J.-F. Marucco, V. Viallet, J. Le Bras, L. Fruchter, C. Marcenat, A. Carrington, and J. Hammann, in *Studies of High Temperature Superconductors*, edited by A. Narlikar (Nova Science, New York, 1997).

[155] I. Terasaki, S. Tajima, H. Eisaki, H. Takagi, K. Uchinokura, and S. Uchida, Phys. Rev B **41**, 865 (1990).

[156] T. Timusk, D.N. Basov, C.C. Homes, A.V. Puchkov, and M. Reedyk, Journal of Superconductivity **8**, 437 (1995).

[157] D.N. Basov, B. Dabrowski, and T. Timusk, Phys. Rev. Lett. **81**, 2132 (1998).

[158] T. Rõõm anf T. Timusk (unpublished) (1998).

[159] A. Sacuto, R. Combescot, N. Bontemps, C.A. Müller, V. Vialet, and D. Colson, Phys. Rev. B **58**, 11721 (1998).

[160] A. Sacuto (private communication).

[161] C. Panagopoulos, J.R. Cooper, T. Xiang, G.B. Peacock, I. Gameson, and P.P. Edwards, Phys. Rev. Lett. **79**, 2320 (1997).

[162] J. Corson, J. Orenstein, S. Oh, J. O'Donnell, and J.N. Eckstein, Phys. Rev. Lett. **85**, 2569 (2000).

[163] A. Carrington, D. Colson, Y. Dumont, C. Ayache, A. Bertinotti, J.F. Marucco, Physica C **234**, 1 (1994).

[164] M.-H. Julien, P. Carretta, M. Horvatić, C. Berthier, Y. Berthier, P. Ségransan, A. Carrington, and D. Colson, Phys. Rev. Lett. **76**, 4238 (1996).

[165] G.V.M. Williams, J.L. Tallon, E.M. Haines, R. Michalak, and R. Dupree, Phys. Rev. Lett. **78**, 721 (1997).

[166] J.M. Harris, P.J. White, Z.-X. Shen, H. Ikeda, R. Yoshizaki, H. Eisaki, S. Uchida, W.D. Si, J.W. Xiong, Z.-X. Zhao, and D.S. Dessau, Phys. Rev. Lett. **79**, 143 (1997).

[167] R. Hackl, G. Krug, R. Nemetshcek, M. Opel, and B. Stadlober, in *Spectroscopic Studies of Superconductors V*, Ivan Bozovic and Dirk van der Marel, Editors, Proc. SPIE **2696**, 194 (1996).

[168] J.P. Carbotte, Rev. Mod. Phys. B **62**, 1027 (1990).